Average properties of nuclear states in the quasi-continuum region

Hilde-Therese Nyhus

Thesis submitted in partial fulfilment of the requirements for the degree of philosophiae doctor

Department of Physics
Faculty of Mathematics and Natural Sciences
University of Oslo

March 2014

Series of dissertations submitted to the
Faculty of Mathematics and Natural Sciences, University of Oslo
No. 1512

ISSN 1501-7710

Cover: Inger Sandved Anfinsen.
Printed in Norway: AIT Oslo AS.

Produced in co-operation with Akademika Publishing.
The thesis is produced by Akademika Publishing merely in connection with the thesis defence. Kindly direct all inquiries regarding the thesis to the copyright holder or the unit which grants the doctorate.

Acknowledgments

The completion of this thesis has been made possible by the help and support from many people around me. First and foremost, I owe a great thanks to my supervisors. Sunniva, thanks for giving me the chance to start my Ph.D. and for always being very encouraging. Magne, I appreciate that you always give me good and clear answers. Ann-Cecilie, you always take time to help me, even though you have tons of things to do. It seems as if you have full control of everything, and you have been of tremendous help.

A special thanks to Hiroaki for all the help you have given me with the *New-SUBARU* experiments, and for letting me take part in the *KOBe*$^{-}$ collaboration, it has been interesting and I have learned so much! Thanks also to the *Bucharest team*, it has been very nice working with you.

My work and traveling partner Therese, I appreciate all the support and help you have given me. Thanks for saying yes in the first place to come with me to Japan. We have had some interesting and fun experiences during our trips, which I will never forget ☺.

Thanks also to the engineers at the *OCL* for providing great experimental conditions during the campaigns.

I am deeply grateful to the whole physics group at *SAFE*, for making my time here a great pleasure. Eda, Francesca, Frank, Aylin and Therese you are always there when I need a break, for lunch every day, running, swimming... I don't think I could have survived the last year without.

I have also gotten support from my friends Gunn, Nina, Siri, Ann-Kristin and Kosovare, which I appreciate very much.

Last but not least I owe a big thanks to my family. My brothers Helge-Jacob and Sverre-Kjetil, sister in-law Anette and in-laws Kari and Rune, thanks for always helping me in any way possible. Especially, thanks for helping out with the kids leaving me with time to finnish my thesis. Audun, thanks for being under-

standing, and for holding out with me, even though I have been a bit absent and very stressed the last months (or years...). Finally, I would like to thank the two best boys in the world, my sons, Christoffer and Jacob, for making me take some much needed time off from work once in a while, and for keeping me happy even in a stressful time ☺.

Hilde-Therese Nyhus

March, 2014

Contents

Chapter 1

Introduction

Since the discovery of the atomic nucleus at the start of the 20th century, it has been studied in depth. Along with increased understanding of nuclear physics, some of the most questioned puzzles of the universe have been resolved. Fundamental understanding of the nuclear constituents and interactions is essential to describe the evolution of the universe and the abundance of elements. Nuclear research have also shown great impact in many fields of applied science. From nuclear power, to medicine treatment and diagnostics, ion implantation in material engineering and radiocarbon dating in geology and archeology, to mention some.

The atomic nucleus is a complex quantum-mechanical system. It consists of protons and neutrons that are bound together by the strong interaction. The nucleus can be characterized by quantum numbers such as energy levels, spin and parity. The unique set of quantum numbers defines the states of the nucleus. Representing the nucleons as wave functions one can calculate the distinct states. However, calculations derived from first principles is only possible for a very few light nuclei. To describe most nuclei one relies on phenomenological models. Two successful models in this respect is the shell model Monte Carlo method for spherical nuclei, and the Nilsson model for deformed nuclei. Although these methods provide accurate results for many nuclei, one still depend heavily on experiments to obtain a full description.

In the discrete energy region one can measure the quantum states through spectroscopy experiments. While at higher excitation energies, the level density is so high that modern equipment cannot resolve the individual levels. This region is known as the quasi-continuum. At even higher excitation energies we have the continuum region where the levels overlap. Beyond the discrete region it is reasonable to do simplifications and look at average nuclear properties, rather than considering single particle descriptions.

Statistical nuclear properties in the quasi-continuum are well described by the level density and the radiative strength function. The level density gives the aver-

age number of levels as a function of excitation energy, while the radiative strength function describes average electromagnetic properties of the nucleus, and it is therefore closely related to reduced transition probabilities. These two functions are not only interesting because of the information they reveal on the nuclear structure, but also because the light they cast upon other fields of physics. Applications of the level density and radiative strength function include astrophysical calculations determining the abundance of the elements in the universe, and modelling of unknown (n,γ) cross sections relevant for next generation reactors.

In this thesis the level density and radiative strength function have been investigated for several nuclei in the range, $A = 105 - 164$. In particular, small resonances on the tail of the giant electric dipole resonance (GEDR) have been studied, using complementary techniques to obtain the strength function both above and below the neutron threshold. By use of the so-called Oslo method the level density and the radiative strength function can be derived simultaneously from one and the same experiment. The excitation energy region from where we extract the strength function extend from the discrete region up to the energy of the neutron separation threshold. The reaction channels used to excite the nuclei are inelastic- and neutron pick-up reactions induced with a ^{3}He beam. These experiments have been performed at the Oslo Cyclotron Laboratory (OCL). In addition, photo-absorption experiments have been conducted at the NewSUBARU synchrotron laboratory in Japan. From these experiment we derive the photo-neutron cross section, and the radiative strength function, from the neutron separation threshold up to the peak of the GEDR.

In this work we have studied several dysprosium isotopes both above and below the neutron separation threshold, we have also investigated palladium isotopes by use of the Oslo method to compare with pre-existing photo-neutron data. Furthermore, we have investigated numerous neodymium and samarium isotopes from photo-absorption experiments. These nuclei cover a wide mass region, and we know that nuclei exhibit different characteristics depending on mass and deformation. For the palladium nuclei, special focus has been on the strength function at low γ energy, where the strength is relatively constant over a wide γ-energy region. We also observe indications of a resonance located at energies around 8 MeV. The theoretical explanation for these structures is not yet understood and it is therefore of great importance to learn more about it, and map the nuclei that exhibit this behaviour.

The dysprosium nuclei have a collective resonance mode located at around 3 MeV of excitation energy, called the $M1$ scissors mode. Characteristics of this resonance have been studied. Photo-neutron data of dysprosium isotopes are also measured, to give a complete description of the strength function below the peak of the giant resonance. The measured cross sections are found in an energy region where there are no preexisting data of dysprosium nuclei. The photo-neutron data

are used to check and renormalize the Oslo data. Furthermore radiative neutron capture cross sections are calculate by use of the TALYS reaction code, and astrophysical reaction rates are calculated. In particular, how the $M1$ scissors mode affect the reaction rated are discussed.

In addition the nuclear level density is studied for palladium and dysprosium isotopes, which provides rich information on the nuclear structure at low excitation energy. One can identify the region of which the nuclear Cooper pairs are broken, and we extract thermodynamic quantities from the level density.

Finally, the neodymium and samarium isotopes are of great importance with respect to astrophysical applications. The s-process path along the line of β stability has been studied for the neodymium and samarium isotopes. The short-lived ^{147}Nd isotope is an s-process branch point nucleus, where β-decay and neutron capture are computing processes. Furthermore, radiative neutron capture cross sections for ^{147}Nd affects the isotopic ratio of the two s-only nuclei, ^{148}Sm and ^{150}Sm. The present photoneutron measurement also involved a p-process nucleus ^{144}Sm, s-only nuclei ^{148}Sm and ^{150}Sm and an r-only nucleus ^{154}Sm.

This work is organised as follows, chapter 2 outlines the concepts of level density, radiative strength function, and radiative neutron capture cross sections. In chapter 3 and 4 experimental details are described, regarding the NewSUBARU and Oslo experiments, respectively. Chapter 5 is dedicated to the methods used for data reduction. The full scientific work in form of the papers produced are presented with reprints in chapter 6. Finally, a summary and conclusions of the work are drawn in chapter 7.

Chapter 2

Level density, radiative strength function and radiative neutron capture cross sections

We have studied statistical properties of excited nuclei in the quasi-continuum region. By looking at average nuclear properties, contained in the nuclear level density and radiative strength function, we obtain importance understanding of the underlying nuclear structure.

In this chapter, the theory behind the level density and radiative strength function will be presented, along with the phenomenological models developed to describe the behaviour of the two quantities. In addition, calculations of the radiative neutron capture cross sections are described.

2.1 Level density

The level density is defined as the number of quantum levels per energy unit as a function of excitation energy. At low excitation energy we find discrete levels, and the level density obtained by spectroscopy measurements. As the excitation energy increases the quasi-continuum is reached, a region in which the level density becomes so large that the individual levels can not be resolved in experiments. The onset of the quasi-continuum region differs for the various mass regions, in rare earth isotopes it typically starts above $2-3$ MeV of excitation energy.

Bethe developed the so called Fermi gas model in 1936 [1], where the particles are assumed to move independently, and single-particle states are considered to be equally spaced. The original formula gives the level density as a function of

excitation energy,

$$\rho(E) = \frac{\sqrt{\pi}}{12}\frac{\exp(2\sqrt{aE})}{a^{1/4}E^{5/4}}, \tag{2.1}$$

at a given excitation energy E. The level density parameter a is expressed by

$$a = \frac{\pi}{6}(g_p + g_n), \tag{2.2}$$

where g_p and g_n are the single-particle level density parameters for protons and neutrons, respectively. However, the Fermi gas model is limited by not accounting for pairing correlations, collective phenomena or shell effects. Later, modified versions of the Fermi gas formula has been developed, where these phenomena are accounted for by employing free parameters that are adjusted to fit the experimental data on level spacings obtained from neutron and/ or proton resonance experiments. Gilbert and Cameron proposed in 1965 a level density formula where the effective excitation energy is reduced by the pairing energy Δ_p and Δ_n for protons and neutrons, respectively. In this way E is replaced with $U = E - \Delta_p - \Delta_n$ [2], resulting in a lower level density for the same excitation energy. The expression for this level density is as follows,

$$\rho(U) = \frac{\sqrt{\pi}}{12}\frac{\exp(2\sqrt{aU})}{a^{1/4}U^{5/4}}\frac{1}{\sqrt{2\pi}\sigma}. \tag{2.3}$$

The spin cutoff parameter σ is given by,

$$\sigma^2 = (g_p + g_n)\left\langle m^2 \right\rangle T, \tag{2.4}$$

where $\left\langle m^2 \right\rangle$ is the mean-square magnetic quantum number for single-particle states, and the temperature $T = \sqrt{U/a}$.

It was soon realised that the shift, equal to $\Delta_p + \Delta_n$, is too large and therefore this energy is *back-shifted* by a parameter C_1, so that $U = E - \Delta_p - \Delta_n + C_1$ [3]. In the back-shifted Fermi gas model described in Ref. [3], both the parameter C_1 and the level density parameter a are treated as free parameters so that the experimental data can be modelled over a wider range of energies.

In 2005 a back-shifted Fermi gas model was proposed by von Egidy and Bucurescu [4]. It is given by the expression

$$\rho_{BS}(E) = \frac{\exp[2\sqrt{a(E-E_1)}]}{12\sqrt{2}\sigma a^{1/4}(E-E_1)^{5/4}}, \tag{2.5}$$

for an excitation energy E, where the level density parameter a and the energy shift E_1 are treated as free parameters to be fitted to experimental data. The spin-cutoff parameter σ is given by

$$\sigma^2 = 0.0146A^{5/3}\frac{1+\sqrt{1+4a(E-E_1)}}{2a}, \tag{2.6}$$

where A denotes the mass number. The spin cut-off parameter has been further revised by von Egidy and Bucurescu, the latest version was published in 2009, see Ref. [5] for more details. In this model the spin cut-off parameter has the form

$$\sigma^2 = 0.391A^{0.675}(E - 0.5Pa)^{0.312}, \tag{2.7}$$

where Pa is the deuteron pairing energy.

In addition to the Fermi gas model there exists a variety of other models that can be used to calculate the level density, both semi-empirical and microscopic calculations. Examples of this includes the original HFB plus combinatorial model of S. Goriely [6], and the temperature-dependent HFB model of S. Hilaire [7]. An other method is the shell model Monte Carlo approach as presented by Y. Alhassid [8, 9, 10].

2.2 Gamma decay

Nuclear reactions which produces an excited nucleus will be accompanied by γ decay. The total angular momentum must be conserved. The parameter L represents the quantum number for angular momentum. The numbers that L can attain must be integers above zero, where $L = 1$ characterises a dipole, $L = 2$ a quadrupole, $L = 3$ an octupole etc. Furthermore, the parity of the radiation distinguishes between electric and magnetic multipole radiation. Electric multipole radiation have even parity if L is even, while magnetic multi- pole radiation have even parity if L is odd. Photo emission is dominated by electromagnetic dipole radiation ($E1$ in short notation).

2.3 Radiative strength function

The RSF is a measure of the average electromagnetic properties of the nucleus. It is therefore closely related to the γ decay and photo absorption processes. The radiative strength function (RSF) of a nucleus is defined as the sum over the strength functions f_{XL} of all possible multipolarities L and electric- and magnetic character X. We distinguish between two types of radiative strength functions [11],

(i) Downward strength function $\overleftarrow{f}$ related to the average radiative width of γ decay.

(ii) Upward strength function $\overrightarrow{f}$ connected to the cross-section for γ absorption.

The RSF is closely connected to the γ-transmission coefficient $\mathscr{T}_{XL}$, which represents a transition with multipolarity XL and energy E_γ,

$$\mathscr{T}_{XL}(E_\gamma) = 2\pi E_\gamma^{2L+1} \overleftarrow{f_{XL}}(E_\gamma). \tag{2.8}$$

In 1972 Bartholomew [12] gave the following model-independent description of the RSF for a transition from the initial state i to the final state f,

$$\overleftarrow{f_{XL}}(E_\gamma) = \frac{\langle \Gamma_{\gamma if} \rangle}{E_\gamma^{2L+1} D_i}, \tag{2.9}$$

where $\langle \Gamma_{\gamma if} \rangle$ is the radiative width, E_γ gives the transition energy and D_i represents the level spacing of the initial states.

The upward RSF is given by the average photo-absorption cross section $\langle \sigma_{\mathrm{XL}}(E_\gamma) \rangle$ summed over all possible spins of the final states [11],

$$\overrightarrow{f_{XL}}(E_\gamma) = \frac{1}{(2L+1)(\pi\hbar c)^2} \frac{\langle \sigma_{\mathrm{XL}}(E_\gamma) \rangle}{E_\gamma^{2L-1}}. \tag{2.10}$$

According to Fermi's golden rule and the principle of detailed balance the upward and downward RSF will correspond to each other, given that the same states are populated equally whether it is populated from above or below.

2.3.1 Modelling the RSF

The RSF is dominated by the giant electric dipole resonance (GEDR). This is a collective excitation mode of the nucleus and geometrically it is interpreted to originate from oscillation of protons against neutrons in the nucleus. The Brink-Axel hypothesis [13, 14] states that collective excitations built on excited states have the same properties as those built on the ground state. As a consequence the probability of γ decay is only dependent on the γ-ray energy E_γ, and not on the temperature of the final state excitation. The standard Lorentzian model (SLO) [11] is widely used to describe the GEDR,

$$f_{E1}^{SLO}(E_\gamma) = \frac{1}{3\pi^2\hbar^2c^2} \frac{\sigma_{E1}\Gamma_{E1}^2 E_\gamma}{(E_\gamma^2 - E_{E1}^2)^2 + \Gamma_{E1}^2 E_\gamma^2}, \tag{2.11}$$

where σ_{E1}, Γ_{E1} and E_{E1} represents the strength, width and centroid energy of the resonance, respectively. The GEDR parameters are derived from photo-absorption experiments. The SLO model provides a very good description of the GEDR close to the centroid, for medium heavy and heavy nuclei. However, in the low excitation energy region (< 2 MeV) the γ-ray strength predicted from Eq. (2.11) is lower than experimentally observed strength.

A model developed by Kadmenskiĭ, Markushev and Furman (KMF model) [15] reproduces the low energy region well and gives a non-zero strength for $E_\gamma \to 0$. In contrast to the SLO model, the KMF model is dependent on the temperature of the final states T_f,

$$f_{E1}^{KMF}(E_\gamma) = \frac{1}{3\pi^2\hbar^2c^2}\frac{0.7\sigma_{E1}E_{E1}\Gamma_{E1}\Gamma_{KMF}(E_\gamma,T_f)}{(E_\gamma^2-E_{E1}^2)^2}, \tag{2.12}$$

where the temperature dependent width of the GEDR is given by,

$$\Gamma_{KMF}(E_\gamma,T_f) = \frac{\Gamma_r}{E_r^2}(E_\gamma^2+4\pi^2T_f^2). \tag{2.13}$$

The temperature dependence is, however, in contradiction with the Brink-Axel hypothesis. The KMF model fails to describe the GEDR close to the centroid, where Eq. (2.12) diverges.

The generalised Lorentzian model (GLO) [16],

$$f_{E1}^{GLO}(E_\gamma) = \frac{1}{3\pi^2\hbar^2c^2}\sigma_{E1}\Gamma_{E1}\left[\frac{E_\gamma\Gamma_{KMF}(E_{\gamma,T})}{(E_\gamma^2-E_{E1}^2)^2+(E_\gamma\Gamma_{KMF}(E_\gamma,T_f))^2}+0.7\frac{\Gamma_{KMF}(E_\gamma=0,T)}{E_{E1}^3}\right] \tag{2.14}$$

describes both the low energy region and the peak region of the GEDR well, at least for spherical nuclei.

The contribution from other resonance modes such as the giant magnetic dipole resonance (GMDR) should also be considered. This resonance has in this work been described by a standard Lorentzian of the form of Eq. (2.11). The resonance parameters of the $M1$ resonance is deduced from the systematics given in Ref. [11]. Various small resonances are also observed in different mass regions. For the dysprosium nuclei the $M1$ resonance called the *scissors mode* is observed around ≈ 3 MeV. Also this resonance is modelled by a SLO. In the palladium data, enhanced strength is observed around ≈ 8 MeV. This resonance is often called pygmy resonances and is best described by a Gaussian with standard deviation equal to $\Gamma_{pyg}/2$,

$$f_{Pd,py} = \frac{1}{3(\pi\hbar c)^2}\sqrt{\frac{2}{\pi}}\frac{\sigma_{py}}{\Gamma_{py}}e^{-2(E_\gamma-E_{py})^2/\Gamma_{py}^2}. \tag{2.15}$$

2.4 Radiative neutron capture

It is in general challenging to measure (n,γ) cross sections directly for relatively high incoming neutron energies ($\approx$ keV). In particular, unstable isotopes are hard or impossible to measure, because radioactive targets are difficult to handle and

because of the high intrinsic radiation. Recently, the (n,γ) cross sections of the unstable ^{63}Ni isotope (half-life 100.1 yr) was measured for the first time at the neutron time-of-flight facility n_ TOF at CERN [17]. However, nuclei with half-lives shorter than this is yet out of reach [18].

We can however determine (n,γ) cross sections by an indirect method from the reversed process, namely photo absorption and neutron emission (γ,n). In doing so, we can not use the principal of detailed balance directly, because the (γ,n) cross section only represents photo absorption of a γ ray of energy higher than the neutron separation energy, of a nucleus in its ground state, while a nucleus that has undergone neutron capture can decay to all possible states below the neutron capture state, see Fig. 2.1. One can instead use an expression based on the Hauser-Feshbach statistical model. The expression is applicable for compound nuclei, where we have a statistical distribution of nuclear excited states [18]. Within these assumptions, the radiative neutron capture cross section depends on three nuclear statistical quantities, namely, the neutron optical model potential, the RSF, and the nuclear level density [19]

$$\sigma_{n,\gamma} = \frac{\pi}{k_n^2}\sum_{J,\pi} g_J \frac{T_\gamma(E,J,\pi)T_n(E,J,\pi)}{T_{\text{tot}}} \approx \frac{\pi}{k_n^2}\sum_{J,\pi} g_J T_\gamma(E,J,\pi), \tag{2.16}$$

where k_n represents the incident neutron wave number, E, J and π gives the energy, spin and parity of the compound state, respectively. Furthermore, the functions T_γ and T_n are the γ- and neutron-transmission coefficients, respectively, and $T_{\text{tot}} = T_\gamma + T_n$. The factor g_J is given by $g_J = (2J+1)/(4J_t+2)$, with the spin J_t of the target nucleus. Note that for keV neutrons, the decay from states above the neutron separation threshold, is dominated by the neutron emission channel, the neutron-transmission coefficient is much larger than the γ-transmission coefficient ($T_n >> T_\gamma$). Furthermore, this means that $T_\gamma(E,J,\pi) \approx T_{\text{tot}}$, which explains the simplification of Eq. (2.16).

The γ-transmission coefficient is given as

$$T_\gamma(E,J,\pi) = \sum_{\nu,X,L} T^{\nu}_{XL}(E_\gamma) + \sum_{X,L}\int T_{XL}(E_\gamma)\rho(E-E_\gamma,J,\pi)dE_\gamma, \tag{2.17}$$

where $T_{XL}(E_\gamma)$ is the γ-transmission coefficient for energy E_γ with multipolarity XL, and ρ represents the nuclear level density [19]. The first term is a sum of T_{XL} over low lying discrete states ν relevant to a given multipolarity (XL) and the second term is an integration of T_{XL} over nuclear states $\rho(E-E_\gamma)dE_\gamma$ in the energy interval dE_γ at the excitation energy $E-E_\gamma$.

The γ-transmission coefficient is uniquely related to the downward RSF $\overleftarrow{f_{XL}}(E_\gamma)$ by $T_{XL}(E_\gamma) = 2\pi E_\gamma^{(2L+1)}\overleftarrow{f_{XL}}(E_\gamma)$, which we can measure directly with the Oslo

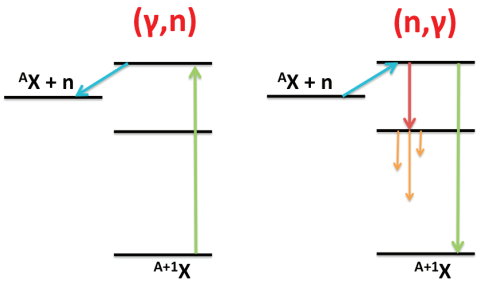

Figure 2.1: *An illustration of the (γ,n) (left) and (n,γ) (right) reactions. The inverse process of the photo absorption reaction is represented by the green arrow in the right figure, where the nucleus decays directly from the capture state to the ground state. The red arrow represent a typical primary γ transition, while the orange ones give possible decay routs after the primary γ-ray transition*

method. Photodisintegration is an excellent probe of the upward RSF. According to Fermi's golden rule and the principle of detailed balance the upward and downward RSF will correspond to each other, given that the same states are populated equally whether it is populated from above or below.

Neutrons will be quickly thermalised in a dense stellar plasma. We can assume that the neutron spectrum at s-process sites can be described by a Maxwell-Boltzmann distribution [18]. The Maxwellian-average cross section (MACS) is therefore considered to represent the stellar reaction cross section, and is found by averaging the experimental data over such a spectrum [18]. As a standard the MACS are often compared for a thermal energy of 30 keV.

Chapter 3

Photo-neutron experiments

In this work, the radiative strength function have been extracted using two very different techniques, by means of photo-neutron experiments and charged-particle induced reactions. In this chapter, the photo-neutron measurements are outlined. From these experiments we extract the radiative strength function above the neutron separation energy S_n.

The experiments were conducted at the NewSUBARU laboratory, which is a synchrotron radiation facility consisting of an electron storage ring. Here, one can produce laser-Compton scatterering (LCS) γ-ray beams. Such beams are ideal for (γ,n) experiments, because they have tuneable energies and are nearly monochromatic.

3.1 The NewSUBARU laboratory

The NewSUBARU laboratory is located at the SPring-8 site (Super Photon ring-8 GeV) in Japan. SPring-8 is a large synchrotron radiation facility, managed by RIKEN, which delivers the most powerful synchrotron radiation currently available [20]. Electron beams are accelerated by the SPring-8 linear accelerator (linac) alternatively injected into SPring-8 and NewSUBARU storage rings, see Fig. 3.1. The NewSUBARU ring is smaller than SPring-8, with a circumference of 119 m, compared to 396 m for SPring8. A photo of the site is displayed in Fig. 3.2. Both SPring-8 and NewSUBARU have a wide range of users from different research areas, such as materials science, spectroscopic analysis, earth science, life science, environmental science and industrial applications. The NewSUBARU laboratory has nine different research stations as displayed in the overview picture in Fig. 3.3. In the lowest corner of the figure, marked *BL01*, the work station for LCS experiments is shown. The electrons are injected into the storage ring with an initial energy of 974 MeV [21]. They are then subsequently accelerated or decelerated

to energies in the range $0.5 - 1.5$ GeV [21]. For the particular experiments featured in this thesis, electron energies in the interval $\approx 600 - 900$ MeV where used.

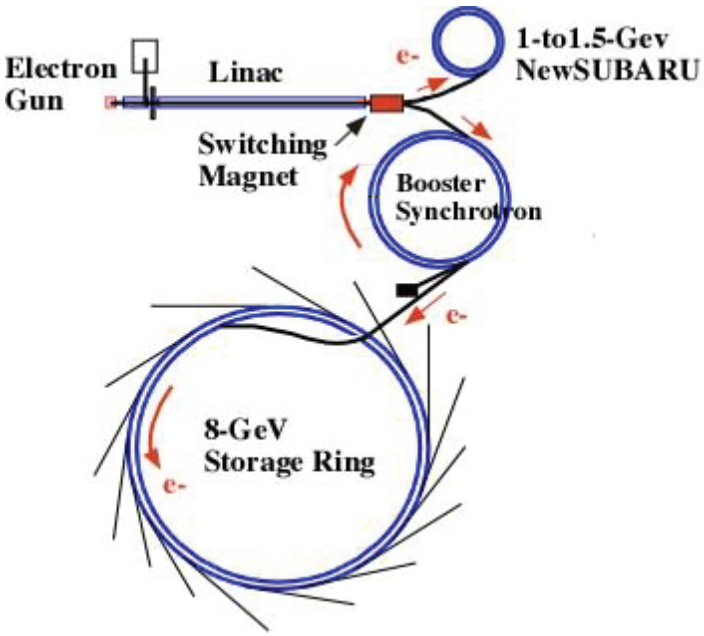

Figure 3.1: *The accelerator complex is comprised of four accelerators: a 1-GeV linac, an 8-GeV booster synchrotron, an 8-GeV storage ring and a 1.5-GeV NewSUBARU storage ring. The figure is taken from the homepage of SPring-8 [20].*

Figure 3.2: *An air photo of the SPring-8 site. The figure is taken from Ref. [22].*

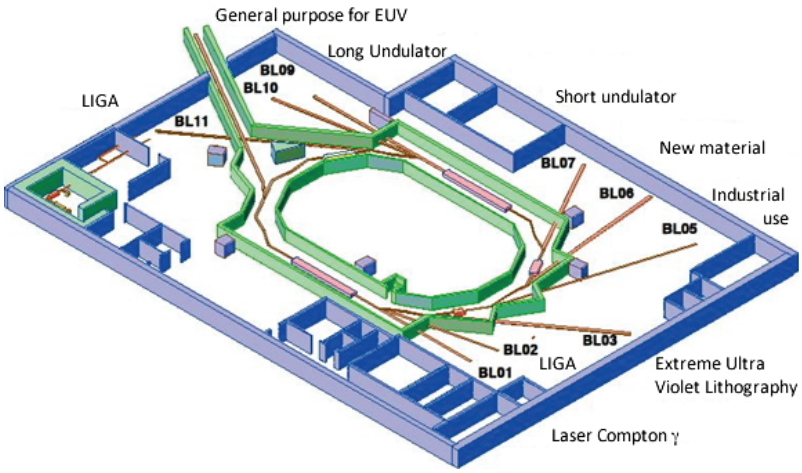

Figure 3.3: *The storage ring and the beam line of the NewSUBARU laboratory. The figure is taken from the homepage of NewSUBARU [23].*

3.1.1 Laser-Compton scattering γ-ray beams

The photo-absorption experiments was performed with laser-Compton scattering (LCS) γ-ray beams. The energy of the LCS γ-ray beam can be expressed by

$$E_\gamma = \frac{4\gamma^2 E_L}{1+(\gamma\theta)^2+4\gamma E_L/mc^2}. \tag{3.1}$$

The factor $\gamma = E_e/mc^2 = 1/\sqrt{1-\beta^2}$, is due to relativistic electrons, where $mc^2 =$ 0.511 MeV is the electron rest energy. Furthermore, E_L and E_e are the laser and electron energies, respectively. The scattering angle from the electron beam is represented by θ. The electrons and laser photons collide head on, and as we see from Eq. (3.1) the γ energy is maximised at zero scattering angle. The energy amplification factor in nearly head-on collisions is very large, of the order of $10^6 - 10^7$, for electrons with energies from several hundred MeV to a few GeV [24]. This means that an eV laser beam can be converted to an MeV γ-ray beam in LCS experiments.

The NewSUBARU ring has two long straight segments of 14 m [21]. It is in one of these segments that the LCS γ-ray beams are produced, giving a long interaction zone. At NewSUBARU γ-ray beams with energies of a few MeV are produced using a CO_2 laser (wavelength $\lambda = 10.59$ nm). The CO_2 laser was not used when measuring the target nuclei, however it was used for an energy calibrate of electron beam as reported in Ref. [24]. The facility also provides γ-ray beams of a few tens of MeV using a Nd:YVO_4 (Nd) laser (wavelength $\lambda = 1064$ nm) [24]. Both lasers are used in collisions with electrons of energies $0.5 - 1.0$ GeV.

The Q-switch Nd laser has a time structure with the pulse width 60 ns and a frequency 20 kHz. The LCS γ-ray beam has a macro time structure, 80 ms beam on and 20 ms beam off, that was made by applying an external trigger gate to the

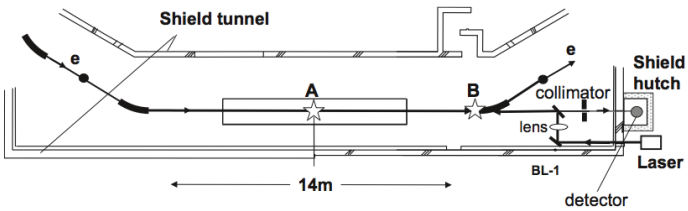

Figure 3.4: *A sketch of the experimental setup of laser Compton scattered γ rays, the figure is taken from Ref. [21].*

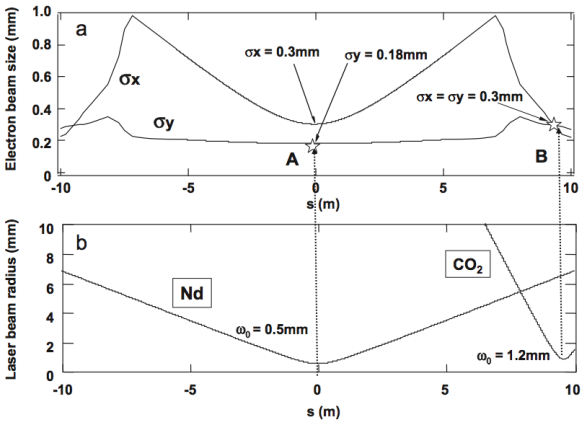

Figure 3.5: *Electron beam size (panel a) and laser beam radius (panel b) of the Nd and CO_2 lasers in the interaction zone. The zero value on the horizontal axis refers to the centre of the long straight section, the figure is taken from Ref. [21].*

laser system. The electron beam consists of bunches of electrons, and it has a frequency of 500 MHz and a 20 ps pulse width.

The collision point of the Nd laser photons with the electron beam is in a distance of 1847 cm from a 2 mm collimator, see Fig 3.4. The collision point is marked with an 'A' in Fig 3.4, the point marked with 'B' is a collision point used when applying a CO_2 laser. The collision point for this detector is closer to the laser window, because the diffraction is ten times that of the Nd laser [21].

The collision point is located a place where the electrons beam size is narrowed, see Fig 3.5.

3.2 Experimental setup

Our aim is to calculate the photo-neutron cross section from LCS experiments. The photo-neutron cross section $\sigma(E_\gamma)$ depends upon the normalized energy distribution of the γ-ray beam $n_\gamma(E_\gamma)$ as follows ,

$$\int_{S_n}^{E_{\mathrm{Max}}} n_\gamma(E_\gamma)\sigma(E_\gamma)dE_\gamma = \frac{N_n}{N_t N_\gamma \xi \varepsilon_n g}, \tag{3.2}$$

where N_n represents the number of neutrons detected, N_t gives the number of target nuclei per unit area, N_γ is the number of γ rays incident on target, ε_n represents

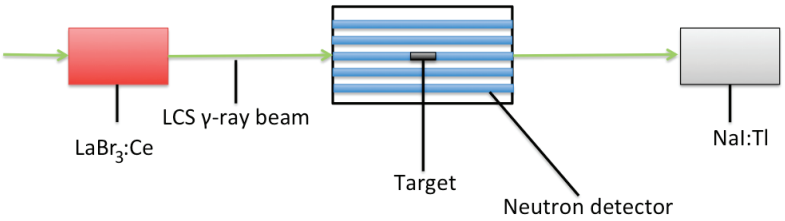

Figure 3.6: *A sketch of the detectors placed inside the hutch. The $LaBr_3$ detector is set up before or after each run to measure the energy distribution of the γ-ray beam.*

the neutron detection efficiency, and finally $\xi = (1-e^{\mu t})/(\mu t)$ is a correction factor for self attenuation in the target. The factor g represents the fraction of γ flux above the neutron separation energy S_n.

As a first approximation we assume a monochromatic γ-ray beam, by replacing the γ-energy distribution $n_\gamma(E_\gamma)$ in Eq. (3.2) by a delta function $\delta(E_\gamma - E_{\rm av})$. We obtain the following cross section in the monochromatic approximation,

$$\sigma^{\rm mono}(E_{\rm av}) = \frac{N_n}{N_t N_\gamma \xi \varepsilon_n g}. \tag{3.3}$$

where $E_{\rm av}$ is the average energy of the LCS γ-ray beam,

$$E_{\rm av} = \frac{\int_{S_n}^{E_{\rm Max}} E_\gamma n_\gamma(E_\gamma) dE_\gamma}{\int_{S_n}^{E_{\rm Max}} n_\gamma(E_\gamma) dE_\gamma}. \tag{3.4}$$

The measurements were carried out at $6-17$ different energies, depending on the target, ranging from the neutron separation energy of the target up to $\approx$ 13 MeV. For each LCS γ-ray energy, we made the following measurements:

(1) Counting the number of neutrons with ^{3}He-proportional counters.

(2) Measuring the energy distribution of the LCS γ-ray beam with a $LaBr_3:Ce$ ($LaBr_3$) detector.

(3) Determining the number of γ rays arriving at the target nucleus using a NaI:Tl (NaI) detector.

The LCS γ-ray beam had a time structure with 80 ms beam on and 20 ms beam off. The purpose of this was to detect background neutrons and γ rays. The measurements were performed inside the beam line named GACKO, which is an acronym for GAmma Collaboration hutch of KOnan University. The detectors were placed as illustrated in Fig. 3.6. The target samples were placed inside aluminium containers. The neutron threshold for aluminium is high, $S_n = 13.1$ MeV, therefore we do not open the $\mathrm{Al}(\gamma, \mathrm{n})$ reaction channel.

In the next sections a detailed description will be given of how the quantities of Eqs. (3.2) and (3.3) are measured and calculated.

3.3 Energy distribution of the γ-ray beam

While assuming the monochromatic approximation, we need to determine the energy distribution of the γ-ray beam in order to calculate a reasonable average energy E_{av}, according to Eq. (3.4). When we want to determine more precisely the cross section from expression (3.2), the key factor is the energy distribution of the γ-ray beam. A $3.5'' \times 4.0''$ $LaBr_3$ detector was used for this purpose, a photo of the detector is displayed in Fig. 3.7. The energy resolution of the detector is 4.0% FWHM for 662 keV γ rays and 2.6% FWHM for 1332 keV γ rays.

The measurements were carried out right before or after each neutron measurement run. The laser was operated in the continuous-wave mode and at a reduced power 1 W to avoid pile-up effects in the $LaBr_3$ detector.

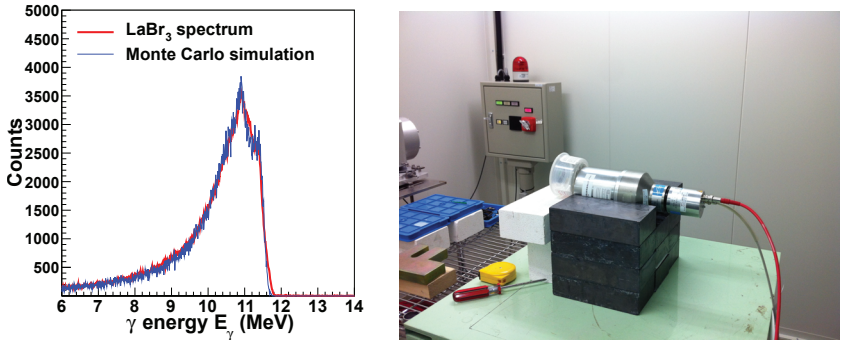

Figure 3.7: *Left panel: A typical $LaBr_3$ spectrum compared with the Monte Carlo simulation. Right panel: A picture of the detector placed along the beam line.*

The Compton backscattering of laser photons on relativistic electrons and the electromagnetic interactions of the γ-ray beams inside the $LaBr_3$ detector were simulated using the EGS4/PRESTA Monte Carlo code [25]. The energy spectra of the LCS γ-ray beams incident on the targets were obtained by best reproducing the $LaBr_3$ detector response. A typical spectrum is displayed in Fig. 3.7.

3.4 Measuring neutrons

A high efficiency 4π neutron detector composed of 20 ^{3}He proportional counters was used. They were arranged in three concentric rings, where the innermost ring consist of four counters, while the two outer rings each have eight counters. The counters were located at distances of 3.8, 7.0 and 10.0 cm from the γ-ray beam axis. All the counters are embedded in a $36 \times 36 \times 50$ cm^3 neutron moderator made of polyethylene, with the target placed in the center, see Fig. 3.8.

We detect the number of neutrons emitted in the 80 ms the laser is on (N_n(on)), and count background events in the 20 ms it is off (N_n(off)). The number of neutrons for each run is calculated as follows:

$$N = N_n(\text{on}) - 4 \cdot N_n(\text{off}) \tag{3.5}$$

The amount of neutrons (N_n(on)) detected will depend upon the energy of the γ-ray beam. At γ-ray energies below the neutron separation threshold, the number of neutrons detected when the laser is on (N_n(on)) will be comparable to the number of background neutrons ($4 \cdot N_n$(off)).

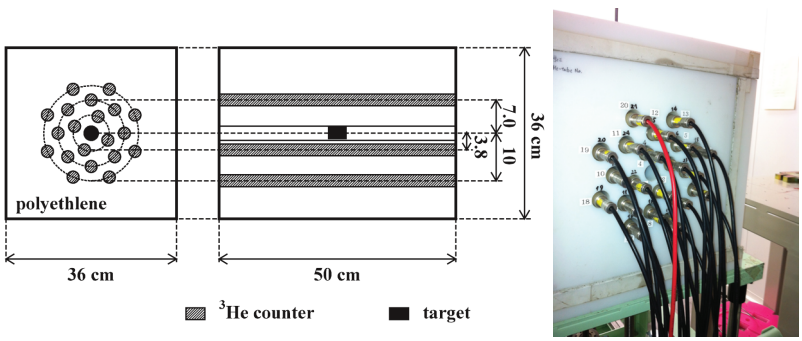

Figure 3.8: *Left panel: A schematic view of the triple-ring neutron detector, the figure is taken from Ref. [28]. Right panel: A photo of the back side of the neutron detector.*

We assume the following statistical uncertainty for when the beam is on and off respectively,

$$\begin{aligned} \Delta N_n(\text{on}) &= \sqrt{N_n(\text{on})} \\ \Delta N_n(\text{off}) &= \sqrt{N_n(\text{off})} \end{aligned} \tag{3.6}$$

The total uncertainty in the number of neutrons is then

$$\Delta N_n^2 = \Delta N_n^2(\text{on}) + 16 \cdot \Delta N_n^2(\text{off}) \tag{3.7}$$

$$\Delta N_n^2 = N_n(\text{on}) + 16 \cdot N_n(\text{off}). \tag{3.8}$$

3.5 Neutron efficiency

A ring-ratio technique, developed by Berman [29], has been used to calculate the efficiency of the neutron detector. Monte Carlo simulations have been performed to simulate the ring-ratio R as a function of neutron energy E_n [30]. The neutron detection efficiency ε_n can be deduced from the energy. The simulations have been tested with a ^{252}Cf source that was calibrated at the National Institute of Japan in AIST [30]. The measured efficiencies compare well with the simulations, as seen in Fig. 3.9.

We start by calculating the number of neutrons from each ring and the corresponding uncertainty from Eqs. (3.5) and (3.8).

$$\begin{aligned} R_{12} &= N_n^{r1}/N_n^{r2} \\ R_{23} &= N_n^{r2}/N_n^{r3} \\ R_{13} &= N_n^{r1}/N_n^{r3}, \end{aligned} \tag{3.9}$$

where the subscripts 1, 2 and 3 gives the ring number. The uncertainty of the ring ratios ΔR are calculated from error propagation,

$$\left(\frac{\Delta R_{12}}{R_{12}}\right)^2 = \left(\frac{\Delta N_n^{r1}}{N_n^{r1}}\right)^2 + \left(\frac{\Delta N_n^{r2}}{N_n^{r2}}\right)^2 \tag{3.10}$$

$$\Delta R_{12} = \sqrt{\left(\frac{\Delta N_n^{r1}}{N_n^{r1}}\right)^2 + \left(\frac{\Delta N_n^{r2}}{N_n^{r2}}\right)^2} \cdot R_{12} \tag{3.11}$$

We know how the average neutron energy depends on the ring ratio, therefore we obtain energies E_{12}, E_{23} and E_{13} for each of the ring ratios. We find the uncertainty of the energies from the uncertainty to the ring ratios, by simply adding and subtracting ΔR from R, and reading out the corresponding energy. Then the

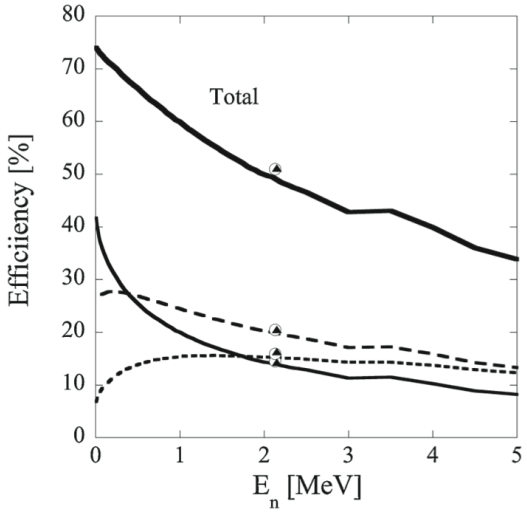

Figure 3.9: *The neutron detection efficiency of the inner most ring (thinnest solid curve), the middle ring (dashed curve), and the outer most ring (dotted curve), along with the total efficiency (thickest solid curve). The detector efficiencies measured with a* ^{252}Cf *source are represented by the open circles, in comparison to the filled triangles which are obtained with the Monte Carlo simulations. The figure is taken from Ref. [30].*

largest difference of these energies with respect to the energy calculated from R is assumed to be the uncertainty of the energy ΔE. Furthermore, we calculate the weighted average of the energies as follows,

$$E_n = \frac{\omega_{12}E_{12} + \omega_{23}E_{23} + \omega_{13}E_{13}}{\omega_{12} + \omega_{23} + \omega_{13}}, \tag{3.12}$$

where $\omega = 1/\Delta E$, for each of the rings. Once the energy is obtained one finds the corresponding efficiency from the simulations. The calculated ring-ratios and corresponding efficiencies for ^{144}Nd is given in Fig. 3.10.

According to Ref. [30], the uncertainty of the neutron detection efficiency is found to be 3.2% of the absolute emission rate of a ^{252}Cf source. This uncertainty is used for the experiments presented in this work.

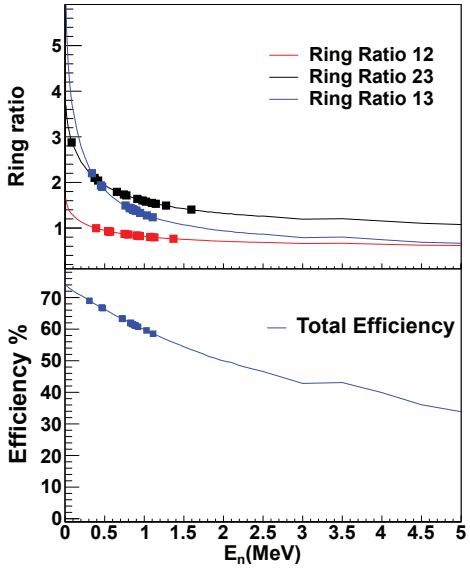

Figure 3.10: *Variation of the ring ratio with neutron energy for* ^{144}Nd, *and the corresponding efficiency of the neutron detector. The solid lines represent the simulations, while the squares give the values deduced from the measurements.*

3.6 Measuring the γ-ray flux

A $5'' \times 6''$ NaI detector was used to measure the LCS γ-ray flux. The γ detector is mounted in the wall behind the neutron detector, as seen in the photo in Fig. 3.11. For each run we record the γ-ray spectra, when the laser is on full power mode. Multiple photons will often be detected simultaneously, which will result in a pile-up spectrum. Before or after each measurement the laser power is reduced in order to obtain a single photon spectra, where it is most likely to measure only one photon at a time. Figure 3.12 shows a typical pile-up spectrum and single-photon spectrum, after background subtraction. From these two spectra we determine the number of γ rays incident on the NaI detector as follows, where $\langle i \rangle = (\sum x_i n_i)/(\sum n_i)$, gives the average channel of the pile-up and single-photon spectrum, and n_i is the number of counts in the i'th channel;

$$N_{\gamma,\text{detected NaI}} = \frac{\langle i \rangle_{\text{pile up}}}{\langle i \rangle_{\text{single}}} (\sum n_i)_{\text{pile up}}. \tag{3.13}$$

Figure 3.11: *The ^{3}He neutron detectors are embedded in the white polyethylene in front, and a NaI detector is located in the wall behind.*

For more details on the derivation of Eq. (3.13), see Ref. [31].

To determine the number of γ rays incident on the target N_γ, we have to account both for attenuation in the target itself and for attenuation in the NaI detector. As the targets are quite thick, of the order ~ 2 g/cm^2, the attenuation in the target is significant, around $2-3\%$ of the γ rays will be affected. The number of γ rays exiting the target will be

$$N_{\gamma,\text{after target}} = N_\gamma \cdot \exp\left[-\frac{\mu_\text{t}}{\rho_\text{t}} t_\text{t}\right], \tag{3.14}$$

where t_t gives the target thickness, and $\frac{\mu_\text{t}}{\rho_\text{t}}$ represents the mass attenuation coefficient, tabulated in Ref. [32]. All of the target nuclei was made of oxide material, in general the attenuation of a compound is given by

$$\frac{\mu}{\rho} = \sum_i w_i \frac{\mu_i}{\rho_i}, \tag{3.15}$$

where the summation is over the constituents of the compound, and w_i gives the fraction of each constituent to the total amount. Furthermore, the number of γ rays stopping in the NaI detector is given by

$$N_{\gamma,\text{detected NaI}} = N_{\gamma,\text{after target}} \cdot \left(1 - \exp\left[-\frac{\mu_\text{NaI}}{\rho_\text{NaI}} t_\text{NaI}\right]\right). \tag{3.16}$$

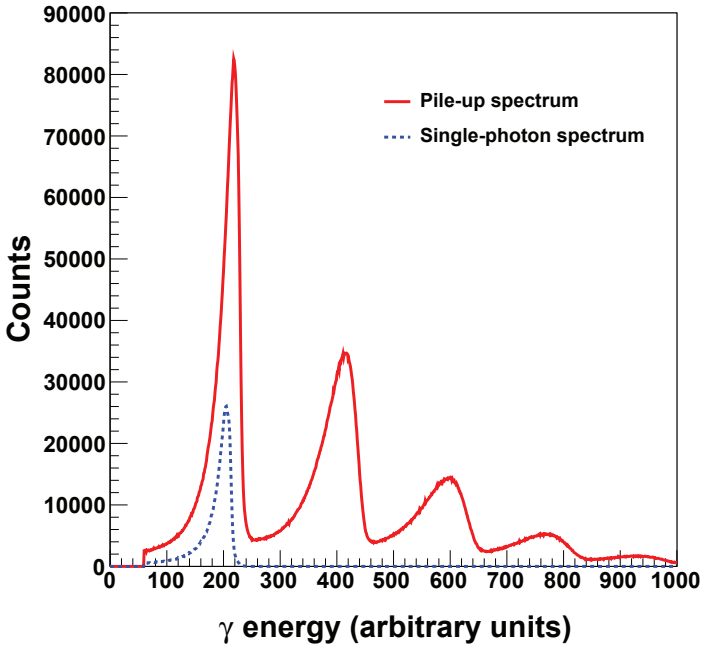

Figure 3.12: *The solid line gives the pile-up spectrum corresponding to a γ beam centered around energy* 12.59 *MeV. The dashed line represents the single photon spectrum taken at the same energy. For the above figure the background is subtracted for both the pile-up spectra and single-photon spectra.*

This results in the following expression for the total number of γ rays incident on the target:

$$N_\gamma = \frac{N_{\gamma,\text{detected NaI}}}{\exp\left[-\frac{\mu_t}{\rho_t}t_t\right]\left(1-\exp\left[-\frac{\mu_{\text{NaI}}}{\rho_{\text{NaI}}}t_{\text{NaI}}\right]\right)}. \tag{3.17}$$

The estimate of the number of incident γ rays depends on the linearity of the response of the γ-ray monitor detector to the pile-up γ rays. A statistical analysis of the pile-up spectra was performed in Ref. [33], and the uncertainty in the number of γ-rays was estimated to be 3%.

3.7 The monochromatic cross section

The monochromatic cross section can be deduced after calculating all the constituents of Eq. (3.3). A typical result is shown for ^{147}Sm in Fig. 3.13. The blue arrow indicate the neutron separation energy of the nucleus.

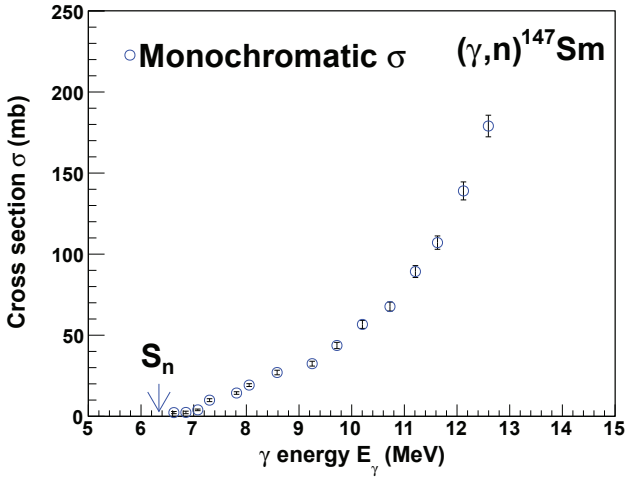

Figure 3.13: The monochromatic (γ, n) cross section of ^{147}Sm.

Chapter 4

Particle-γ experiments

For this thesis data from ^{105,106}Pd and ^{163,164}Dy have been studied through particle-γ coincidence measurements performed at the Oslo Cyclotron Laboratory (OCL). The experiments were conducted in 2006 and 2010, respectively. From the data recorded we have extracted the radiative strength function below the neutron threshold S_n, in addition to the level density at low temperatures ($T < 1$ MeV), using the Oslo method. The experimental setup and data extraction technique will be outlined in the following chapter.

4.1 The Oslo Cyclotron Laboratory

The Oslo Cyclotron Laboratory (OCL) is a part of the *Center for accelerator based research and energy physics (SAFE)*. Most of SAFE's activities are centered around research performed at this laboratory, which serves as an experimental center for various fields of research and applications. Until recently it has been used in production of radioactive isotopes to be used for medical diagnostics at the Norwegian Radium Hospital in Oslo. Currently it is used for research purposes in the field of nuclear medicine. The laboratory is also used extensively for basic research within nuclear physics and nuclear chemistry.

The cyclotron is of type Scanditronix MC-35, and it has been operating since 1979. The accelerator can deliver pulsed light-ion beams, namely ^{1}H and ^{2}H, in addition to ^{3}He and α particles. A schematic overview of the laboratory and its target stations is given in Fig. 4.1. The location labeled CACTUS/SiRi is where the nuclear physic experiments take place, which will be discussed in the following section.

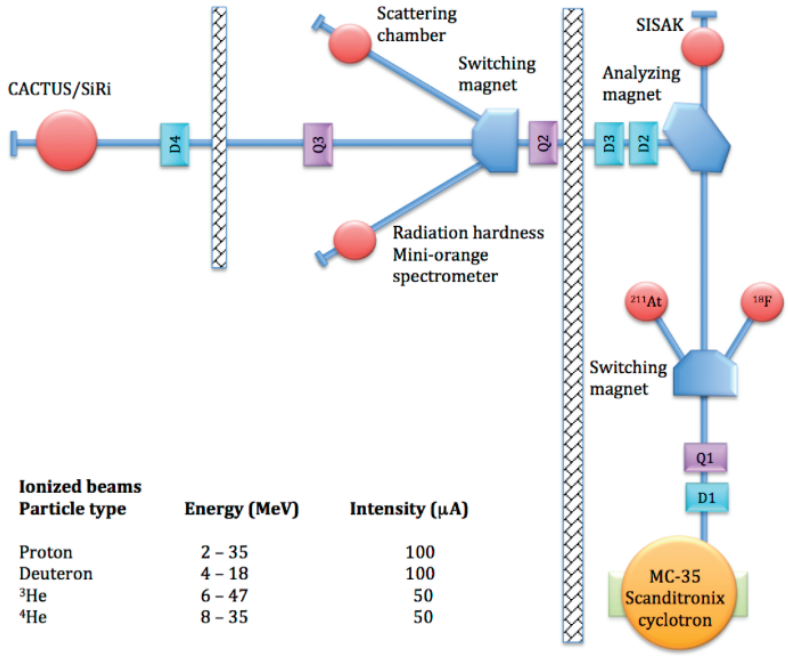

Figure 4.1: *An overview of the OCL with its target stations. The figure is taken from Ref. [34].*

4.2 Experimental setup

The targets, ^{164}Dy and ^{106}Pd, were irradiated with a beam of ^{3}He and the inelastic $(^{3}\mathrm{He},^{3}\mathrm{He}')$ reaction and the pick-up $(^{3}\mathrm{He},\alpha)$ reaction were studied. The corresponding Q-values for the reactions are given in Table 4.1. Particle-γ coincidences were measured with the CACTUS γ-ray array [35], and the Silicon Ring (SiRi) particle telescope system [36].

The particle telescopes are mounted on a ring inside the CACTUS detector frame. For the dysprosium experiment, the silicon detectors were made up of 8 ΔE counters of thickness $\sim 150\ \mu$m, each placed in front of a 1500 μm E detector, for ΔE-E particle determination [35]. The telescopes were placed in an angle of 45° relative to the beam axis.

Later, the silicon detectors have been upgraded and used for the palladium experiment [36]. In the present setup, each of the front counters are segmented

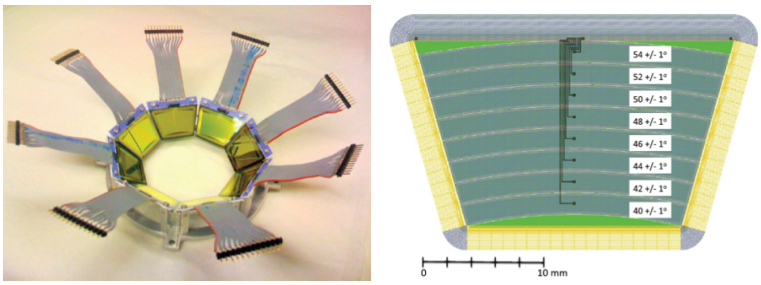

Figure 4.2: *A picture of the silicon ring (left panel), and an illustration of the segmented ΔE detectors (right panel).*

into 8 strips with a thickness of 130 μm, in front of 1550 μm thick E detectors, see Fig. 4.2. In total, the new SiRi has 64 ΔE-E detectors. The segmented front counters cover angles of $40^\circ - 54^\circ$, when placed in forward direction, as illustrated in Fig. 4.2. The new ring makes an angle of 47° with the beam axis. The new SiRi system gives improved energy resolution due to less spread in scattering angle. In addition, there is a much larger solid angle coverage of $\approx 8\%$ compared to the old setup with $\approx 1\%$ of 4π. As a result we have a higher detection efficiency.

In front of the detector modules, an aluminium foil is placed to shield the ΔE detectors from δ-electrons, with thickness of 10.5 μm and 19 μm, for the new and old setup, respectively [35, 36].

CACTUS consists of 28 NaI(Tl) detector of size $5'' \times 5''$, which can be seen on the picture of Fig. 4.3. The NaI(Tl) detectors are mounted on a spherical frame, and lead collimators are placed in front to reduce Compton events. The total efficiency of the NaI(Tl) detectors is measured to be 15.2% at a γ energy of 1.3 MeV. The relative energy resolution is $\approx 6\%$ for 1.3 MeV γ-rays.

4.3 Particle identification

We aim to study particle-γ coincidences which stem from the same nuclear reaction. To be able to distinguish the nuclear reactions taking place, we have to identify the various charged ejectiles produced. The particles will loose energy mainly due to ionisation of the atoms in the crystal. The Bethe-Block formula [37] describes how charged particles deposit energy in a medium,

$$-\frac{dE}{dx} = 2\pi N_a r_e^2 m_e c^2 \rho \frac{Z}{A}\frac{z^2}{\beta^2}\left[\ln\left(\frac{2m_e\gamma^2 v^2 W_{max}}{I^2}\right) - 2\beta^2\right], \qquad (4.1)$$

Figure 4.3: *A picture of the γ-detector array, named CACTUS. The 28 NaI detectors are seen mounted on the outside of the sphere.*

where N_a is Avagadros number ($6.022 \cdot 10^{23}$ mol^{-1}), r_e is the classical electron radius ($2.817 \cdot 10^{13}$ cm) and m_e is the mass of the electron, z is the charge of the incoming particle, Z, A and ρ are the atom number, mass number and the density, respectively, of the absorbing material. The factor β is given by $\beta = v/c$, where v is the speed of the particle and c is the speed of light. The factor γ is given by $\gamma = 1/\sqrt{1-\beta^2}$. The mean excitation potential is denoted by I, while the maximum energy transferred in a single collision is given by W_{max}.

From Eq. (4.1) it follows that the mass and charge of a particle will influence the energy deposition, and that the energy deposition increases when a charged particle is slowing down. When plotting the energy deposition in the front detector versus the energy deposition in the end detector, a unique banana-shaped curve is found for each charged particle type. Such a plot is given in Fig. 4.4, generated by a beam of 38 MeV ^{3}He particles on a ^{106}Pd target. The uppermost curve represents the α particles, while the curve below belongs to ^{3}He ejectiles, in the latter curve we observe a peak located at approximately 33 MeV in the end detector. This peak corresponds to the elastic ^{3}He peak. Diagonal to this peak we observe a *tail*, which is most likely due to a small amount of ejectiles channeling through the polycrystalline structure of the front detector. As a result too little energy is deposited in the front detector. The sharp vertical line seen in the spectrum above the elastic peak corresponds to the case when δ-electrons deposit energy

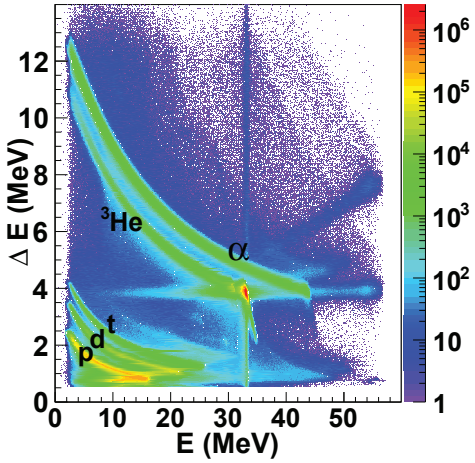

Figure 4.4: *Energy deposited in the front detector versus energy deposited in the end detector, for a* ^{106}Pd *target exposed to a* 38 *MeV* ^{3}He *beam.*

in the front detector along with elastically scattered ^{3}He-particles. Below the elastic peak there is another vertical line that originates when some of the energy deposited in the front detector is not collected. Similarly the horizontal line to the left of the peak is due to failure in collecting all the energy in the end detector. At the bottom left of Fig. 4.4, curves corresponding to tritons, deuterons and protons are observed.

Nucleus	Reaction	Q-value (MeV)
^{163}Dy	$(^{3}\mathrm{He}, \alpha\gamma)$	12.92
^{164}Dy	$(^{3}\mathrm{He}, ^{3}\mathrm{He}\gamma)$	-
^{105}Pd	$(^{3}\mathrm{He}, \alpha\gamma)$	11.02
^{106}Pd	$(^{3}\mathrm{He}, ^{3}\mathrm{He}\gamma)$	-

Table 4.1: *Reactions of interest and corresponding Q-values.*

4.3.1 The thickness spectrum

The range $R(E)$ of a particle describes how far a particle can penetrate in a medium as a function of energy. From the known range functions we can derive a thickness spectrum, which gives the observed thickness of the front detector as a function of particle type. This is achieved by subtracting the range of the particle in the end detector from the total range of the particle,

$$d_{\text{front}} = R(\Delta E + E) - R(E), \tag{4.2}$$

where ΔE and E give the energy deposited in the front and end detector, respectively. The ^{3}He peak in Fig. 4.5 corresponds to the true thickness of the front detector. From the thickness spectrum we can set gates for the ^{3}He and α particles, which are used in subsequent data sorting routines to extract the α-γ and ^{3}He-γ coincidences.

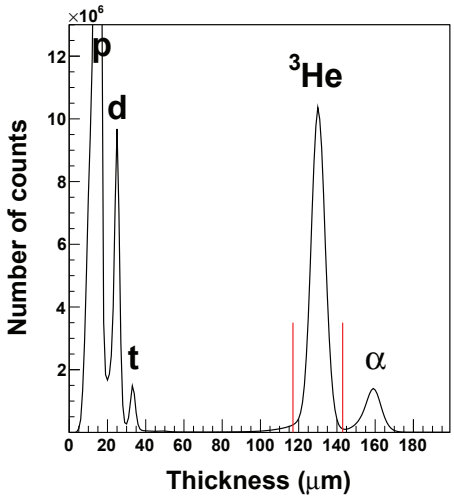

Figure 4.5: *The thickness spectrum used to set gates on the particle types. The vertical lines give the gates set on the ^3He particles to study ^{106}Pd. Peaks due to protons, deuterons and tritons can also be seen, in addition the α-peak.*

4.3.2 The time spectrum

We have used a time-to-digital converter (TDC) for each of the NaI(Tl) detectors. A start signal is generated when a charged particle is detected in the silicon detectors, and a stop signal is created when a γ ray is registered in the NaI(Tl) detectors. A delay of ~ 400 ns is set on the stop signal, which results in a prominent peak in the time spectrum, see Fig. 4.6. Since the beam pulse period is smaller than the time window, we will generate false coincidences where the particle and γ do not steam from the same beam pulse. These are seen as the smaller peaks in Fig. 4.6. We expected a background of false coincidences also underlying the prominent peak, and therefore we subtract a background of this order of magnitude, see Fig. 4.6.

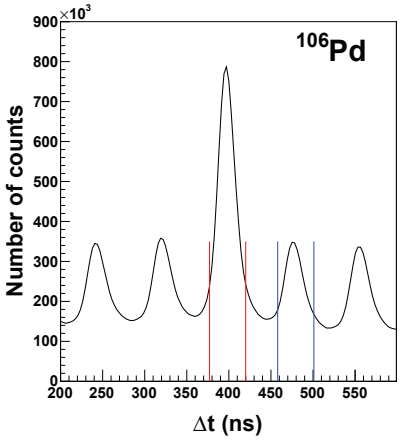

Figure 4.6: *The time spectrum of ^{106}Pd, the vertical lines show the gates set on the prompt peak (red lines) and random peak (blue lines).*

4.4 Coincidence matrices

Each individual particle telescope and NaI detector is calibrated by assuming a linear correlation between the true energy and the channel number

$$E = a_0 + a_1 \cdot \mathrm{ch}, \tag{4.3}$$

where E is the energy, a_0 is the constant shift, a_1 represents the dispersion and ch gives the channel number in the spectrum. After calibrating all the detectors

properly, one can add the data of all the particle telescopes together, and likewise the NaI spectra. Furthermore, when the gates are sett in the thickness spectrum on a specific particle, and appropriate gates in the time spectrum to define coincidences, the data are sorted into particle-γ ray matrices. The coincidence matrix for ^{105}Pd is displayed in Fig. 4.7. The neutron threshold S_n for ^{105}Pd is 7094.1 keV. It is interesting to see that there is no abrupt change in the matrix when the neutron channel is opened. Considering the final nucleus in the reaction $^{105}\mathrm{Pd}(^3\mathrm{He}, \alpha n\gamma)^{104}\mathrm{Pd}$, the first excited state is a 2^+ located at 556 keV, whilst the next state is a 4^+ state at 1324 keV. As the $(^3\mathrm{He}, \alpha)$ reaction favours high-l transfer in general, the populated states very likely have an average spin larger than 2. Thus, there is an effective spin hindrance which could explain the observed behaviour in the coincidence matrix.

For the further analysis the true γ-ray energy has to be determined from the known detector response. Details of this procedure will be given in the upcomming section.

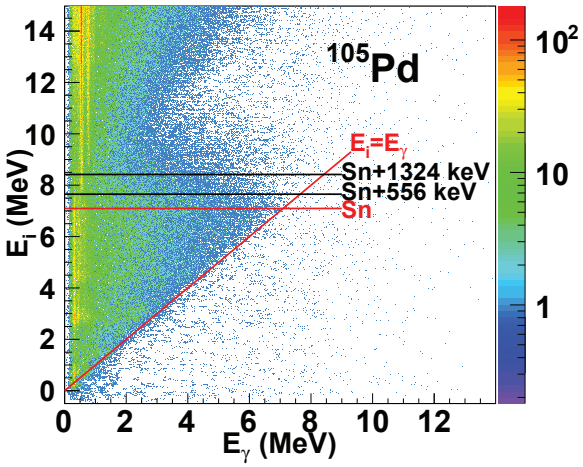

Figure 4.7: *The coincidence matrix of* ^{105}Pd. *The diagonal red line represents where the excitation energy equals the* γ*-ray energy. The horizontal red line illustrates the neutron separation threshold, while the horizontal black lines represent at what excitation energies the first and second excited states in* ^{104}Pd *are located.*

4.5 Unfolding γ spectra

Gamma rays interact with matter in various ways. There are three dominating processes: photoelectric effect, Compton scattering and pair production. In cases where all the energy of a incoming γ ray is absorbed (through one or multiple processes) it will contribute to the full energy peak. If the γ ray is scattered by an electron with partial energy loss out of the detector, we will register an event in the Compton region. We also observe a single- and double escape peak in the registered spectrum, where γ rays have undergone pair production creating an electron-positron pair. The positron is quickly annihilated, and if one or two of the resulting 511 keV γ rays escape the detector, they will contribute to the single- and double escape peak, respectively. We also observe a 511 keV peak due to background annihilation radiation, in addition to a $\approx$200 keV peak from backscattering γ rays.

Unfortunately, the processes leading to energy loss in the detector occurs rather frequently. A peak-to-total ratio is often $< 50\%$ [38]. A folding iteration method is therefore used to convert the detected γ-ray spectrum into the true spectrum. To use this method we need to know how the detector responds to γ rays of a wide energy range.

4.5.1 Detector response

The response function $R(E,E_\gamma)$ gives the amount of energy E deposited in the detector for γ rays of energy E_γ. The response function is measured for several in-beam γ lines from excited states in ^{13}C, ^{16,17}O, ^{28}Si and ^{56,57}Fe where the relative detector efficiency as function of γ energy could be extracted in a reliable way [**?**]. Furthermore, an interpolation procedure is used between these energies in order to obtain the response function for all energies E_γ. Note that while the unfolding procedure follows the method described in Ref. [38], the response functions have recently been remeasured, also the detector efficiencies are changed. Therefore, the information in Table 1 of Ref. [38] should be overlooked, and replaced with the values given in Appendix A [39], for the newest data, namely the ^{105,106}Pd nuclei.

To simplify the interpolation procedure, the full energy, single- and double escape and annihilation peaks are removed from the measured spectra [38]. Later, Gaussian distributions will be added at the interpolated peak positions, with proper intensities and energy resolution [38].

The energy of a Compton scattered electron is given by,

$$E_e = E_\gamma - \frac{E_\gamma}{1+\frac{E_\gamma}{m_e c^2}(1-\cos\theta)}, \tag{4.4}$$

where θ is the scattering angle, m_e is the rest mass of the electron and c represents the speed of light. When interpolating the Compton background, this is performed for channels with the same scattering angle, using the following expression,

$$c(E) = \left(\frac{dE}{D\theta}\right)_{E_\gamma} \left[c_1(E_1) \left(\frac{dE}{D\theta}\right)_{E_{\gamma,1}} + \frac{E_\gamma - E_{\gamma,1}}{E_{\gamma,2} - E_{\gamma,1}} \right. \tag{4.5}$$

$$\left. \cdot \left(c_2(E_2) \left(\frac{dE}{D\theta}\right)_{E_{\gamma,2}} - c_1(E_1) \left(\frac{dE}{D\theta}\right)_{E_{\gamma,1}} \right) \right]. \tag{4.6}$$

The quantities E_γ, $E_{\gamma,1}$ and $E_{\gamma,2}$ represents the maximum energies of the Compton spectrum for the interpolated spectrum end the reference spectra, respectively, while the values E, E_1 and E_2 gives the corresponding energies that the electron deposits as a function of scattering angle.

From Eq. (4.4) we see that the maximum energy transfer is achieved for $\theta = 180°$. In Fig. 4.8 we se a sharp drop in the number of counts for electron energies corresponding to this value. However, there are also some counts above this edge. These stem from γ rays undergoing two or more Compton scattering interactions. These channels are added one by one and interpolated [38]. In addition, we observe a broad peak in the γ spectrum around $\sim$200 keV. This is due to backscattering, X-rays and other background events. Here, interpolation is performed between the same channel numbers. If we use a response function with the experimental energy resolution, this will result in artificial undershoots on both sides of pronounced peaks [38, 39]. It is found that the best result is obtained with a response matrix with an energy resolution to 10% of the experimental one[1], $\text{FWHM}^{\text{resp}} = 0.1 \cdot \text{FWHM}^{\text{exp}}$.

4.5.2 The folding iteration proceedure

The response function is normalized by $\sum_i R_{ij} = 1$, where channel i represents the response (amount of energy deposited), when a γ ray of energy corresponding to channel j hits the detector. The folded spectrum f can be calculated a follows,

$$f = \mathbf{R}u, \tag{4.7}$$

where u represents the unfolded spectrum. A straight forward way of calculating the spectra would be to take the inverse matrix $\mathbf{R}^{-1}$ and multiply with the observed spectrum [40, 41]. However, taking the inverse of the response matrix could cause huge fluctuations. Therefore, we use a folding iteration method instead, which consists of the following steps [38]:

[1] In Ref. [38], the resolution of the response matrix was set to 50% of the experimental one, but this has been altered and 10% is used in the analysis of the palladium data.

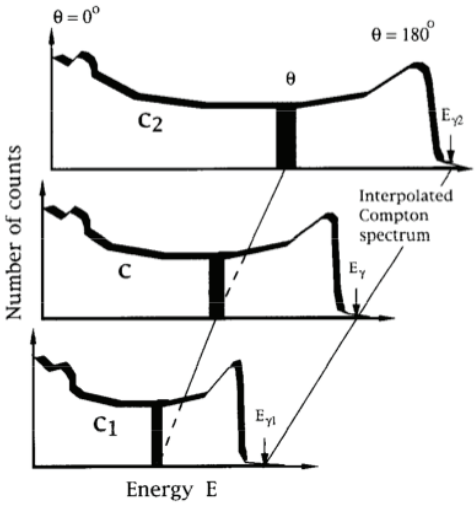

Figure 4.8: *Illustration of the interpolation of the Compton part of the measured response functions c_1 and c_2. The figure is taken from Ref. [38].*

1. As a trial function for the unfolded spectrum u^0 we start with the observed one r, $u^0 = r$.

2. We calculate the folded spectrum, $f^0 = \mathbf{R}u^0$.

3. The next trial function will be the difference $r - f^0$ added to the original trial function u^0, $u^1 = u^0 + (r - f^0)$.

4. We continue by folding u^1 to obtain f^1 which is again used to obtain the next trial function. This is repeated until f^i reproduces r, within the experimental fluctuations.

4.5.3 The Compton subtraction method

While the first trial function $u^0 = r$ has the fluctuations of the observed spectrum, the fluctuations will increase and propagate for each iteration. Therefore, the Compton subtraction method is developed to smooth the Compton contribution, before subtracting it from the observed spectrum. As a result we will obtain an unfolded spectrum with the same fluctuations as the observed one. We start with the unfolded spectrum obtained from the folding iteration procedure. The

observed spectrum containing all but the Compton contribution is defined as [38],

$$v(i) = p_f(i)u_0(i) + w(i), \tag{4.8}$$

where the first term represents the full energy contribution, followed by $w(i) = u_s + u_d + u_a$, which gives the single- and double escape peak and annihilation peak, respectively. These three terms are given by,

$$u_s(i - i_{511}) = p_s(i)u_0(i) \tag{4.9}$$
$$u_d(i - i_{1022}) = p_d(i)u_0(i) \tag{4.10}$$
$$u_a(i_{511}) = p_a(i)u_0(i). \tag{4.11}$$

The probabilities p_s, p_d and p_a for single- and double escape peak and annihilation peak, respectively, are estimated from the measured monoenergetic transitions.

The u_a spectrum is smoothed with an energy resolution of 1 FWHM to attain the energy resolution of the observed spectrum. Whereas, u_f, u_s and u_d have an energy resolution determined from the observed spectrum (1 FWHM) and of the response matrix (0.1 FWHM), namely $\sqrt{1^2 + 0.1^2}$ FWHM $= \sqrt{1.01} \approx 1$ FWHM.

After smoothening the spectra we extract the Compton background $c(i)$ from the observed spectra $r(i)$,

$$c(i) = r(i) - v(i). \tag{4.12}$$

We know that $c(E)$ should be a slowly varying function of energy. We therefore can us a strong smoothening to obtain a resolution of 1 FWHM. Finally, the smoothed Compton spectra and peak structures are subtracted from the observed spectra, and the γ- ray energy distribution is corrected for full energy probability p_f and the detection efficiency [38],

$$u(i) = \frac{r(i) - c(i) - w(i)}{p_f(i)\varepsilon_{\text{tot}}(i)}. \tag{4.13}$$

4.6 Extracting the primary γ-ray matrix

From the unfolded γ-ray spectra, we may now obtain the distribution of the primary γ rays emitted in each decay cascade. We cannot experimentally resolve the time between the γ rays stemming from the same cascade, therefore we do not know in which order they were emitted. When measuring γ rays the only information we have is at which initial excitation energy the associated γ decay cascades originated. If each excitation energy bin had an equal chance of direct population, we could find the primary γ rays by subtracting the spectra of the underlying bins,

$$h_i = f_i - \sum_0^i w_{ij} f_j, \tag{4.14}$$

where h_i gives the primary γ rays at the initial excitation energy bin i, f denotes unfolded spectra, and w_{ij} is an unknown coefficient that gives the probability of decay from states in bin i to states in bin j. This factor is normalized such that $\sum_i w_{ij} = 1$, which gives the branching ratios as a function of excitation energy. In other words, w_i gives the primary γ ray spectrum h_i at bin i.

However, we know that the excitation levels populated in direct reactions is not a random process. For reactions induced with the ^{3}He beam for example, vibrational states with relatively high angular momentum have a high cross section to be populated. To account for this we must introduce a new factor n_{ij}, that when multiplied with each spectra f_i, gives the same number of cascades. Adding this to Eq. (4.14) we obtain the following expression for calculating the primary γ rays,

$$h_i = f_i - \sum_0^j w_{ij} n_{ij} f_j. \tag{4.15}$$

In the following we will describe two techniques we can use to obtain the normalisation factor.

- Singles normalisation To account for the different cross sections when populating the energy bins, we can use the singles particle spectrum. Since this spectrum is proportional to the reaction yield it also gives the number of cascades decaying from this bin. The population of one level i relative to a level j is found by dividing the number of counts S in the single particle spectra,

$$n_{ij} = \frac{S_i}{S_j}. \tag{4.16}$$

- Multiplicity normalisation The average γ ray multiplicity gives the average number of γ rays in the cascades. We can express the average γ-ray energy $\langle E_{\gamma,i} \rangle$ decaying from a energy level i by the following expression

$$\langle E_{\gamma,i} \rangle = \frac{E_i}{\langle M_i \rangle}, \tag{4.17}$$

  where E_i is equal to the total energy carried by the γ rays (equal to the energy of the populated bin), and $\langle M_i \rangle$ is the average multiplicity from this level. Rearranging Eq. (4.17), we have the following expression for the multiplicity,

$$\langle M_i \rangle = \frac{E_i}{\langle E_{\gamma,i} \rangle}. \tag{4.18}$$

Furthermore, the single particle cross section S_i is equal to the area of spectrum f_i (the number of cascades) $A(f_i)$ divided by the multiplicity, $S_i = A(f_i)/\langle M_i \rangle$. Incerting this onto Eq. (4.16), we obtain,

$$n_{ij} = \frac{A(f_i)/\langle M_i \rangle}{A(f_j)/\langle M_j \rangle}. \tag{4.19}$$

The two normalisation methods have been thoroughly tested and compared in Ref. [43]. It was found that they normally give very similar results that agree within the error bars. An exception however is in the presence of some isomeric states, where the multiplicity method must be used to obtain the correct result [43].

The area of the primary γ-ray matrix should be equal to the area of the observed spectrum minus the area of the sum in Eq. (4.15). However, this is not always the case, due to an improper choice of the weighting function w. To compensate for this we introduce an area correction [42],

$$A(h_i) = A(f_i) - \delta A(g_i), \tag{4.20}$$

where $g_i = \sum_0^j w_{ij} n_{ij} f_i$, and δ is a small correction. This corresponds to a γ-ray multiplicity of one unit. The same value can be expressed by,

$$A(h_i) = \frac{A(f_i)}{\langle M_i \rangle}. \tag{4.21}$$

When combining Eqs. (4.20,4.21), we obtain,

$$\delta = (1 - 1/\langle M_i \rangle)\frac{A(f_i)}{A(g_i)}. \tag{4.22}$$

The correction parameter δ is varied to obtain the best agreement between the areas of h_i, f_i and g_i. However, we restrict the correction to be maximum 15%.

4.6.1 Assumption of the primary γ-ray method

For the primary γ-ray method to be valid, it is essential that decay from any excitation level is independent of how the nucleus was excited to this bin, whether they were initiated directly by the nuclear reaction or by γ decay from higher-lying states. In the region of high level density, the nucleus seems to attain a compound-like system before emitting γ rays, even though direct reactions are utilized. This is fulfilled because a significant configuration mixing of the levels will appear when the level spacing is comparable to the residual interaction. And because the

formation of a complete compound state is as fast as $\sim 10^{-18}$ s, significantly less than the typical life time of a state in the quasi-continuum which is $\sim 10^{-15}$ s. Therefore, the assumption is believed to be reasonable, and the decay process is at least mainly statistical.

4.6.2 The iteration procedure

Since w is identical to the primary γ-ray spectrum h, we can determine both through an iterative procedure [42]. The steps are as follows:

1. Apply a trial function for w_{ij}.
2. Deduce h_i.
3. Extract new w_{ij} functions from h_i by giving both variables the same energy calibration, and normalize the area of h_i to unity.
4. If $w_{ij}(\text{new}) \approx \text{w}_{\text{ij}}(\text{old})$, convergence is achieved, if not repeat from step 2.

The resulting primary γ-ray spectra are not sensitive to the starting trial function [43], and one could for instance start with the total unfolded spectrum. The procedure is fast converging, usually $10-20$ iterations are performed on each experimental spectrum [43].

The entire landscape of the primary γ-ray matrix, as seen in Fig. 4.9, can then be disentangled into a product of two functions each of one variable. The extraction of the level density $\rho(E)$ and the RSF $f(E_\gamma)$ is described in detail in the next chapter.

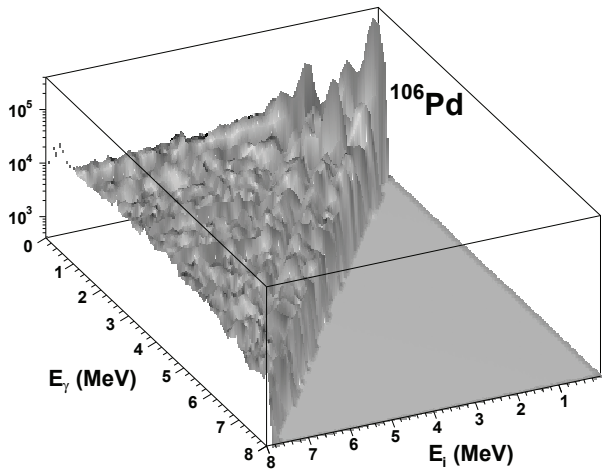

Figure 4.9: *The primary γ-ray matrix of* ^{106}Pd.

Chapter 5

Data analysis

In this chapter an outline of the data analysis methods used to extract the various functions will be given. The particle-γ coincidences have been analysed using the so-called Oslo method [45]. The non-monochromatic photo-neutron data are evaluated by use of a Taylor expansion method [46], which takes into account the energy spread of the γ-ray beam.

5.1 Extracting non-monochromatic cross sections

For the NewSUBARU experiments, we have so far assumed the monochromatic approximation which implies a sharp energy of the γ-ray beam. The photo neutron cross section can be expressed as follows,

$$\int_{S_n}^{E_{\max}} n_\gamma(E_\gamma)\sigma(E_\gamma)dE_\gamma = \frac{N_n}{N_t N_\gamma \xi \varepsilon_n g}, \tag{5.1}$$

where $n_\gamma(E_\gamma)$ gives the normalized energy distribution of the γ-ray beam, and $\sigma(E_\gamma)$ is the photo-neutron cross section we wish to determine. Furthermore, N_n represents the number of neutrons detected, N_t gives the number of target nuclei per unit area, N_γ is the number of γ rays incident on target, ε_n represents the neutron detection efficiency, and finally $\xi = (1-e^{\mu t})/\mu t$ is a correction factor for self attenuation in the target, where t is the target thickness. The factor g represents the fraction of γ flux above the neutron threshold S_n,

$$g = \frac{\int_{S_n}^{E_{\max}} n_\gamma(E_\gamma)dE_\gamma}{\int_0^{E_{\max}} n_\gamma(E_\gamma)dE_\gamma}. \tag{5.2}$$

As a first approximation we assume a sharp energy distribution of the γ-ray beam, by replacing the γ energy distribution $n(E_\gamma)$ in Eq. (5.1) by a delta function,

$\delta(E_\gamma - E_{\text{av}})$. Here E_{av} is the average energy of the LCS γ beam,

$$E_{\text{av}} = \int_{S_n}^{E_{\text{max}}} E_\gamma n_\gamma(E_\gamma) dE_\gamma. \tag{5.3}$$

We obtain the following cross section in the monochromatic approximation,

$$\sigma^{\text{mono}}(E_{\text{av}}) = \frac{N_n}{N_t N_\gamma \xi \varepsilon_n g}. \tag{5.4}$$

The next step is to correct for the energy spread of the γ-ray beam. A Taylor expansion method is adapted to solve the integral of Eq. (5.1) with respect to $\sigma(E)$, according to Ref. [46]:

$$\sigma(E_{\text{av}}) + \sum_i s_i(E_{\text{av}}) = \frac{n_n}{N_t N_\gamma \xi \varepsilon_n}, \tag{5.5}$$

where

$$s_i(E_{\text{av}}) = \frac{1}{n!}\sigma^{(i)}(E_{\text{av}}) \int_{s_n} n_\gamma(E_\gamma - E_{\text{av}})^i. \tag{5.6}$$

where $\sigma^{(i)}(E_{\text{av}})$ represents the i'th derivative of $\sigma(E_{\text{av}})$. For details of the Taylor series, see Appendix C. Now, the aim is to find the cross section as a function of energy, however in order to do so one must assume an energy dependence in order to calculate the s_i terms, hence an iteration procedure must be made. The iteration procedure contains the following four steps:

1. We use the monochromatic cross section found from Eq. 5.4 as our starting point $\sigma_{(0)}(E_{\text{av}}) = \sigma_{\text{mono}}(E_{\text{av}})$, and fit to a Lorentzian function,

   $$\sigma(E) = \sigma_c \left(\frac{E - S_n}{S_n}\right)^p \frac{1}{1 + (E^2 - E_R^2)^2/(E^2\Gamma^2)}, \tag{5.7}$$

   where σ_c, p, E_R and Γ are treated as free parameters, as done in Ref. [30].

2. The fitted function $\sigma(E)$ is further divided into small regions of 300 keV, each region is fitted by a third order polynomial.

3. The third order polynomials are in turn used to calculate the derivatives $\sigma^{(i)}(E_{\text{av}})$, of Eq. (5.6).

4. Combining Eq. (5.4) and (5.5), we solve for $\sigma(E_{\text{av}})$,

   $$\sigma_{(1)}(E_{\text{av}}) = \sigma_{\text{mono}}(E_{\text{av}}) + S_2(E_{\text{av}}) + S_3(E_{\text{av}}). \tag{5.8}$$

   The calculated photoneutron cross section $\sigma_{(1)}(E_{\text{av}})$ is used for the next iteration, and we continue until convergence is achieved.

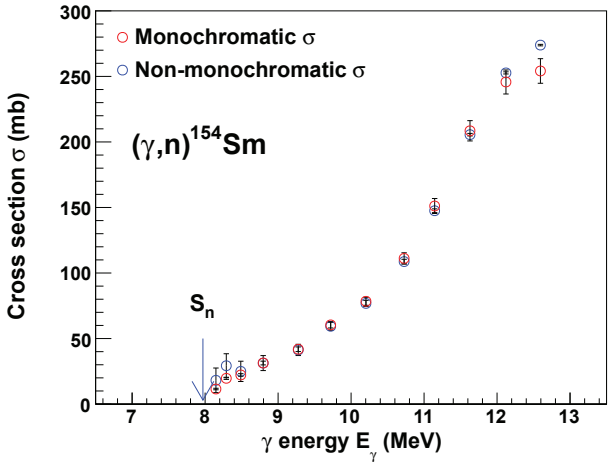

Figure 5.1: *The calibrated monochromatic and non-monochromatic* (γ,n) *cross section of* ^{154}Sm.

By taking the detour of finding the third order polynomial, instead of simply using the best fit function of Eq. (5.7), the higher order terms vanish in Eq. (5.5), because $\sigma^{(i)}(E_{\mathrm{av}}) = 0$, for $i > 3$. Also the s_1 term is omitted, as this will cancel out, see Appendix B for details. We find that the series converges rather fast, usually within $5-10$ iterations.

The cross sections have been normalized to cross sections retrieved from a ^{197}Au measurement as the standard for photoneutron cross sections [30]. The ^{197}Ag target sample had a purity of 99.99%, a thickness of 4.00 mm and a diameter of 10.0 mm. A comparison between three measured cross sections found at γ energies 8.6, 9.08 and 10.18 MeV was compared to corresponding cross sections published in Ref. [30].

The energy spread of the γ beam is indeed very narrow, and the overall correction for the energy spread of the γ beam is small. Only cross sections located at the highest average energy obtain a significant correction, as seen in Fig. 5.1.

5.2 The Oslo Method

The Oslo method is a method that enables us to extract both the level density and the radiative strength function from one experiment [45]. These functions are

extracted below the neutron separation threshold for a low spin region ($0-6\ \hbar$). The basic concept behind the method was first presented by L. Henden *et. al.* [49] in 1995, while the first attempt to solve the problem iteratively was presented by T. S. Tveter shortly after. However, the first complete and successive method to extract the two functions were presented by A. Schiller *et. al.* in 2000 [45]. The method has gradually been developed and has resulted in many publications.

The starting point of the data extraction is the primary γ-ray matrix $P(E_i, E_\gamma)$. The exited nucleus will decay through a number of γ decay cascades down to the ground state. Utilizing a subtraction technique as discussed in Chapter 3, we extract the primary γ rays emitted in each decay cascade, for each excitation energy bin. The primary γ-ray matrix corresponds to the probability distribution of the energies of the primary γ rays E_γ at the respective excitation energies E_i of the nucleus.

Fermi's golden rule predicts that the decay probability may be factorized into a transition matrix element between the initial and final states, and the density of final states. According to the Brink-Axel hypothesis [13, 14], the γ-ray transmission coefficient $\mathscr{T}$ is approximately independent of excitation energy. From this we deduce that the probability for γ decay at a certain excitation energy E_i to a final level E_f, by a γ ray of energy $E_\gamma = E_i - E_f$ is proportional to the product of the level density at the final level $\rho(E_f)$ and the γ transmission coefficient $\mathscr{T}(E_\gamma)$, given that we are in the statistical energy region. The normalized primary γ-ray matrix can therefore be written as

$$P(E_i, E_\gamma) = \frac{\mathscr{T}(E_\gamma)\rho(E_i - E_\gamma)}{\sum_{E_\gamma = E_\gamma^{\min}}^{E_i} \mathscr{T}(E_\gamma)\rho(E_i - E_\gamma)}. \tag{5.9}$$

The functional form of Eq. (5.9) does not give a one-to-one solution, but an infinite number of possibilities. It can be shown that all solutions can be deduced from each other through the following transformation,

$$\tilde{\rho}(E_i - E_f) = \rho(E_i - E_f) A e^{\alpha(E_i - E_\gamma)} \tag{5.10}$$

$$\tilde{\mathscr{T}}(E_\gamma) = \mathscr{T}(E_\gamma) B e^{\alpha E_\gamma}, \tag{5.11}$$

see Appendix C for the details of the derivation. In these formulas the parameters A, B and α can be chosen arbitrary and still give a good agreement with the experimental primary γ-ray matrix. However, in order to obtain the desired functions ρ and $\mathscr{T}$, the extracted functions $\tilde{\rho}$ and $\tilde{\mathscr{T}}$, are normalized to known experimental data. Details of this procedure will be discussed in section 5.2.2.

5.2.1 χ^2 minimization

A least-squareds method is performed in order to determine ρ and $\mathscr{T}$. The functions are therefore chosen such that the function

$$\chi^2 = \frac{1}{N} \sum_{E_i=E_i^{\min}}^{E_i^{\max}} \sum_{E_\gamma=E_\gamma^{\min}}^{E_i^{\max}} \left(\frac{P(E_i,E_\gamma) - P_{\exp}(E_i,E_\gamma)}{\Delta P_{\exp(\mathrm{E_i},\mathrm{E}\gamma)}} \right)^2, \tag{5.12}$$

is minimised. The factor N in the above expression represents the number of degrees of freedom, which is equal to

$$N = N_P - N_\rho - N_{\mathscr{T}} \tag{5.13}$$

where N_P is the number of entries in the primary γ ray matrix, and N_ρ and $N_{\mathscr{T}}$ are the number of data points in the respective spectra [45]. This χ^2 is minimised with respect to $\mathscr{T}$ at every γ energy bin, and with respect to ρ at every excitation energy $E_f = E_i - E_\gamma$,

$$\frac{\partial}{\partial \mathscr{T}(E_\gamma)} \chi^2 = 0 \quad \text{and} \quad \frac{\partial}{\partial \rho(E_i - E_\gamma)} \chi^2 = 0. \tag{5.14}$$

As a starting point we set $\rho^{(0)} = 1$, to be a zeroth order estimate. This can be chosen arbitrary and all other solutions can be found from the transformations of Eq. (5.11). Inserting this solution into Eq. (5.9) we obtain

$$P(E_i,E_\gamma) = \frac{\mathscr{T}(^{(0)}E_\gamma)}{\sum_{E_\gamma=E_\gamma^{\min}}^{E_i} \mathscr{T}^{(0)}(E_\gamma)}. \tag{5.15}$$

Furthermore, we sum over all excitation energy bins, while requiring that the γ energy can not exceed the excitation energy,

$$\sum_{E_i=\max(\mathrm{E_i^{min}},\mathrm{E}\gamma)}^{E_i^{\max}} P(E_i,E_\gamma) = \mathscr{T}^{(0)}(E_\gamma) \sum_{E_i=\max(\mathrm{E_i^{min}},\mathrm{E}\gamma)}^{E_i^{\max}} \frac{1}{\sum_{E_\gamma=E_\gamma^{\min}}^{E_i} \mathscr{T}^{(0)}(E_\gamma)}. \tag{5.16}$$

We choose to set the sum on the right hand side equal unity, and obtain the zeroth order estimate for $\mathscr{T}$,

$$\mathscr{T}^{(0)}(E_\gamma) = \sum_{\max(\mathrm{E_i^{min}},\mathrm{E}\gamma)}^{E_i^{\max}} P(E_i,E_\gamma). \tag{5.17}$$

The next step is to calculate higher order estimates. To do so we have to evaluate Eq. (5.14), in doing so we can derive the following expressions [45],

$$\mathscr{T}(E_\gamma) = \frac{\sum_{\max(E_i^{\min},E_\gamma)}^{E_i^{\max}} \rho(E_i - E_\gamma)\phi(E_i,E_\gamma)}{\sum_{\max(E_i^{\min},E_\gamma)}^{E_i^{\max}} \rho^2(E_i - E_\gamma)\psi(E_i,E_\gamma)} \tag{5.18}$$

$$\rho(E_f) = \frac{\sum_{\max(E_i^{\min},E_f+E_\gamma^{\min})}^{E_i^{\max}} F(E_i - E_f)\phi(E_i,E_i - E_f}{\sum_{\max(E_i^{\min},E_f+E_\gamma^{\min})}^{E_i^{\max}} F^2(E_i - E_f)\psi(E_i,E_i - E_f)}, \tag{5.19}$$

where

$$\phi(E_i,E_\gamma) = \frac{a(E_i)}{s^3(E_i)} - \frac{b(E_i)}{s^2(E_i)} + \frac{P(E_i,E_\gamma)}{s(E_i)(\Delta P(E_i,E_\gamma))^2} \tag{5.20}$$

$$\psi(E_i,E_\gamma) = \frac{1}{(s(E_i)\Delta P(E_i,E_\gamma))^2}, \tag{5.21}$$

and

$$a(E_i) = \sum_{E_\gamma=E_\gamma^{\min}} \left(\frac{\mathscr{T}(E_\gamma)\rho(E_i - E_\gamma)}{\Delta P(E_i,E_\gamma)}\right)^2 \tag{5.22}$$

$$b(E_i) = \sum_{E_\gamma=E_\gamma^{\min}} \frac{\mathscr{T}(E_\gamma)\rho(E_i - E_\gamma)P(E_i,E_\gamma)}{(\Delta P(E_i,E_\gamma))^2} \tag{5.23}$$

$$s(E_i) = \sum_{E_\gamma=E_\gamma^{\min}} \mathscr{T}(E_\gamma)\rho(E_i - E_\gamma). \tag{5.24}$$

We start each new iteration by calculating a, b and s, from Eqs. (5.22)-(5.24). The result is inserted into Eqs. (5.20) and (5.21) to obtain ϕ and ψ. Finally, we can calculate the new ρ and $\mathscr{T}$, using Eqs. (5.18) and (5.19). In Fig. 5.2 an illustration of how the summations used in the above equations are performed. Only the white region of the figures are used when extracting ρ and $\mathscr{T}$. We exclude the low excitation energy region, due to non-statistical γ decay. The low γ energy region are excluded due to insufficient subtraction of yrast transitions and limitations in the electronics that make the low γ-ray energy region not reliable. We observe from the left panel of Fig. 5.2 that when the γ energy E_γ exceeds the minimum excitation energy $E_{i,\min}$, the summation has to start from $E_i = E_\gamma$.

Convergence is often achieved fast. However, in some cases the χ^2-minimum is very shallow. To ensure that we find the global minimum we set a restriction to the maximum change of every datapoint in ρ and $\mathscr{T}$ within one iteration, to a set

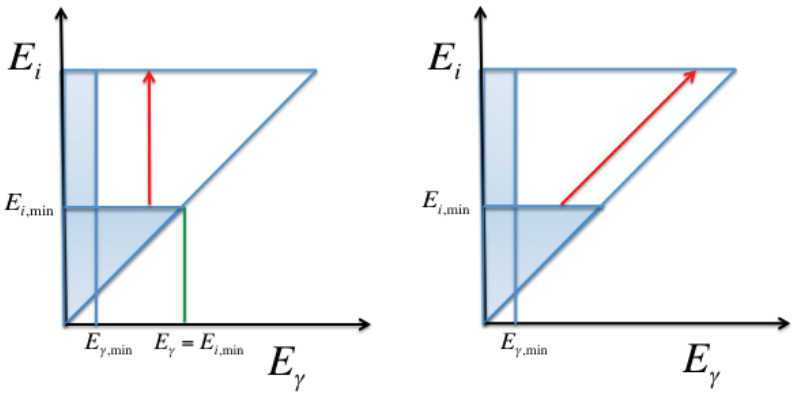

Figure 5.2: *A sketch of how the summation over the excitation energy bins (left), and γ energy bins (right) of the primary γ-ray matrix are performed. The red lines give the directions of the summation. The shaded area is usually excluded due to methodical problems.*

percentage P [45]. In the case the value is higher than the accepted value, it is set to the value equal the maximum allowed change. The chosen allowed change is narrowed as the number of iterations increase, in this way we limit the execution time while retaining an accurate solution [45].

The first generation spectra P for ^{164}Dy at six different excitation energies are displayed in Fig. 5.3 and compared to the ones obtained by multiplying the extracted $\mathscr{T}$ and ρ functions. In general, the agreement between the experimental data and the fit is very good.

5.2.2 Normalization proceedure

The functional form of ρ and $\mathscr{T}$ are uniquely determined by the Oslo method, but in order to normalize on depends upon complimentary experimental data. The transformation generators α, A and B of Eqs. (5.11) and (5.11), represents the slope of the two functions and the absolute normalisation of ρ and $\mathscr{T}$, respectively.

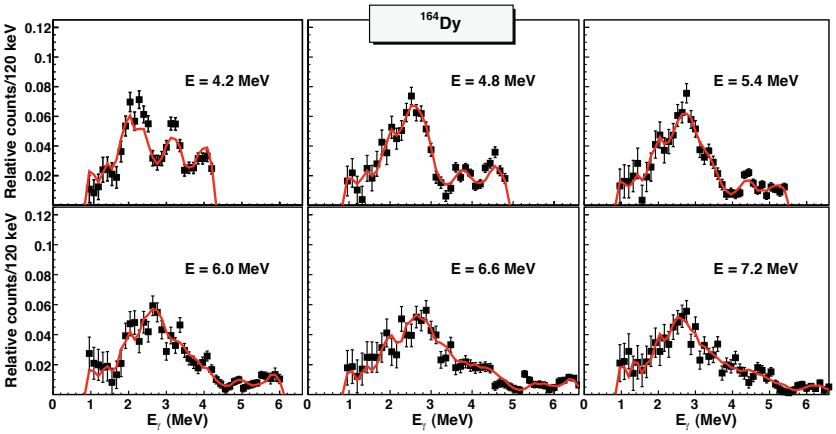

Figure 5.3: *Comparison of experimental first-generation spectra (squares) and the ones obtained from multiplying the extracted $\mathscr{T}$ and ρ functions (red line).*

Normalizing ρ

The parameters α and A can be determined by normalising ρ to known discreet levels at low excitation energy [47], and at high energy from the density of neutron resonances following (n,γ) capture at the neutron separation energy S_n. The level density $\rho(S_n)$ is calculated from s-wave (or p-wave) resonance spacings D_0 taken from RIPL-3 [11]. The total level density at the neutron separation energy assuming s-wave ($l=0$) is [45],

$$\rho(S_n) = \frac{2\sigma^2}{D_0}\frac{1}{(I+1)\exp[-(I+1)^2/2\sigma^2]+\exp[-I^2/2\sigma^2]}, \tag{5.25}$$

where I is the spin of the target nucleus. The spin-cut off parameter σ depends on the model assumed for ρ, see discussion in chapter 2. The experimental data normally extends up to $\sim S_n - 1$ MeV, we therefore extrapolate $\rho(S_n)$ by a Fermi gas level density to fill the gap between the data and the calculated $\rho(S_n)$ [45]. An illustration of the normalisation of ρ is given in the upper panel of Fig. 5.4.

Normalizing $\mathscr{T}$

The parameter B controls the scaling of the transmission coefficient $\mathscr{T}$. It is determined using the average, total radiative width $\langle\Gamma_\gamma\rangle$ at S_n. Assuming that the

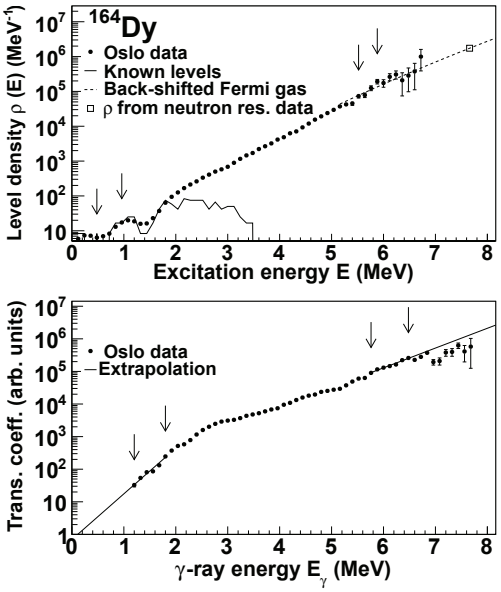

Figure 5.4: *Upper panel: The level density is normalized to known discrete levels and to $\rho(S_n)$ calculated from neutron resonance spacing data extrapolated using the back shifted Fermi gas model. Lower panel: The extrapolation of the radiative transmission coefficient. The normalization is preformed in the regions between the arrows.*

γ decay is dominated by dipole transitions, the width is given by [48]

$$\langle \Gamma_\gamma \rangle = \frac{1}{2\pi\rho(S_n, I, \pi)} \sum_{I_f} \int_0^{S_n} dE_\gamma B\mathscr{T}(E_\gamma)\rho(S_n - E_\gamma, I_f), \qquad (5.26)$$

for initial spin I and parity π. The summation and integration run over all final levels with spin If that are accessible by $E1$ or $M1$ transitions with energy E_γ. In Fig. 5.4, the normalisation of the transmission coefficient of ^{164}Dy is displayed.

Correcting α, A and B using photo-absorption data

From Eq. 5.26 we see that the determination of B depends on the spin-cut off parameter σ. The spin distribution is however, difficult to determine, as discussed

in Ref. [43]. Hence, there are some uncertainties originating from the normalization procedure. Another procedure is therefore adopted, where we compare the RSF with the extrapolation of known data from photo-absorption reactions. This method has been applied to check and correct the normalization of the dysprosium isotopes.

The RSF can be calculated from $\mathscr{T}$ by [11],

$$f(E_\gamma) = \frac{1}{2\pi}\frac{\mathscr{T}(E_\gamma)}{E_\gamma^3}, \tag{5.27}$$

assuming dipole radiation. The RSF is compared with the strength function derived from the cross section σ from photo-absorption experiments by [11],

$$f(E_\gamma) = \frac{1}{3\pi^2\hbar^2c^2}\frac{\sigma(E_\gamma)}{E_\gamma}. \tag{5.28}$$

The photo-absorption data is extrapolated below S_n using the generalized Lorentzian (GLO) as defined in RIPL [11] to describe the GEDR, but with a constant temperature of the final states T_f. In addition we have two $M1$ resonances, the scissors mode and the spin-flip, which are both assumed a Lorentzian shape, as discussed in chapter 2.

The renormalisation of the dysprosium isotopes have been determined by simultaneously varying the parameters α and B and the strength σ_{py}, width Γ_{py} and centroid E_{Py} of the scissors mode, to best mach the two sets of experimental data and to find an appropriate model. In Fig. 5.5 the results of the renormalisation of ^{161}Dy is displayed.

One can then normalize the level density ρ, by applying the same slope α as determined for the strength function, and determine the absolute normalization A by fitting ρ to known discrete levels at low excitation energies.

5.2.3 Uncertainties of ρ and $\mathscr{T}$

Only statistical errors are taken into consideration when calculating the uncertainties of ρ and $\mathscr{T}$, possible errors steeming from the models chosen for normalisation are not considered. Since the experimental primary γ-ray matrix has been obtained from raw data, one first have to estimate the error of the primary γ-ray matrix data, an furthermore estimate the error propagation through the unfolding- and subtraction techniques discussed in the previous chapter. An outline of how these estimations were made can be read in Ref. [45]. An analysis of possible systematic errors in the Oslo method is discussed in detail in Ref. [43].

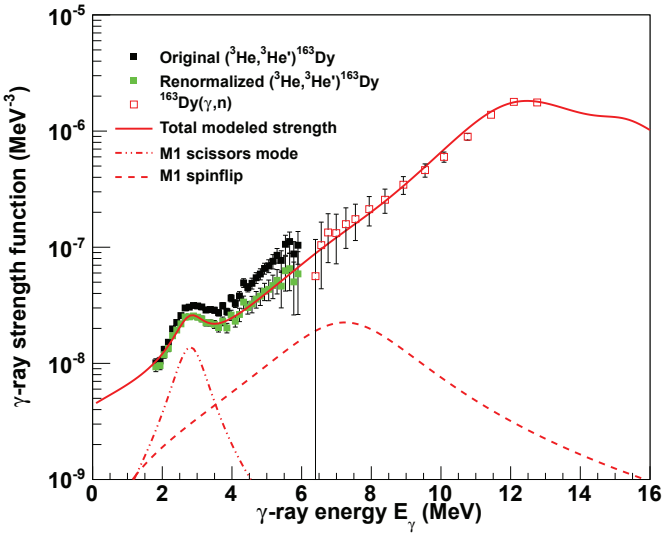

Figure 5.5: *Renormalized RSF of* ^{163}Dy *(green squares), compared with the original data (black squares). Also displayed is the RSF deduced from the* $^{163}(\gamma,n)$ *cross sections (red squares), and the modelled strength (red lines).*

Chapter 6

Articles

The following papers are included in this thesis:

I H.-T. Nyhus, S. Siem, M. Guttormsen, A. C. Larsen, A. Bürger, N. U. H. Syed, G. M. Tveten, and A. Voinov *Radiative strength functions i* ^{163,164}Dy, Phys. Rev. C 81, 024325 (2010)., *Erratum: Radiative strength functions in* ^{163,164}*Dy*, Phys. Rev. C 82, 029909(E) (2010).

II H.-T. Nyhus, S. Siem, M. Guttormsen, A. C. Larsen, A Bürger, N. U. H. Syed, H. K. Toft, G. M. Tveten, and A. Voinov, *Level density and thermodynamic properties of dysprosium isotopes*, Phys. Rev. C 85, 014323 (2012).

III H. Utsunomiya, T. Shima, K. Takahisa, D. M. Filipescu, O. Tesileanu, I. Gheorghe, H.-T. Nyhus, T. Renstrøm, Y.-W. Lui, Y. Kitagawa, S. Amano, S. Miyamoto, *Energy Calibration of the NewSUBARU Storage Ring for Laser Compton-Scattering Gamma Rays and Applications*, accepted to be published in IEEE.

IV H.-T. Nyhus, T. Renstrøm, H. Utsunomiya, S. Goriely, D. M. Filipescu, I. Gheorghe, O. Tesileanu, T. Glodariu, T. Shima, K. Takahisa, Y.-W. Lui, S. Hilaire, S. Péru, M. Martini, and A. J. Koning, *Photoneutron cross sections for neodymium isotopes: toward a unified understanding of* (γ,n) *and* (n,γ) *reactions in the rare earth region I*, to be submitted to Phys. Rev. C.

V D. M. Filipescu, I. Gheorghe, H. Utsunomiya, S. Goriely, T. Renstrøm, H.-T. Nyhus, O. Tesileanu, T. Glodariu, T. Shima, K. Takahisa, Y.-W. Lui, S. Hilaire, S. Péru, and A. J. Koning, *Photoneutron cross sections for samarium isotopes: toward a unified understanding of* (γ,n) *and* (n,γ) *reactions in the rare earth region II*, to be submitted to Phys. Rev. C.

VI H.-T. Nyhus, T. Renstrøm, A. C. Larsen, H. Utsunomiya, S. Goriely D.-M. Filipescu, I. Gheorghe, M. Guttormsen, Y. W. Lui, T. Shima, S. Siem, K. Takahisa and O. Tesileanu, *Photo-absorption cross sections, radiative strength functions and astrophysical reaction rates of dysprosium isotopes*, to be submitted to Phys. Rev C.

VII T. K. Eriksen, H.-T. Nyhus, A. Bürger, M. Guttormsen, A. Görgen, A. C. Larsen, P. Mansouri, T. Renstrøm, S. Rose, I. E. Ruud, S. Siem, H. K. Toft, G. M. Tveten, and J. N. Wilson, *Level densities and γ-ray strength functions of* $^{105-108}$Pd, to be submitted to Phys. Rev C.

6.1 A brief introduction to the papers

Paper I and II

The nuclei ^{163,164}Dy have been investigated using the Oslo method on data from the pickup reaction $(^3\mathrm{He},\alpha\gamma)^{163}$Dy and the inelastic scattering $(^3\mathrm{He},^3\mathrm{He}'\gamma)^{163}$Dy, respectively. The nuclei have been evaluated using the Oslo method.

In paper I the radiative strength function for both nuclei are presented. In particular, a small resonance centred around $E_\gamma \approx 3$ MeV, is evaluated. The parameters of this so-called pygmy $M1$ resonance (the scissors mode) are compared with previous results on ^{160,161,162}Dy using the Oslo method, and with data on ^{163}Dy measured by the Prague group using the two-step cascade method. The integrated reduced transition probability $B(M1\uparrow)$ of the pygmy resonance is compared with neighbouring dysprosium isotopes, and all agree within the uncertainties.

Paper III is dedicated to study the level densities and thermodynamic properties. Thermodynamics are deduced within both micro-canonical and canonical ensemble theories. A phase transition from the pair-correlated state at low energies to a less correlated or uncorrelated state is studied in both ensembles. We observe transitions between the various quasiparticle regimes when studying thermodynamical properties within the framework of the micro-canonical ensemble. In the canonical ensemble we observe a second-order phase transition, influenced by the first broken pairs of the nucleus, but also the later breaking of Cooper pairs enhances the phase transition significantly. It is investigated whether the temperature of the nucleus is constant or a varying function of excitation energy. It is found that above an excitation energy of 3 MeV the temperature of all five dysprosium nuclei have a constant value within the experimental uncertainties. The impact of a constant-temperature level density versus a Fermi gas level density is discussed with respect to the canonical heat capacity.

Paper III

The electron beam at the NewSUBARU facility has been calibrated in the nominal energy range $550-974$ MeV. The electron beam was calibrated by using γ-ray beams produced in inverse Compton scattering between CO_2 laser photons and relativistic electrons. The resulting laser Compton-scattered (LCS) γ-ray beams were in the energy range from 561 keV to 1728 keV, and detected with a high purity germanium detector. The electron beam energies were determined by reproducing the full energy peaks of the γ-ray beams by Monte Carlo simulations. The reproducibility of the electron beam energy is excellent in an independent injection and deceleration. The present energy calibration of the electron beams

offers a standard for the energy calibration of high-energy LCS γ-ray beams produced with a Nd:YVO4 laser.

Paper IV and V

Photo-neutron cross sections of five neodymium (paper IV) and seven samarium (paper V) isotopes have been studied. The experiments were performed at the NewSUBARU synchrotron laboratory, using laser Compton backscattered γ-ray beams. The photo-neutron cross sections where extracted from the neutron separation threshold of each isotope up to $\approx$ 13 MeV. The radiative neutron capture cross section where extracted using an indirect method called the γ-ray strength function method. The measurements were performed as a step to obtain a unified understanding of (γ, n) and (n, γ) reactions in the rare earth region.

The present systematic measurement included two odd-N nuclei, ^{143}Nd and ^{145}Nd for which photo-neutron cross sections are presented near neutron threshold for the first time. Photo-neutron cross sections for two odd-N nuclei, ^{147}Sm and ^{149}Sm, are also measured for the first time

The neodymium and samarium isotopes are of special interest with regards to nuclear astrophysics. The s-process path along the line of β stability has been studied for the neodymium and samarium isotopes. The short-lived ^{147}Nd isotope is an s-process branch point nucleus, where β-decay and neutron capture are computing processes. Furthermore, radiative neutron capture cross sections for ^{147}Nd affects the isotopic ratio of the two s-only nuclei, ^{148}Sm and ^{150}Sm. The present photo-neutron measurement also involved a p-process nucleus ^{144}Sm, s-only nuclei ^{148}Sm and ^{150}Sm and an r-only nucleus ^{154}Sm.

Paper VI

The photo-absorption cross section of ^{162,163}Dy have been extracted from (γ, n) experiments, and the radiative strength functions are deduced. The experiments where performed at the NewSUBARU synchrotron laboratory, using laser Compton backscattered γ-ray beams, which are nearly monochromatic. The data are extracted from the neutron separation threshold up to around $\approx$ 13 MeV, covering an energy region where there are no preexisting data for dysprosium isotopes. The new data are compared with Dy data evaluated by the Oslo method, and a renormalisation is made. Furthermore, the $M1$ scissor mode is discussed, and it is evaluated how it will influence astro-physical reaction rates.

Paper VII

The nuclear level densities and radiative strength functions of $^{105-108}$Pd have been investigated using the Oslo method. Particle-γ coincidence measurements were performed at the Oslo cyclotron laboratory. Using a ^{3}He beam, both the pickup reaction (^{3}He, $\alpha\gamma$) and the inelastic scattering (^{3}He,^{3}He$'\gamma$) channel was studied. The level densities exhibits well known characteristics. The extracted radiative strength functions indicate a sudden increase in magnitude for $E_\gamma > 4$ MeV, which is believed to be caused by a pygmy resonance centered at $E_\gamma \approx 8.5$ MeV. The enhancement is likely cased by resonances related to neutron skin oscillations. We also observe an interesting feature in the radiative strength function at low γ-ray energy, where we have a nearly constant strength over a long energy region. We also see slightly indications of increasing strength at very low γ-ray energy, known as the upbend. This indicates that the Pd isotopes is in a transitional region considering the upend behaviour.

6.2 Paper I: Radiative strength functions in ^{163,164}Dy

PHYSICAL REVIEW C **81**, 024325 (2010)

Radiative strength functions in ^{163,164}Dy

H. T. Nyhus,[1,*] S. Siem,[1] M. Guttormsen,[1] A. C. Larsen,[1] A. Bürger,[1] N. U. H. Syed,[1] G. M. Tveten,[1] and A. Voinov[2]
[1]*Department of Physics, University of Oslo, N-0316 Oslo, Norway*
[2]*Department of Physics and Astronomy, Ohio University, Athens, Ohio 45701, USA*
(Received 3 September 2009; published 25 February 2010)

The nuclei ^{163,164}Dy have been investigated using the Oslo method on data from the pickup reaction ^{164}Dy(^{3}He,$\alpha\gamma$)^{163}Dy and the inelastic scattering ^{164}Dy(^{3}He,^{3}He$'\gamma$)^{164}Dy, respectively. The radiative strength functions for both nuclei have been extracted, and a small resonance centered around $E_\gamma \approx 3$ MeV is observed in both cases. The parameters of this so-called pygmy $M1$ resonance (the scissors mode) are compared with previous results on ^{160,161,162}Dy using the Oslo method, and with data on ^{163}Dy measured by the Prague group using the two-step cascade method. In particular, the integrated reduced transition probability $B(M1\uparrow)$ of the pygmy resonance is compared with neighboring dysprosium isotopes. We also observe an enhanced strength in the region above $E_\gamma \approx 5$ MeV in ^{164}Dy. Possible origins of this feature are discussed.

DOI: 10.1103/PhysRevC.81.024325 PACS number(s): 25.20.Lj, 24.30.Gd, 25.55.Hp, 27.70.+q

I. INTRODUCTION

A continuing effort has long been devoted to studying γ decay from excited nuclei. The radiative strength function (RSF) represents the mean value of the decay probability via a γ ray with energy E_γ, and contains rich information on the average electromagnetic properties of the nucleus.

For high-energy γ transitions (∼7–20 MeV), the RSF is dominated by the giant electric dipole resonance (GEDR). At lower energies other resonances have been discovered, such as the giant magnetic dipole resonance (GMDR, also called the giant magnetic spin-flip resonance) and the electric quadrupole resonance; however, these have a significantly lower strength [1]. In addition, there are other structures observed in the RSF governed by various collective modes of the nucleus. These structures are often referred to as pygmy resonances because of their low strength compared to the GEDR. There are two known pygmy resonances: the $E1$ resonance for γ ray energies between 5 and 10 MeV, which is believed to stem from neutron skin oscillation [2], and the $M1$ resonance called the scissors mode, which is observed in the region of $E_\gamma = 3$ MeV for rare-earth nuclei [3].

The RSFs below the neutron threshold have been studied mainly by (γ,γ') experiments, also called nuclear resonance fluorescence (NRF) [4]. Other methods, such as the two-step-cascade (TSC) method [5] and the Oslo method [6], have also successfully provided data on the RSFs for many nuclei. The latter method enables us to extract the RSF for γ ray energies up to the neutron binding energy B_n. This method has been used in the present analysis.

Previous experiments have been performed on ^{160,161,162}Dy [7] using the Oslo method [6]. From these data, the widths of the $M1$ pygmy resonance have been found to be about two times greater than the width found for ^{163}Dy obtained by the Prague group using the TSC method [8]. In the present work, we have studied ^{163,164}Dy to investigate the discrepancy between the measured widths. In particular, we have compared the total integrated strength $B(M1\uparrow)$ of all the mentioned Dy isotopes.

Details about the experimental method are presented in Sec. II, followed by the experimental results for the RSF in Sec. III. Finally, conclusions are drawn in Sec. IV.

II. EXPERIMENTAL PROCEDURE AND DATA ANALYSIS

The experiment was conducted at the Oslo Cyclotron Laboratory (OCL), using a 38-MeV beam of ^{3}He particles. The target of 98.5% enriched ^{164}Dy had a thickness of 1.73 mg/cm^2, and the reactions ^{164}Dy(^{3}He,$\alpha\gamma$)^{163}Dy and ^{164}Dy(^{3}He,^{3} He$'\gamma$)^{164}Dy were studied.

The γ rays and ejectiles were measured with the CACTUS multidetector array [9], which consists of a sphere of 28 collimated NaI γ detectors with total efficiency of 15% of 4π, surrounding a vacuum chamber containing eight $\Delta E - E$ Si particle telescopes with thicknesses of 140 and 1500 μm. The particle telescopes were placed in the forward direction at 45° relative to the beam axis.

From the known Q values, the excitation energies of the nuclei were calculated from the detected ejectile energy using reaction kinematics. The particles and γ rays were measured in coincidence; hence, each γ ray could be assigned to an initial excitation energy of the nucleus. The γ ray spectra were unfolded using the known response functions of the CACTUS detector array [10]. The excited nuclei decayed through a cascade of γ rays down to the ground state. By using the first-generation method [11], we were able to isolate the first (primary) γ rays emitted in each γ decay cascade. The distribution of primary γ rays was found for each excitation energy bin, giving an excitation energy vs γ ray energy matrix denoted by $P(E_i, E_\gamma)$. The primary γ ray spectrum was normalized to unity for each excitation energy bin, which then represents the decay probability for each γ ray with energy E_γ decaying from a certain excitation energy E_i: $\sum_{E_\gamma=E_\gamma^{\min}}^{E_i} P(E_i, E_\gamma) = 1$. The primary γ ray matrix for ^{164}Dy is shown in Fig. 1. The diagonal line of the matrix corresponds to decay directly to the ground state ($E_\gamma = E_i$);

*h.t.nyhus@fys.uio.no

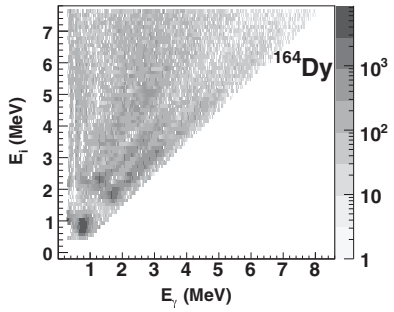

FIG. 1. Primary γ-ray matrix for ^{164}Dy, displaying primary γ rays emitted at each initial excitation energy.

however, it is more probable to decay to the first excited 2^+ and 4^+ states. Therefore, a ridge is formed in the matrix for decay to $E_i \sim 150$ keV, see Fig. 1.

The original Brink-Axel hypothesis [12,13] states that the GEDR can be built on every excited state, and that the properties of the GEDR do not depend on the temperature of the nuclear state on which it is built. This hypothesis can be generalized to include any type of collective excitation. Provided that this hypothesis is valid, the primary γ ray matrix can be factorized as

$$P(E_i, E_\gamma) \propto \mathcal{T}(E_\gamma)\rho(E_i - E_\gamma), \tag{1}$$

where $P(E_i, E_\gamma)$ is the experimentally obtained and normalized primary γ ray matrix. The function $\mathcal{T}(E_\gamma)$ represents the radiative transmission coefficient, and $\rho(E_i - E_\gamma)$ is the level density at the final energy $E_f = E_i - E_\gamma$. The above factorization is based on the essential assumption that the system is fully thermalized prior to γ emission, so the reaction can be described as a two-stage process of which the first is the formation of the compound nucleus, which subsequently decays in a manner that is independent of the mode of formation [14]. The formation of a complete compound state is as fast as $\sim 10^{-18}$ s, significantly less than the typical lifetime of a state in the quasicontinuum, which is $\sim 10^{-15}$ s. Therefore, the assumption is believed to be reasonable, and the decay process is at least mainly statistical. Recently, it has been shown that Eq. (1) can be valid even in some cases where full thermalization is not achieved [15].

However, there is experimental evidence that the Brink-Axel hypothesis is violated for high temperatures (above 1–2 MeV). In particular, the width of the GEDR has been shown to depend on the temperatures of the final states [16]. For our experimental conditions, the excitation energy (and thus the temperature) is relatively low and changes slowly with excitation energy ($T \sim \sqrt{E_f}$). Therefore, we assume that the radiative strength function does not depend on temperature in the energy region under consideration.

The right-hand side of Eq. (1) is normalized to unity, yielding

$$P(E_i, E_\gamma) = \frac{\mathcal{T}(E_\gamma)\rho(E_i - E_\gamma)}{\sum_{E'_\gamma = E_\gamma^{\min}} \mathcal{T}(E'_\gamma)\rho(E_i - E'_\gamma)}. \tag{2}$$

Using this equation and applying a least-squares fit to the primary γ ray matrix, a unique functional form of $\rho(E_i - E_\gamma)$ and $\mathcal{T}(E_\gamma)$ is derived [6], while the normalization is yet to be determined. There are infinitely many normalization options that reproduce the experimental primary γ ray matrix. All the solutions are related to each other through the two transformations [6]

$$\widetilde{\rho}(E_i - E_\gamma) = A\ \exp[\alpha(E_i - E_\gamma)]\ \rho(E_i - E_\gamma) \tag{3}$$

and

$$\widetilde{\mathcal{T}}(E_\gamma) = B\ \exp(\alpha\ E_\gamma)\ \mathcal{T}(E_\gamma), \tag{4}$$

where A, B, and α are constants representing the absolute values of $\rho(E_i - E_\gamma)$ and $\mathcal{T}(E_\gamma)$, and the slopes of the two functions, respectively. These parameters are determined by normalizing Eqs. (3) and (4) to known experimental data. The parameters A and α are identified by normalizing the experimental level density to known levels found from discrete spectroscopy at low energies. At higher excitation energies, the experimental level density is normalized to the level density determined from the known neutron resonance spacing data [1] at the neutron binding energy B_n. The present experimental data extend up to about B_n–1 MeV; an interpolation is thus required to reach B_n. The back-shifted Fermi gas model [17,18] was applied for this purpose:

$$\rho_{\rm bs}(E) = \eta \frac{\exp(2\sqrt{aU})}{12\sqrt{2}a^{1/4}U^{5/4}\sigma}, \tag{5}$$

where the constant η is applied to adjust $\rho_{\rm bs}(E)$ to the semiexperimental level density at B_n. The intrinsic excitation energy is given by $U = E - C_1 - E_{\rm pair}$, where C_1 is the back-shift parameter equal to $C_1 = -6.6A^{-0.32}$ MeV, where A represents the mass number. The pairing energy $E_{\rm pair}$ is based on the pairing gap parameters Δ_p and Δ_n evaluated from odd-even mass differences [19] according to Ref. [20]. The parameter $a = 0.21A^{0.87}$ MeV^{-1} corresponds to the level density parameter. The spin-cutoff parameter σ is given by $\sigma^2 = 0.0888aTA^{2/3}$, where the nuclear temperature is described by

$$T = \sqrt{U/a}. \tag{6}$$

The normalization of $\rho(E_i - E_\gamma)$ for ^{164}Dy is displayed in the upper panel of Fig. 2.

Finally, $\mathcal{T}(E_\gamma)$ is normalized by determining the coefficient B, which gives the magnitude of $\mathcal{T}(E_\gamma)$. We have the following relation between the total radiative width of neutron resonances $\langle\Gamma_\gamma\rangle$ at the neutron binding energy and the radiative transmission coefficient $\mathcal{T}(E_\gamma)$ [21]:

$$\langle\Gamma_\gamma\rangle = \frac{1}{4\pi\rho\left(B_n, J_i^\pi\right)} \sum_{J_f^\pi} \int_0^{B_n} dE_\gamma B\mathcal{T}(E_\gamma)\rho\left(B_n - E_\gamma, J_f^\pi\right), \tag{7}$$

where $D_i = 1/\rho(B_n, J_f^\pi)$ is the average spacing of s-wave neutron resonances. The summation and integration extends over all final levels with spin J_f which are accessible by γ radiation with energy E_γ.

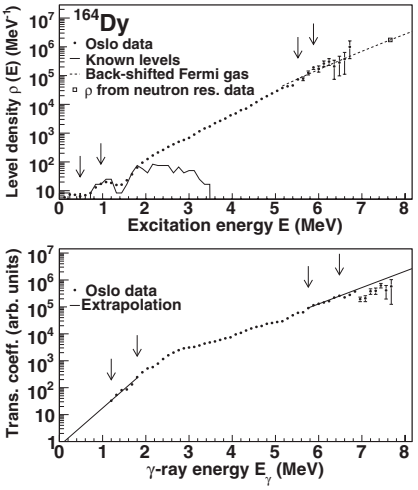

FIG. 2. Upper panel: Level density of ^{164}Dy, normalized to known discrete levels and to $\rho(B_n)$ calculated from neutron resonance spacing data, with an interpolation using the back-shifted Fermi gas model. Lower panel: Radiative transmission coefficient of ^{164}Dy with extrapolations. The normalization is performed in the regions between the arrows.

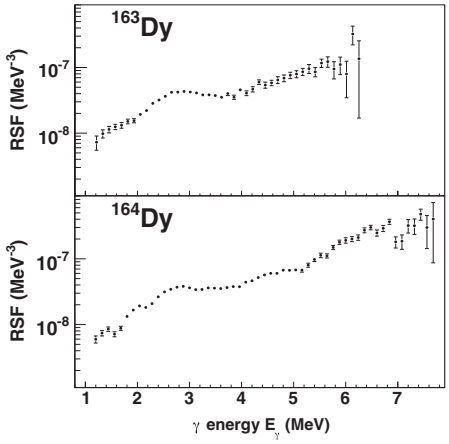

FIG. 3. Normalized RSFs of ^{163,164}Dy.

Due to methodological difficulties, $\mathcal{T}(E_\gamma)$ cannot be determined experimentally for low-energy γ rays, $E_\gamma < 1$ MeV [22]. In addition, the data suffer from poor statistics for γ ray energies $E_\gamma > B_n$–1 MeV. We therefore extrapolate $\mathcal{T}(E_\gamma)$ with an exponential function, as demonstrated for ^{164}Dy in the lower panel of Fig. 2. For further details of the normalization procedure, see Ref. [22]. The parameters used for normalizing $\rho(E_i - E_\gamma)$ and $\mathcal{T}(E_\gamma)$ are given in Table I.

Note that the uncertainties displayed in Fig. 2 only reflect statistical uncertainties and do not include the uncertainties related to the model used for normalization. This is also the case for the other figures showing experimental data.

III. RADIATIVE STRENGTH FUNCTIONS

Assuming that γ decay taking place in the quasicontinuum is dominated by dipole transitions ($L = 1$), the radiative strength function can be calculated from the normalized transmission coefficient by

$$f(E_\gamma) = \frac{1}{2\pi}\frac{\mathcal{T}(E_\gamma)}{E_\gamma^3}. \tag{8}$$

Using this relation, we obtain the experimental RSFs displayed in Fig. 3. We observe that they are increasing functions of γ energy, and we can easily identify the $M1$ pygmy resonance in both cases. We expect the RFS to be composed of the pygmy resonance, the giant electric dipole resonance (GEDR), and the giant magnetic dipole resonance (GMDR). The Kadmenskiĭ-Markushev-Furman (KMF) model [23] is employed to characterize the $E1$ strength. In this model, an excitation-energy dependence is introduced through the temperature of the final states T_f, i.e.,

$$f_{E1}^{\mathrm{KMF}}(E_\gamma) = \frac{1}{3\pi^2\hbar^2c^2}\frac{0.7\sigma_{E1}E_\gamma\Gamma_{E1}^2\left(E_\gamma^2+4\pi^2T_f^2\right)}{E_{E1}\left(E_\gamma^2-E_{E1}^2\right)^2}, \tag{9}$$

where σ_{E1}, Γ_{E1}, and E_{E1} denote the peak cross section, width, and the centroid of the GEDR, respectively. In general, the KMF model describes experimental data very well; however, the temperature dependence violates the Brink-Axel hypothesis. In line with the previously mentioned argument that the temperature varies relatively little in our region of interest, we have assumed that the temperature can be considered to be constant. Thus, the Brink-Axel hypothesis is revived.

It was found that a constant temperature of $T_f = 0.3$ MeV gives a good fit to the experimental data, in agreement with Ref. [7]. For deformed nuclei, the GEDR is split into two and is therefore described as the sum of two strength functions given by Eq. (9). The GMDR is thought to be governed by the spin-flip $M1$ resonance [22] and can be described by a

TABLE I. Parameters used for normalizing ρ and $\mathcal{T}$.

Nucleus	E_{pair} (MeV)	C_1 (MeV)	a (MeV^{-1})	D (eV)	$\sigma\,(B_n)$ (MeV)	B_n (MeV)	$\rho\,(B_n)$ (10^6 MeV^{-1})	J_t	$\langle\Gamma_\gamma\rangle$ (meV)	η
^{163}Dy	0	−1.293	17.653	62(5)	5.435	6.271	0.96(12)	0	112	0.52
^{164}Dy	0.832	−1.291	17.747	6.8(6)	5.541	7.658	1.74(21)	$\frac{5}{2}$	113	0.56

TABLE II. Parameters used for the radiative strength functions.

Nucleus	E^1_{E1} (MeV)	σ^1_{E1} (mb)	Γ^1_{E1} (MeV)	E^2_{E1} (MeV)	σ^2_{E1} (mb)	Γ^2_{E1} (MeV)	E_{M1} (MeV)	σ_{M1} (mb)	Γ_{M1} (MeV)	β_2
^{163}Dy	12.37	278.50	3.17	15.90	139.04	5.12	7.51	1.49	4.00	0.300
^{164}Dy	12.26	280.41	3.12	15.95	140.00	5.15	7.49	1.49	4.00	0.314

Lorentzian function:

$$f_{M1}(E_\gamma) = \frac{1}{3\pi^2\hbar^2c^2}\frac{\sigma_{M1}E_\gamma\Gamma^2_{M1}}{\left(E^2_\gamma - E^2_{M1}\right)^2 + E^2_\gamma\Gamma^2_{M1}}, \quad (10)$$

where σ_{M1}, Γ_{M1}, and E_{M1} give the peak cross section, width, and the centroid of the GMDR, respectively. The GEDR and GMDR parameters are taken from the systematics of Ref. [1] calculated with the deformation parameter β_2 [1]. The $M1$ pygmy resonance $f_{\rm py}$ is described by a Lorentzian function similar to the one given in Eq. (10). All parameters are listed in Table II.

The theoretical strength function is then given by

$$f = \kappa(f_{E1} + f_{M1}) + f_{\rm py}, \quad (11)$$

where f_{E1}, f_{M1}, and $f_{\rm py}$ represent the contributions from the GEDR, GMDR, and the $M1$ pygmy resonance, respectively. The parameter κ is a normalization constant. Together with the pygmy-resonance parameters $\sigma_{\rm py}$, $\Gamma_{\rm py}$, and $E_{\rm py}$, κ is used as a free parameter when performing a least-squares fit to adjust the total theoretical strength to the experimental data.

The fit to the experimental data points is shown in Fig. 4 for both nuclei. The upper panels show the contributions κf_{E1} and κf_{M1} and the sum of these two contributions. In the lower panels the sum $\kappa(f_{E1} + f_{M1})$ is subtracted from the experimental data, and the fit to the $M1$ pygmy resonance is displayed. We notice that the fit to the experimental data around the $M1$ pygmy resonance is good, especially for ^{163}Dy. When comparing the pygmy-resonance parameters of ^{163,164}Dy (see Table III) to those extracted for ^{160,161,162}Dy reported in Ref. [7], we find a smaller width of the pygmy resonance. The previous measurements for ^{160,161,162}Dy yielded widths in the range of $\Gamma_{\rm py} = 1.26$–1.57 MeV using a constant temperature of $T_f = 0.3$ MeV. In the present work, with the same constant temperature, we find widths of $\Gamma_{\rm py} = 0.86$ and 0.80 MeV for ^{163}Dy and ^{164}Dy, respectively. The nucleus ^{163}Dy has been investigated earlier by the Prague group, analyzing TSC spectra from the ^{162}Dy$(n, 2\gamma)^{163}$Dy reaction [8]. In their work, the width of the pygmy resonance was reported to be $\Gamma_{\rm py} = 0.6$ MeV. For this specific case (^{163}Dy), the measured $\Gamma_{\rm py}$ from the Oslo data and the data from the Prague group are comparable within the uncertainties.

We note from Fig. 4 that σ_{M1} for ^{163}Dy is significantly larger than for ^{164}Dy. The reason for this is not yet understood. To obtain a more precise comparison, the total integrated strength $B(M1\uparrow)$ given by

$$B(M1\uparrow) = \frac{9\hbar c}{32\pi^2}\left(\frac{\sigma\Gamma}{E}\right)_{M1\,\rm py}, \quad (12)$$

is calculated for $^{160-164}$Dy, and the results are displayed in Fig. 5. When calculating the weighted average of the Oslo

TABLE III. Fitted pygmy-resonance parameters and normalization constants.

Nucleus	$E_{\rm py}$ (MeV)	$\sigma_{\rm py}$ (mb)	$\Gamma_{\rm py}$ (MeV)	κ
^{163}Dy	2.81(9)	0.72(12)	0.86(19)	1.78(14)
^{164}Dy	2.81(6)	0.53(6)	0.80(12)	1.72(6)

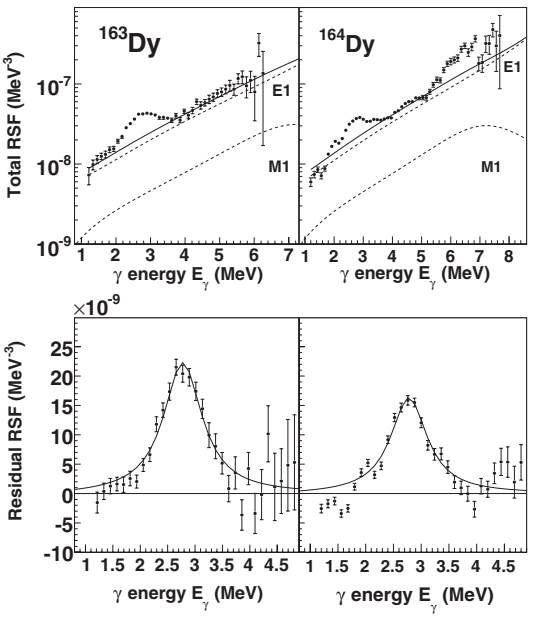

FIG. 4. Experimental RSFs of ^{163}Dy (left panels) and ^{164}Dy (right panels). The dashed lines in the uppermost panels show the contributions from the giant dipole resonances multiplied by κ; the solid line represents the sum of these two contributions, $\kappa(f_{E1} + f_{M1})$. The fit to the experimental data points in ^{164}Dy is performed up to $E_\gamma = 5.3$ MeV. In the lower panels, the sum $\kappa(f_{E1} + f_{M1})$ is subtracted from the experimental data, and the fit to the $M1$ pygmy resonance is displayed (solid line).

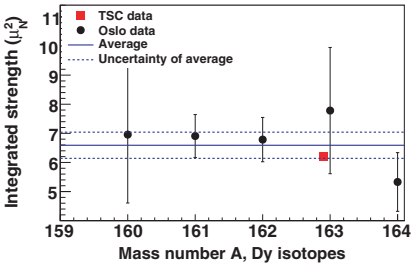

FIG. 5. (Color online) Integrated $B(M1\uparrow)$ strength of the pygmy resonance for Dy isotopes measured with the Oslo method (filled circles) and their average value (solid line). The TSC data point for ^{163}Dy [8] is also displayed (filled square).

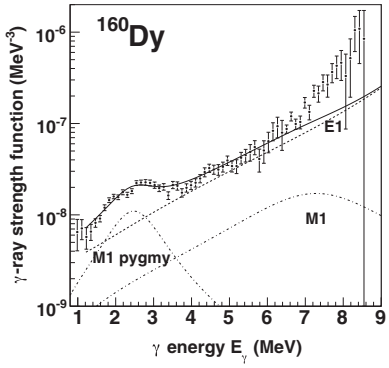

FIG. 6. Experimental RSF for ^{160}Dy. The dashed line represents the tail of the GEDR, while the dashed-dotted lines give the contributions from the GMDR and the $M1$ pygmy resonance. The solid line is the sum of all the resonances. The fit to the experimental data points is performed up to $E_\gamma = 6.9$ MeV.

data, a value of $6.6(4)\mu_N^2$ is found.[1] The $B(M1\uparrow)$ value from the TSC experiment is not included in the fit, because no errors are given in Ref. [8]. We observe that all the measured values agree within the uncertainties.

For ^{164}Dy, we observe an increase in the RSF compared to theory for energies above $E_\gamma \approx 5.0$ MeV. Similar features have been observed in (γ, γ') experiments on other nuclei, e.g., ^{116,124}Sn [24] and ^{208}Pb [25]. For these nuclei, the structure is thought to be governed by the so-called neutron skin oscillation, a collective mode of $E1$ character that for stable nuclei is located in the region of $E_\gamma = 5$–10 MeV. This feature has been observed in nuclei with a high neutron-to-proton ratio N/Z and is interpreted as an oscillation of the neutron-enriched periphery of the nucleus versus a core consisting of equally many protons and neutrons, $N = Z$ [2,26]. Enhanced strength is also observed in the RSF of ^{117}Sn measured at OCL [27]. Unfortunately, the present experimental technique cannot provide information on the electromagnetic character of the enhanced strength in ^{164}Dy. However, it might be a reasonable guess that the observed strength stems from the $E1$ skin oscillation, since we note that Dy nuclei have a high neutron-to-proton ratio of $N/Z = 1.36$–1.48 for the stable isotopes. Evidence of both the $M1$ pygmy resonance and the $E1$ pygmy resonance in one and the same nucleus has, however, not been reported earlier.

Data on ^{160}Dy from a previous experiment [7] also appear to have excess strength, see Fig. 6. Unfortunately, the strength function in the interesting region ($E_\gamma > 7$ MeV) suffers from poor statistics. However, this could be a hint that the same feature is present in this nucleus.

[1]The $B(M1\uparrow)$ values for ^{160,161,162}Dy are calculated from Ref. [6]. The values of ^{161,162}Dy are the weighted averages of the values obtained from the (^{3}He,α) and (^{3}He,^{3}He$'$) reactions.

IV. SUMMARY AND CONCLUSIONS

The nuclei ^{163,164}Dy have been investigated using the Oslo method. The radiative strength functions have been extracted, displaying the $M1$ pygmy resonance. This resonance has been studied in detail, and it is found that the measured widths are smaller than what has previously been measured in other Dy nuclei at OCL. However, the pygmy widths of ^{163,164}Dy in the present work are still larger than what has been measured for ^{163}Dy by means of the TSC method. When comparing the total integrated strength $B(M1\uparrow)$ of the $M1$ pygmy resonance, the results for all the nuclei agree within the uncertainties.

For ^{164}Dy, we have observed an excess of strength for $E_\gamma > 5$ MeV compared to model calculations; similar features can also be seen in ^{160}Dy. The enhanced strength might be due to neutron skin oscillations. If that is the case, this is the first time both the scissors mode and the neutron-skin oscillation mode is seen in one and the same nucleus.

ACKNOWLEDGMENTS

The authors thank E. A. Olsen and J. Wikne for excellent experimental conditions. Financial support from the Research Council of Norway (NFR) is gratefully acknowledged.

[1] T. Belgya *et al.*, *Handbook for Calculations of Nuclear Reaction Data*, RIPL-2. IAEA-TECDOC-1506 (IAEA, Vienna, 2006), available online at http://www-nds.ipen.br/RIPL-2/

[2] P. Van Isacker, M. A. Nagarajan, and D. D. Warner, Phys. Rev. C **45**, R13 (1992).

[3] D. Bohle, A. Richter, W. Steffen, A. E. L. Dieperink, N. Lo. Iudice, F. Palumbo, and O. Scholten, Phys. Lett. **B137**, 27 (1984).

[4] N. Pietralla, P. von Brentano, R.-D. Herzberg, U. Kneissl, N. Lo. Iudice, H. Maser, H. H. Pitz, and A. Zilges, Phys. Rev. C **58**, 184 (1998).

[5] J. Honzátko, K. Konečný, I. Tomandl, J. Vacík, F. Bečvář, and P. Cejnar, Nucl. Instrum. Methods A **376**, 434 (1996).
[6] A. Schiller, L. Bergholt, M. Guttormsen, E. Melby, J. Rekstad, and S. Siem, Nucl. Instrum. Methods Phys. Res. A **447**, 498 (2000).
[7] M. Guttormsen, A. Bagheri, R. Chankova, J. Rekstad, S. Siem, A. Schiller, and A. Voinov, Phys. Rev. C **68**, 064306 (2003).
[8] M. Krtička, F. Bečvář, J. Honzátko, I. Tomandl, M. Heil, F. Käppeler, R. Reifarth, F. Voss, and K. Wisshak, Phys. Rev. Lett. **92**, 172501 (2004).
[9] M. Guttormsen, A. Atac, G. Løvhøyden, S. Messelt, T. Ramsøy, J. Rekstad, T. F. Thorsteinsen, T. S. Tveter, and Z. Zelazny, Phys. Scr. **T32**, 54 (1990).
[10] M. Guttormsen, T. S. Tveter, L. Bergholt, F. Ingebretsen, and J. Rekstad, Nucl. Instrum. Methods Phys. Res. A **374**, 371 (1996).
[11] M. Guttormsen, T. Ramsøy, and J. Rekstad, Nucl. Instrum. Methods Phys. Res. A **255**, 518 (1987).
[12] D. M. Brink, Ph.D. thesis, Oxford University, 1955.
[13] P. Axel, Phys. Rev. **126**, 671 (1962).
[14] A. Bohr and B. Mottelson, *Nuclear Structure* (Benjamin, New York, 1969), Vol. I, p. 184.
[15] N. U. H. Syed, M. Guttormsen, F. Ingebretsen, A. C. Larsen, T. Lönnroth, J. Rekstad, A. Schiller, S. Siem, and A. Voinov, Phys. Rev. C **79**, 024316 (2009).
[16] E. Ramakrishnan *et al.*, Phys. Lett. **B383**, 252 (1996).
[17] A. Gilbert and A. G. W. Cameron, Can. J. Phys. **43**, 1446 (1965).
[18] T. von Egidy, H. Schmidt, and A. N. Behkami, Nucl. Phys. **A481**, 189 (1988).
[19] G. Audi and A. H. Wapstra, Nucl. Phys. **A595**, 409 (1995).
[20] A. Bohr and B. Mottelson, *Nuclear Structure* (Benjamin, New York, 1969), Vol. I, p. 169.
[21] J. Kopecky and M. Uhl, Phys. Rev. C **41**, 1941 (1990).
[22] A. Voinov, M. Guttormsen, E. Melby, J. Rekstad, A. Schiller, and S. Siem, Phys. Rev. C **63**, 044313 (2001).
[23] S. G. Kadmenskiĭ, V. P. Markushev, and V. I. Furman, Yad. Fiz. **37**, 277 (1983) [Sov. J. Nucl. Phys. **37**, 165 (1983)].
[24] K. Govaert, F. Bauwens, J. Bryssinck, D. De Frenne, E. Jacobs, W. Mondelaers, L. Govor, and V. Yu. Ponomarev, Phys. Rev. C **57**, 2229 (1998).
[25] N. Ryezayeva, T. Hartmann, Y. Kalmykov, H. Lenske, P. von Neumann-Cosel, V. Yu. Ponomarev, A. Richter, A. Shevchenko, S. Volz, and J. Wambach, Phys. Rev. Lett. **89**, 272502 (2002).
[26] J. Chambers, E. Zaremba, J. P. Adams, and B. Castel, Phys. Rev. C **50**, R2671 (1994).
[27] U. Agvaanluvsan, A. C. Larsen, R. Chankova, M. Guttormsen, G. E. Mitchell, A. Schiller, S. Siem, and A. Voinov, Phys. Rev. Lett. **102**, 162504 (2009).

Erratum: Radiative strength functions in $^{163,164}Dy$

Erratum: Radiative strength functions in ^{163,164}Dy [Phys. Rev. C 81, 024325 (2010)]

H. T. Nyhus, S. Siem, M. Guttormsen, A. C. Larsen, A. Bürger, N. U. H. Syed, G. M. Tveten, and A. Voinov

(Received 11 August 2010; published 30 August 2010)

DOI: 10.1103/PhysRevC.82.029909 PACS number(s): 25.20.Lj, 24.30.Gd, 25.55.Hp, 27.70.+q, 99.10.Cd

The pairing energies E_{pair} and spin-cutoff parameters σ were misquoted in Table I. The correct values are $E_{\text{pair}} = 0.661$ and 1.707 MeV and $\sigma = 5.408$ and 5.492 for ^{163}Dy and ^{164}Dy, respectively. In the calculations of $\rho(B_n)$ in Table I the correct values were used, and the published results are based on these correct values.

6.3 Paper II: Level density and thermodynamic properties of dysprosium isotopes

PHYSICAL REVIEW C **85**, 014323 (2012)

Level density and thermodynamic properties of dysprosium isotopes

H. T. Nyhus,[1,*] S. Siem,[1] M. Guttormsen,[1] A. C. Larsen,[1] A. Bürger,[1] N. U. H. Syed,[1] H. K. Toft,[1] G. M. Tveten,[1] and A. Voinov[2]

[1]*Department of Physics, University of Oslo, N-0316 Oslo, Norway*

[2]*Department of Physics and Astronomy, Ohio University, Athens, Ohio 45701, USA*

(Received 1 March 2011; revised manuscript received 14 September 2011; published 25 January 2012)

^{163,164}Dy nuclei have been measured by use of the Oslo method on data from pick-up (^{3}He, α) and inelastic scattering (^{3}He,^{3}He$'$) reactions, respectively. The level densities for these dysprosium isotopes together with previously measured $^{160–162}$Dy are extracted in the region below the neutron binding energy. Thermodynamic properties are deduced within both micro-canonical and canonical ensemble theories. A phase transition from the pair-correlated state at low energies to a less correlated or uncorrelated state is studied in both ensembles. It is investigated whether the temperature of the nucleus is constant or a varying function of excitation energy. It is found that above an excitation energy of 3 MeV the temperature of all five dysprosium nuclei have a constant value within the experimental uncertainties. The impact of a constant-temperature level density versus a Fermi gas level density is discussed with respect to the canonical heat capacity.

DOI: 10.1103/PhysRevC.85.014323 PACS number(s): 21.10.Ma, 24.30.Gd, 25.55.Hp, 27.70.+q

I. INTRODUCTION

The nuclear level density is defined as the number of quantum energy levels per energy unit, and it may give information on the underlying nuclear structure. In particular, step structures in the level density can be interpreted as fingerprints of the pair-breaking process. At low excitation energy all nucleons are coupled together in time-reversed orbitals, so-called Cooper pairs. As the energy increases the pairs will break up. The first broken pairs of the nucleus cause a large and abrupt change to the system. As the number of broken pairs increase more and more of the levels near the Fermi energy are occupied by unpaired particles. One therefore expects a weakening of the pair correlation, and eventually it will vanish. Within the seniority model, the step structure in the level density is connected to a specific seniority quantum number (see, e.g., Ref. [1] and references therein).

Also, one may shed new light on the process of quenching of the pair correlations using the framework of thermodynamics. The first broken pairs result in a first-order phase transition seen as discontinuities in the micro-canonical heat capacity. The nucleus will also undergo a phase transition when moving from the pair-correlated state to a less correlated state. A signature of such a phase transition would be the S shape of the heat capacity derived in the canonical ensemble. This transition has been observed in dysprosium nuclei and in other nuclei in the same mass region [2,3].

In this paper we will compare new data on ^{163,164}Dy to the previously extracted $^{160–162}$Dy data. One of the goals is to map the behavior of nuclei in this mass region to achieve further knowledge of the systematics of such nuclei. We have investigated in detail how the nuclear temperature depends upon the excitation energy. All the experimental data are extracted using the Oslo method [4]. Details about the experimental method are presented in Sec. II, followed by the experimental results for the level density in Sec. III. In Sec. IV thermal properties of the nuclei are extracted and discussed, within the framework of both the micro-canonical and the canonical ensemble. Finally, conclusions will be drawn in Sec. V.

II. EXPERIMENTAL PROCEDURE AND DATA ANALYSIS

The experiment was performed at the Oslo Cyclotron Laboratory (OCL). A self-supporting target of ^{164}Dy enriched to 98.5%, with a thickness of 1.73 mg/cm^3, was bombarded by a 38-MeV beam of ^{3}He particles. The target was placed in the center of the multidetector array CACTUS [5]. Surrounding the target, eight Si telescopes were placed at a 45° angle, relative to the beam line in the forward direction, to measure the ejectiles. The particle telescopes were composed of a thin front detector (≈140 μm), which the particles traverse depositing some energy, and a thick end detector (≈1500 μm), where the particles are stopped completely. To measure the γ decay 28 collimated NaI(Tl) detectors were used. The γ-ray detectors were mounted on a spherical frame surrounding the particle telescopes. The γ detectors have a total efficiency of 15.2% for $E_\gamma = 1332$ keV.

The reactions of interest were the pick-up reaction ^{164}Dy(^{3}He, α)^{163}Dy and the inelastic scattering ^{164}Dy(^{3}He,^{3}He$'$)^{164}Dy reaction. From the known Q value and the reaction kinematics, the ejectile energy is transformed into initial excitation energy of the residual nuclei. Further, coincidence matrices containing excitation energy versus γ-ray energy could be extracted. The excitation energy bins are chosen to be 120 keV wide, and total γ-ray spectra were obtained for each bin. These γ-ray spectra where unfolded using the measured response function of the CACTUS array [6].

The first (primary) γ rays emitted in each γ-decay cascade reveal essential information about decay properties. The primary γ rays in each decay cascade are extracted. These γ rays are used to construct the so-called first-generation

*h.t.nyhus@fys.uio.no

matrix $P(E_i, E_\gamma)$, which is a two-dimensional matrix giving the excitation energy of the nucleus versus the energy of the primary γ rays. Experimentally, one cannot resolve which γ ray in a cascade is emitted first. However, a subtraction method, described in Ref. [7], has been developed. This method enables us to extract the primary γ rays from the rest of the cascade. An assumption made in this procedure is that the γ-decay pattern is independent of whether the state is populated in a direct reaction or is populated via γ decay from higher lying states following the initial reaction. When the states have equal chance of being populated by the two processes, the assumption is fulfilled because the following γ decay is a property of the states themselves. When the states have different cross sections to be populated by the two processes, the assumption may not hold. However, in the region of high level density it is likely that the γ distribution is independent of the type of population. The experimental γ-ray matrix is displayed in Fig. 1.

According to Fermi's golden rule the decay probability may be factorized into the transition matrix element between the initial and final state, and the density at the final state ρ_f [8],

$$\lambda_{i\to f} = \frac{2\pi}{\hbar}|\langle f|H|i\rangle|^2\rho_f. \tag{1}$$

By normalizing the primary γ-ray spectrum to unity for each excitation energy bin, the first-generation matrix $P(E_i, E_\gamma)$ will represent the decay probability for $E_i \to E_f = E_i - E_\gamma$,

$$\sum_{E_\gamma=E_\gamma^{\min}}^{E_i} P(E_i, E_\gamma) = 1. \tag{2}$$

We may write the equivalent expression of Eq. (1) as

$$P(E_i, E_\gamma) \propto \mathscr{T}_{i\to f}\rho_f, \tag{3}$$

where $\mathscr{T}_{i\to f}$ is the γ-ray transmission coefficient, and $\rho_f = \rho(E_i - E_\gamma)$ is the level density at excitation energy E_f after the first γ-ray emission. The Brink-Axel hypothesis states that the γ-strength function, and thus also the transmission coefficient, depends only on the energy of the γ transition and not on the excitation energies of the initial (E_i) and final ($E_i - E_\gamma$) states [9,10]. Assuming that this hypothesis is valid, we can write Eq. (3) as

$$P(E_i, E_\gamma) \propto \mathscr{T}(E_\gamma)\rho(E_i - E_\gamma). \tag{4}$$

The above factorization is based on the essential assumption that the system is fully thermalized prior to γ emission, so that the reaction can be described as a two-stage process of which the first is the formation of the compound nucleus, which subsequently decays in a manner that is independent of the mode of formation [11]. This requirement is fulfilled by two factors. First, the spacing between the levels in the quasicontinuum is so small that it is comparable to the residual interaction. The wave functions will therefore overlap and we obtain a significant configuration mixing. Second, the formation of a complete compound state is as fast as $\sim 10^{-18}$ s, significantly less than the typical lifetime of a state in the quasicontinuum, which is $\sim 10^{-15}$ s. Therefore, the assumption is believed to be reasonable, and the decay process is at least mainly statistical.

The ρ and $\mathscr{T}$ functions can be determined by an iterative procedure [4], where each data point in the two functions is adjusted until a global χ^2 minimum with the experimental $P(E_i, E_\gamma)$ matrix is reached. In the fitting procedure a region of low excitation energy is excluded from the P matrix due to nonstatistical decay, as indicated in Fig. 1. The first-generation method has a weakness in that it is difficult to subtract yrast transitions correctly in the P matrix. The levels from which these transitions originate are populated more strongly from higher excited levels through γ emission than through the direct reaction. In addition there are limitations in the electronics that make the low γ-ray energy region ($E_\gamma <$ 400 keV) not reliable. For these reasons a region of low γ-ray energy in the P matrix is excluded.

The first-generation spectra P for ^{164}Dy at six different excitation energies are displayed in Fig. 2 and these are compared to the ones obtained by multiplying the extracted $\mathscr{T}$ and ρ functions. In general, the agreement between the experimental data and the fit is very good.

It has been shown [4] that if one solution of the multiplicative functions ρ and $\mathscr{T}$ is known, one may construct an infinite number of other functions, which give identical fits to the P matrix. All the solutions are related to each other through the two transformations [4]

$$\widetilde{\rho}(E_i - E_\gamma) = A\ \exp[\alpha(E_i - E_\gamma)]\ \rho(E_i - E_\gamma) \tag{5}$$

and

$$\widetilde{\mathscr{T}}(E_\gamma) = B\ \exp(\alpha\, E_\gamma)\ \mathscr{T}(E_\gamma), \tag{6}$$

where A, B, and α are constants representing the absolute value of $\mathscr{T}$ and ρ and the slope of the two functions, respectively. From the γ-ray transmission coefficient $\mathscr{T}$, the γ-ray strength function can be extracted, as has been reported in Ref. [12] for ^{163,164}Dy. In this paper we will focus on the level density.

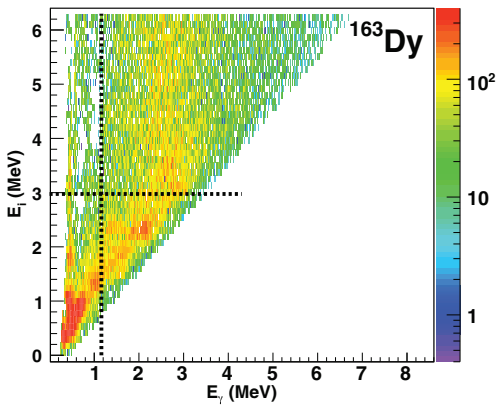

FIG. 1. (Color online) The experimental first-generation matrix of ^{163}Dy. The dashed lines show the limits set in the experimental first-generation matrix.

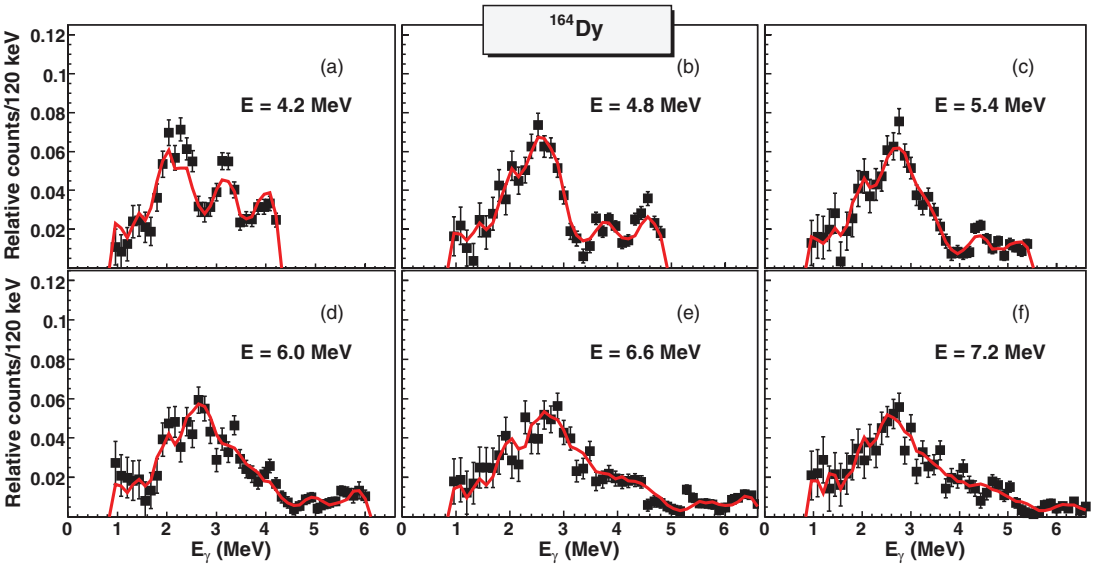

FIG. 2. (Color online) Comparison of experimental first-generation spectra (squares) and the ones obtained from multiplying the extracted $\mathcal{T}$ and ρ functions (red line).

III. THE LEVEL DENSITY

Through the global fitting to the data points the functional form of ρ is determined. The absolute normalization of the function as well as the slope remains to be found. These coefficients are found by normalizing Eq. (5) to known experimental data. At low excitation energy it is assumed that all levels are known from discrete spectroscopy. The level density is normalized to these levels; the result can be viewed in the lower panel of Fig. 3. At higher excitation energies ρ is normalized to the level density determined from the known neutron resonance spacing data [13] at the neutron binding energy B_n. To calculate the level density at B_n, the back-shifted Fermi gas model was used [14,15]:

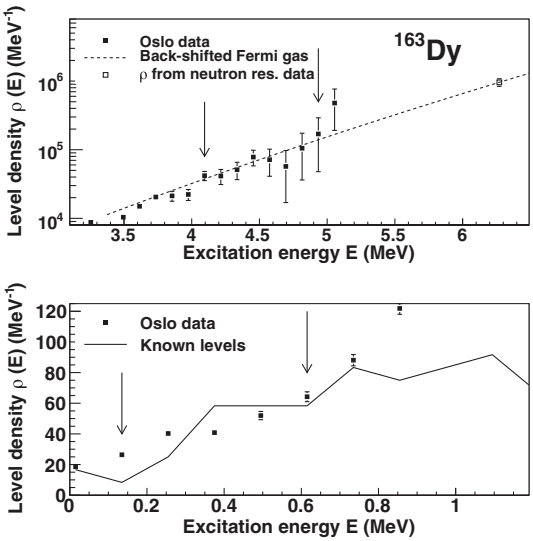

FIG. 3. Normalization of the level densities of ^{163}Dy to neutron resonance data (upper panel) and to discrete levels (lower panel). The regions in between the arrows are used for normalization.

$$\rho(U,J)=\frac{\sqrt{\pi}}{12}\frac{\exp(2\sqrt{aU})}{a^{1/4}U^{5/4}}\frac{(2J+1)\exp[-(J+1/2)^2/2\sigma^2]}{2\sqrt{2\pi}\sigma^3}, \tag{7}$$

$$\rho(U)=\frac{\exp(2\sqrt{aU})}{12\sqrt{2}a^{1/4}U^{5/4}\sigma}, \tag{8}$$

where $\rho(U,J)$ represents the level density for both parities for a given spin J, and $\rho(U)$ is the level density for all spins and parities. The parameter σ gives the spin dependence and a is the level density parameter. The intrinsic excitation energy is given by U.

The neutron resonance spacing D for s-wave neutron capture can be expressed as follows:

$$\frac{1}{D}=\frac{1}{2}\left[\rho\left(B_n, J=J_t+\frac{1}{2}\right)+\rho\left(B_n, J=J_t-\frac{1}{2}\right)\right], \tag{9}$$

where J_t is the spin of the target nucleus in neutron capture. Here we assume that both parities contribute equally to the level density at the neutron binding energy B_n [4]. As recently reported in Ref. [16], calculations of the parity asymmetry of ^{163}Dy and ^{164}Dy show that it approaches zero as a function of excitation energy; in fact it is approximately zero from

TABLE I. Parameters used for normalizing ρ.

Nucleus	E_{pair} (MeV)	C_1 (MeV)	a (MeV^{-1})	D (eV)	$\sigma(B_n)$	B_n (MeV)	$\rho(B_n)$ (10^6 MeV^{-1})	J_t
^{163}Dy	0.661	−1.293	17.653	62(5)	5.408	6.271	0.96(12)	0
^{164}Dy	1.707	−1.291	17.747	6.8(6)	5.492	7.658	1.74(21)	$\frac{5}{2}$

around 4 MeV, which is far lower than B_n. When combining Eqs. (7)–(9) one can obtain an expression for the level density at the neutron binding energy of

$$\rho(B_n)=\frac{2\sigma^2}{D}\frac{1}{(I+1)\exp(-(I+1)^2/2\sigma^2)+I\exp(-I^2/2\sigma^2)}, \tag{10}$$

where the spin-cutoff σ is calculated as follows [15]:

$$\sigma^2 = 0.0888\sqrt{aB_n}A^{2/3}, \tag{11}$$

and A is the mass number of the nucleus.

The experimental data extend up to about $B_n - 1$ MeV; an interpolation is thus required to reach B_n. The back-shifted Fermi gas model [14,15] was applied for this purpose:

$$\rho_{\text{bs}}(E) = \eta\frac{\exp(2\sqrt{aU})}{12\sqrt{2}a^{1/4}U^{5/4}\sigma}. \tag{12}$$

The intrinsic excitation energy is given by $U = E - C_1 - E_{\text{pair}}$, where C_1 is the back-shift parameter equal to $C_1 = -6.6A^{-0.32}$ MeV. The pairing energy E_{pair} is based on the pairing gap parameters Δ_p and Δ_n evaluated from odd-even mass differences [17] according to Ref. [18]. The spin-cutoff parameter σ is given by $\sigma^2 = 0.0888aTA^{2/3}$, where the nuclear temperature is described by

$$T = \sqrt{U/a}. \tag{13}$$

The back-shifted Fermi gas model of Eq. (12) must be scaled in order to fit the level density calculated at B_n using the experimentally determined neutron resonance spacing. This is done through the parameter η, which is equal to 0.52 and 0.56 for ^{163}Dy and ^{164}Dy, respectively. The normalization at high excitation energy for ^{163}Dy is displayed in the upper panel of Fig. 3. All the parameters used in the normalization are given in Table I.

Note that the uncertainties displayed in Fig. 3 only reflect statistical uncertainties and do not include the uncertainties related to the model used for normalization. This is also the case for the other figures showing experimental data. We have chosen the present parametrization for normalization in order to be consistent with previous work on $^{160-162}$Dy.

The normalized ρ of both nuclei are displayed in Fig. 4. We observe a characteristic steplike structure in the level density of the even-even ^{164}Dy nucleus. Similar structures are observed in several rare earth isotopes, in particular for even-even nuclei. Microscopic calculations based on the seniority model indicate that step structures in the level density can be explained by the consecutive breaking of nucleon Cooper pairs [1]. The discrete levels below the plateau located beneath 1 MeV of excitation energy are caused by rotational modes of the nucleus.

We observe a steep slope of the level density around 1.6 MeV for ^{164}Dy, which corresponds to twice the pairing gap parameters, $2\Delta_n = 1.66$ MeV and $2\Delta_p = 1.75$ MeV, which is the expected energy needed to break a neutron and proton pair, respectively. The even-odd nucleus already has an unpaired neutron at low energies. Due to the smearing effect of this valence neutron we cannot identify as easily the breaking of Cooper pairs in ^{163}Dy by studying the level density directly. In the following we will investigate this further by studying the thermodynamics of the nucleus.

IV. THERMAL PROPERTIES

The micro-canonical ensemble describes an isolated system with fixed total energy E and volume size V. The micro-canonical ensemble is often preferred as the proper framework when describing a nucleus. One can justify this because the nuclear force has a very short range, and the nucleus does normally not share its excitation energy with its surroundings. It is therefore fair to consider the nucleus as an isolated system. However, the drawback for applying this ensemble is that some thermodynamic properties, such as the temperature T and heat capacity C_V, can show huge fluctuations and even negative values. If one applies the canonical ensemble, allowing heat

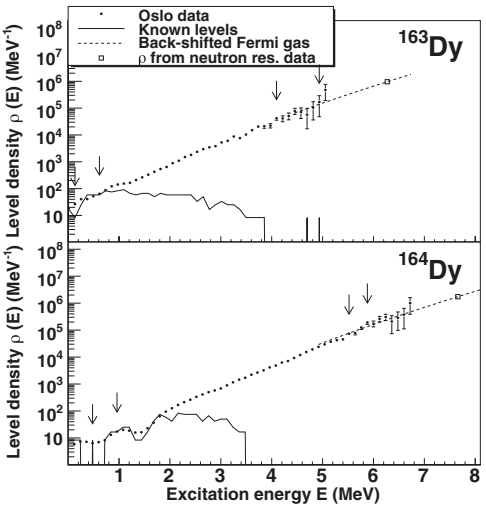

FIG. 4. The normalized level densities of ^{163}Dy (upper panel) and ^{164}Dy (lower panel). The regions in between the arrows are used for normalization.

exchange, these mathematical difficulties are met. However, this approach causes structural changes to be smoothed.

Results obtained from both the micro-canonical and canonical ensemble are given in the following. In both ensembles one observes phaselike transitions as the system goes from a state where all the particles are coupled to a less correlated or uncorrelated state.

A. Micro-canonical ensemble

The micro-canonical partition function is given by the multiplicity of states $\Omega(E)$, which is directly proportional to the level density and a spin dependent factor:

$$\Omega_s(E) \propto \rho(E)(2\langle J(E)\rangle + 1), \tag{14}$$

where $\langle J(E)\rangle$ represents the average spin at excitation energy E. The $2\langle J\rangle + 1$ degeneracy of magnetic substates is not known, because there exist little experimental data regarding the spin distribution. We have therefore chosen to work with a multiplicity solely depending on the experimental level density:

$$\Omega_l(E) = \frac{\rho}{\rho_0}, \tag{15}$$

where ρ_0 is a constant used for normalization.

The level density is our starting point for extracting thermodynamic properties of the nucleus. The entropy S is then described by

$$S = k_B \ln \Omega_l(E) = k_B \ln \rho(E) + S_0, \tag{16}$$

where $S_0 = -k_B \ln \rho_0$. The constant S_0 is a normalization factor adjusted to fulfill the third law of thermodynamics, which states that the entropy approaches a constant value as the temperature goes to zero. In the even-even nucleus ^{164}Dy, there is only one possible configuration in the ground state, and thus the ground-state entropy should be $S = \ln 1 = 0$. The normalization factor is calculated to be $S_0 = -2.08k_B$ to fulfill this requirement. The same value is used in ^{163}Dy; however, there are more possible configurations at low temperature in this nucleus and therefore the entropy has a nonzero value at low temperature.

The extracted entropies are displayed in Fig. 5. We observe a near-constant entropy difference between the two nuclei. As was reported in an earlier work [19], the entropy excess ΔS may be interpreted as the single-quasiparticle entropy. In this case the entropy can be expressed by

$$S = nS_1, \tag{17}$$

where n is the number of quasiparticles and S_1 is the single-quasiparticle entropy. The entropy difference is almost constant in the region above an excitation energy of 2 MeV. After performing a least-squares fit in this region the entropy difference is found to be $S_1 = 1.94(1)k_B$. This suggests that the entropy is an extensive function with respect to the number of quasiparticles (as opposed to macroscopic systems where it is an extensive quantity which scales with the volume of the system). This is a rather surprising result that contradicts the well-established Fermi gas model, which is often applied to model the level density.

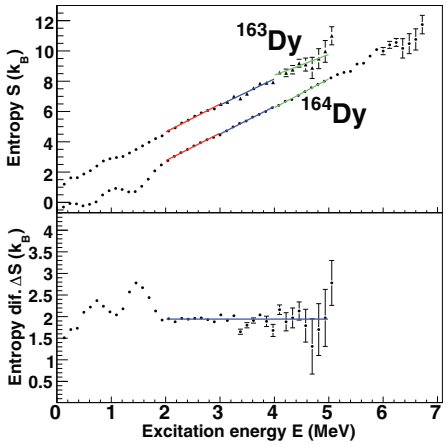

FIG. 5. (Color online) Upper panel: The micro-canonical entropies of ^{163,164}Dy, where the solid lines represents a linear fit to the data points to obtain the temperature in different energy regions. Lower panel: The entropy difference between ^{163}Dy and ^{164}Dy, where the solid line gives the average entropy difference in the energy region E_i = 2–5 MeV.

Other thermodynamic quantities such as temperature and heat capacities are derived from the entropy. The temperature T for a system in equilibrium is given by

$$T = \left(\frac{\partial S}{\partial E}\right)^{-1}_V. \tag{18}$$

The temperature of the systems is found by applying Eq. (18), which corresponds to the inverse slope of the entropy displayed in Fig. 5. The slopes were found through a least-squares fit to the experimental entropy. However, we observe in Fig. 5 that the functional form of the entropy is not linear but has some structure and a slight curvature. This results in different temperatures in different energy regions. We have therefore performed a fit in three energy regions, namely the 2–3, 3–4, and 4–5 MeV regions. The fits are displayed as solid lines in the upper panel of Fig. 5. The entropies of $^{160-162}$Dy, taken from the experiments discussed in Ref. [20], are displayed in Fig. 6. Similarly, the temperatures of $^{160-162}$Dy have been extracted within the three energy regions. The fits are indicated in Fig. 6 and all the temperatures are given in Table II. The average temperatures have been extracted within the three regions for all the mentioned dysprosium nuclei, and the results are displayed in Fig. 7. We observe from Fig. 7 and Table II that the lowest energy region has a lower temperature for all the nuclei, with an average of $T_{2\text{–}3\,\mathrm{MeV}} = 0.51(2)$ MeV. The two higher energy regions have a more similar temperature of $T_{3\text{–}4\ \mathrm{MeV}} = 0.60(2)$ MeV and $T_{4\text{–}5\,\mathrm{MeV}} = 0.57(3)$ MeV, and thus they agree within the uncertainties. Note that the highest energy region in ^{161}Dy and ^{163}Dy is close to the neutron separation energy and therefore the uncertainties are rather high.

In Ref. [21] temperatures of some dysprosium isotopes were found using a constant-temperature formula of the level

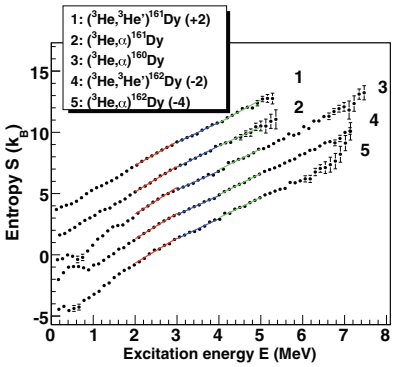

FIG. 6. (Color online) The entropies of $^{160-162}$Dy obtained from (^{3}He,^{3}He′) (filled symbols) and (^{3}He,α) (open symbols). The red, blue, and green lines display least-squares fit to the experimental data in the energy regions $E = 2$–3, 3–4, and 4–5 MeV, respectively. Various entropy curves are shifted as indicated in the parentheses for better visualization.

density, fitted to a level density derived from the low energy level schemes and neutron resonance densities. The following temperatures were found: $T_{^{161}\mathrm{Dy}} = 0.57(3)$, $T_{^{162}\mathrm{Dy}} = 0.58(1)$, $T_{^{163}\mathrm{Dy}} = 0.59(2)$ and $T_{^{164}\mathrm{Dy}} = 0.58(1)$. This is in excellent agreement with the temperatures found from this dataset in the region above an excitation energy of 3 MeV.

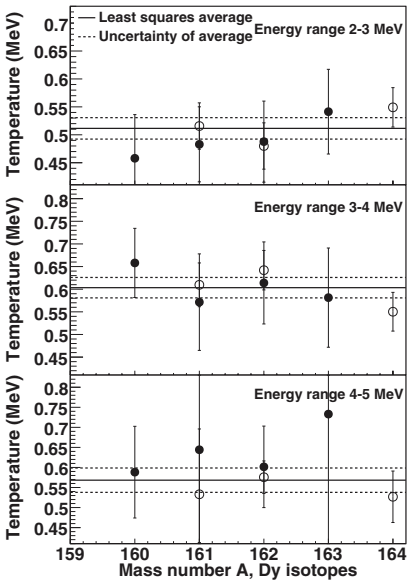

FIG. 7. The average temperature calculated in the excitation energy regions $E = 2$–3 MeV (upper panel), $E = 3$–4 MeV (central panel), and $E = 4$–5 MeV (lower panel). The filled circles represents nuclei obtained from the (^{3}He,^{3}He′) reaction while the open circles corresponds to (^{3}He,α).

TABLE II. Least-squares average of temperature in different energy regions.

Nucleus/energy region	2–3 MeV	3–4 MeV	4–5 MeV
(^{3}He,α)^{160}Dy	0.46(8)	0.66(8)	0.59(11)
(^{3}He,α)^{161}Dy	0.52(4)	0.61(5)	0.53(16)
(^{3}He,^{3}He)^{161}Dy	0.48(7)	0.57(11)	0.64(23)
(^{3}He,α)^{162}Dy	0.48(4)	0.64(4)	0.57(4)
(^{3}He,^{3}He)^{162}Dy	0.49(7)	0.61(9)	0.60(10)
(^{3}He,α)^{163}Dy	0.54(8)	0.58(11)	0.73(48)
(^{3}He,^{3}He)^{164}Dy	0.55(4)	0.55(4)	0.53(6)
Average	0.51(2)	0.60(2)	0.57(3)

Viewing Fig. 6 we observe structure in the entropy, especially pronounced in ^{160}Dy. This is again interpreted as pair breakups, and in ^{160}Dy also more than one broken pair can be identified. The largest difference in the temperature when comparing the excitation energy regions is found in ^{160}Dy, where the temperatures are $T_{2\text{–}3} = 0.46(8)$ MeV and $T_{3\text{–}4} = 0.66(8)$ MeV. This is probably due to these structures we observe.

A slight change in the entropy will result in significant fluctuations in the temperature, as shown in Fig. 8. The microcanonical heat capacity C_V is given by

$$C_V = \left(\frac{\partial T}{\partial E}\right)_V. \tag{19}$$

Because negative slopes of the temperature occur this will create negative values of the heat capacities. In Fig. 8 the

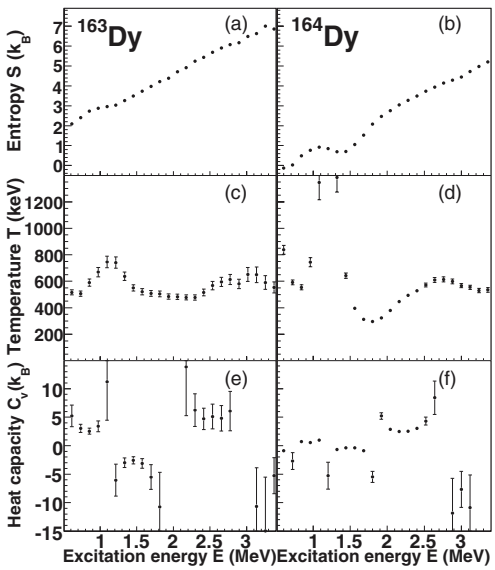

FIG. 8. Entropy (upper panel), temperature (middle panel), and heat capacity (lower panel) as a function of excitation energy in ^{163}Dy (left) and ^{164}Dy (right).

temperatures and heat capacities are displayed together with the entropy for both nuclei. The negative branches of the heat capacities can be identified as the breaking of nucleon Cooper pairs, which results in a first-order phase transition. Negative heat capacities are not observed in macroscopic systems, but they have been observed in other microscopic systems [22]. The low-energy region is displayed in Fig. 8 to illustrate how the first broken pairs can be identified. At higher energies the transitions are harder to identify due to the smoothening of the already broken pairs.

It should be noted that the region below 2Δ in Fig. 8 is dominated by collective excitations, especially for ^{164}Dy, which has no valence neutron. It is therefore a challenge to interpret the temperature and heat capacity at such low excitation energies, since rotational states are considered to be cold. Therefore, we do not take these low-energy data points into consideration when interpreting the thermodynamic quantities.

B. Canonical ensemble

The partition function of the canonical ensemble is expressed as the Laplace transformation of the multiplicity of states $\Omega(E_i)$,

$$Z(T) = \sum_{i=0}^{\infty} \Omega(E_i) e^{-E_i/k_B T}, \tag{20}$$

where $\Omega(E_i) = \delta E_i \rho(E_i)$, and where E_i is the excitation energy, δE_i is a small energy interval, and $\rho(E_i)$ represents the level density at excitation energy E_i. The sum of the above equation runs from zero to infinity; however, the experimental level density is only extracted up to the neutron binding energy B_n. Above this region the level density has reached the quasicontinuum and is expected to follow the Fermi gas model expression given by Eq. (12).

From the partition function all other thermodynamic quantities in the canonical ensemble can be derived. The Helmholtz free energy F is defined by

$$F(T) = -k_B T \ln Z(T). \tag{21}$$

The canonical entropy S, average energy $\langle E \rangle$, and heat capacity C_V are given by the three following equations:

$$S = -\left(\frac{\partial F}{\partial T}\right)_V, \tag{22}$$

$$\langle E \rangle = -T^2 \left(\frac{\partial (F/T)}{\partial T}\right)_V, \tag{23}$$

$$C_V = -T \left(\frac{\partial^2 F}{(\partial T)^2}\right)_V, \tag{24}$$

respectively.

In Fig. 9 the canonical temperature is displayed together with the micro-canonical temperature for ^{164}Dy. Due to the strong smoothening introduced by the transformation to the canonical ensemble we do not observe clear transitions between the various quasiparticle regimes as we do in the micro-canonical ensemble, but only at the transition where all pairing correlations are quenched as a whole. With this in mind the results extracted within the canonical framework

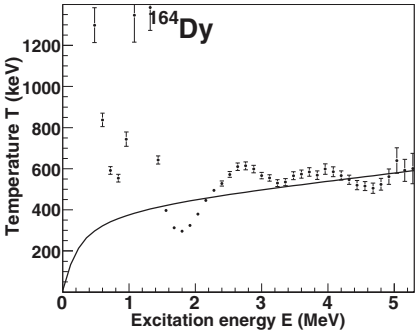

FIG. 9. The temperature of ^{164}Dy derived within the micro-canonical ensemble (circles) and the canonical ensemble (line).

are presented. The canonical entropy, average energy, and heat capacities are displayed in Fig. 10, for both nuclei. We observe in the upper panel of Fig. 10 a clear entropy difference between the two nuclei at temperatures below $T \leqslant 0.5$–0.6 MeV, where the odd-A ^{163}Dy nucleus has the highest entropy. For the lowest temperature we observe an entropy difference of $\approx 2k_B$ between the two nuclei, which is of the same order as in the micro-canonical ensemble. At around $T = 0.5$–0.6 MeV the entropies of the even-odd and even-even systems approach

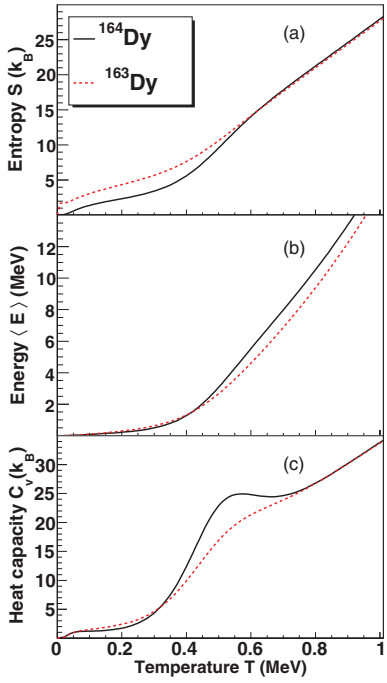

FIG. 10. (Color online) The canonical entropy (a), average energy (b), and heat capacity (c) of ^{163}Dy (dashed line) and ^{164}Dy (solid line).

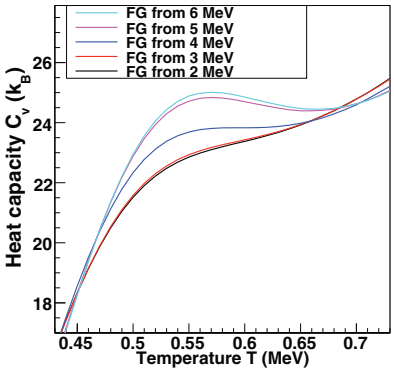

FIG. 11. (Color online) The heat capacities of ^{163,164}Dy derived from level density functions which have been varied according to a normal distribution.

each other; this corresponds to an average excitation energy of $\langle E \rangle = 2.7$–4.6 MeV in ^{163}Dy and $\langle E \rangle = 3.1$–5.5 MeV in ^{164}Dy. Above this region the entropy curves coincide and display almost identical behavior. Also the entropies of ^{161,162}Dy coincide at approximately the same temperature [19], and the forms of these entropies are very similar to what we observe in ^{163,164}Dy. This is because pairing is expected to play a less significant role as the level density becomes high. Naively, we expect that adding two additional quasiparticles to ^{163}Dy hardly has any effect on the entropy, when in a region of high temperature.

The average excitation energies $\langle E \rangle$ behave smoothly as a function of temperature, as shown in the central panel of Fig. 10. We observe that ^{164}Dy has a higher $\langle E \rangle$ than the neighboring ^{163}Dy nucleus as a function of temperature. In Ref. [23] a model based on the canonical ensemble theory was applied to perform calculations for nuclei around ^{162}Dy. It was found that even-even, odd-even/even-odd, and odd-odd systems have different excitation energies at the same temperature, and the even-even system requires the highest $\langle E \rangle$ value. This is also confirmed by experimental data (for example in Ref. [20]) for ^{160,161}Dy.

In Fig. 10 we observe the characteristic S shape of the heat capacity of ^{164}Dy, which is interpreted as a fingerprint of a phase transition. The S shape is much weaker for ^{163}Dy, displayed in the same figure. In Ref. [24] two different critical temperatures were discovered in the canonical ensemble using the method discussed in Refs. [25,26]. The lowest critical temperature is explained by the first breakup of Cooper pairs. The second critical temperature is due to the continuous melting of Cooper pairs at higher excitation energies. We see an increase in the heat capacity around temperature $T \approx 0.45$–0.55 MeV in the ^{164}Dy nucleus, which may be interpreted as the first critical temperature. This first contribution is strongest for ^{164}Dy because this is an even-even nucleus and thus the first broken pair represents a large and abrupt step in the level density and thereby a large contribution to the heat capacity. The second critical temperature can be observed at about $T \approx 0.55$–0.65 MeV and agrees with the region where the entropy curves coincide. Similar features for the heat capacity as discussed here have been observed for ^{160,161}Dy [20].

There are no error bars displayed in Fig. 10. Since all the thermodynamic quantities are derived from the experimental level density, possible uncertainties must stem from this function. To ensure that the uncertainties do not exceed the odd-even differences the level densities of ^{163,164}Dy have been varied according to a normal distribution $N(\mu, \sigma)$, with the experimentally determined μ and standard deviation σ. Figure 11 displays the heat capacities of ^{163,164}Dy with 30 variations of the heat capacity for both nuclei. We note that varying the level density produces slightly different heat capacities; however, these differences are of a much smaller scale than the odd-even differences.

We continue the discussion of whether the micro-canonical temperature is constant or varying as a function of excitation energy, by studying the canonical heat capacity. First, we have compared the level density of ^{164}Dy calculated from the Fermi gas model to a constant-temperature level density, satisfying $T = 0.5$ MeV in the micro-canonical ensemble. The results are displayed in the left panel of Fig. 12. The Fermi gas level density resembles to some degree the experimental functions. However, the Fermi gas model gives a strong curvature of the level density, when viewed on a logarithmic

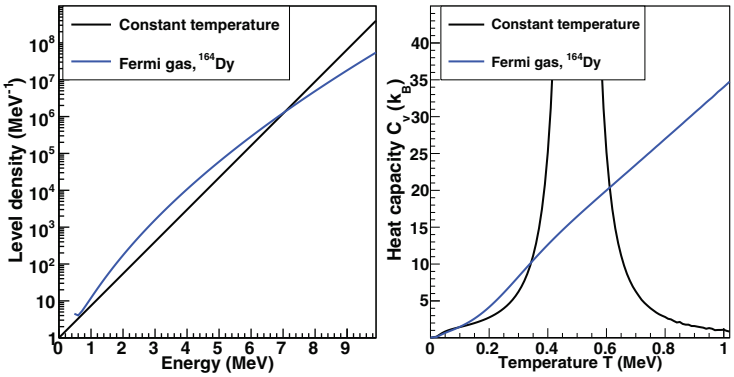

FIG. 12. (Color online) Left panel: The level density of ^{164}Dy calculated from the Fermi gas model and from a constant-temperature level density. Right panel: The corresponding heat capacities.

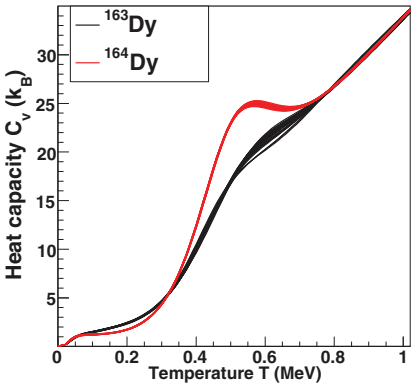

FIG. 13. (Color online) The heat capacities of ^{164}Dy derived from the level density, where the Fermi gas extrapolation is taken from different temperatures.

scale. The corresponding experimental function displays a more or less constant slope above an excitation energy of 3 MeV. In the right panel of the same figure the canonical heat capacities are displayed. The constant-temperature level density diverges around $T = 0.5$ MeV, while the Fermi gas level density gives a heat capacity which resembles more the ones displayed in Fig. 10, although it hardly gives any phase transition as observed in Fig. 10. However, the presence of some linear behavior of the entropy may induce strong S-shape-like behavior for the heat capacity. It is interesting to investigate what gives rise to the characteristic S shape of the heat capacities in even-even nuclei.

Figure 13 displays the heat capacities found from the level density, where the experimental level density has been replaced by a Fermi gas function above five different excitation energies: 2, 3, 4, 5, and 6 MeV. It is interesting to see that the region of constant temperature, with an excitation energy of 3–5 MeV, contributes significantly to the second-order phase transition. However, we can clearly identify a phase transition also when only including experimental data below an excitation energy of 2 MeV, although this transition is weaker. This is in the same region where we observe the step structure in the entropy, thought to be caused by the first pair splittings. There are thus several features that determines the shape of the heat capacity.

V. CONCLUSIONS

The level density and thermodynamic quantities of $^{160–164}$Dy have been extracted by use of the Oslo method. The level density displays the characteristic step structure seen at low excitation energy in several rare earth isotopes. The step is most pronounced in the even-even nuclei, which also coincides with previous findings.

We observe transitions between the various quasiparticle regimes when studying thermodynamical properties within the framework of the micro-canonical ensemble. The micro-canonical temperatures for $^{160–164}$Dy have been extracted within three energy regions, $E = 2–3$, 3–4, and 4–5 MeV. We have found that the temperature increases up to $E \sim 3$ MeV and then remains approximately constant due to the continuous breaking of nucleon pairs. In the canonical ensemble we observe a second-order phase transition, influenced by the first broken pairs of the nucleus, but also the later breaking of Cooper pairs enhances the phase transition significantly. In results obtained from the canonical ensemble we observe a transition to a state where pair correlations no longer play a central role.

ACKNOWLEDGMENTS

The authors would like to thank E. A. Olsen and J. Wikne for excellent experimental conditions. Financial support from the Research Council of Norway, Grant No. 180663, is gratefully acknowledged.

[1] A. Schiller *et al.*, Phys. Rev. C **68**, 054326 (2003).
[2] E. Melby, M. Guttormsen, J. Rekstad, A. Schiller, S. Siem, and A. Voinov, Phys. Rev. C **63**, 044309 (2001).
[3] A. Schiller, A. Bjerve, M. Guttormsen, M. Hjorth-Jensen, F. Ingebretsen, E. Melby, S. Messelt, J. Rekstad, S. Siem, and S. W. Ødegård, Phys. Rev. C **63**, 021306(R) (2001).
[4] A. Schiller, L. Bergholt, M. Guttormsen, E. Melby, J. Rekstad, and S. Siem, Nucl. Instrum. Methods Phys. Res., Sect. A **447**, 498 (2000).
[5] M. Guttormsen, A. Atac, G. Løvhøiden, S. Messelt, T. Ramsøy, J. Rekstad, T. F. Thorsteinsen, T. S. Tveter, and Z. Zelazny, Phys. Scr., T **32**, 54 (1990).
[6] M. Guttormsen, T. S. Tveter, L. Bergholt. F. Ingebretsen, and J. Rekstad, Nucl. Instrum. Methods Phys. Res., Sect. A **374**, 371 (1996).
[7] M. Guttormsen, T. Ramsøy, and J. Rekstad, Nucl. Instrum. Methods Phys. Res., Sect. A **255**, 518 (1987).
[8] E. Fermi, *Nuclear Physics* (University of Chicago Press, Chicago, 1950).
[9] D. M. Brink, Ph.D. thesis, Oxford University, 1955.
[10] P. Axel, Phys. Rev. **126**, 671 (1962).
[11] A. Bohr and B. Mottelson, *Nuclear Structure* (Benjamin, New York, 1969), Vol. I, pp. 184–185.
[12] H. T. Nyhus, S. Siem, M. Guttormsen, A. C. Larsen, A. Bürger, N. U. H. Syed, G. M. Tveten, and A. Voinov, Phys. Rev. C **81**, 024325 (2010); **82**, 029909(E) (2010).
[13] T. Belgya *et al.*, *Handbook for Calculations of Nuclear Reaction Data*, RIPL-2, IAEA-TECDOC-1506 (International Atomic Energy Agency, Vienna, 2006).
[14] A. Gilbert and A. G. W. Cameron, Can. J. Phys. **43**, 1446 (1965).
[15] T. von Egidy, H. H. Schmidt, and A. N. Behkami, Nucl. Phys. A **481**, 189 (1988).
[16] A. C. Larsen *et al.*, Phys. Rev. C **83**, 034315 (2011).
[17] A. Audi and A. H. Wapstra, Nucl. Phys. A **595**, 409 (1995).
[18] A. Bohr and B. Mottelson, *Nuclear Structure* (Benjamin, New York, 1969), Vol. I, pp. 169–171.

[19] M. Guttormsen, A. Bjerve, M. Hjorth-Jensen, E. Melby, J. Rekstad, A. Schiller, S. Siem, and A. Belić, Phys. Rev. C **62**, 024306 (2000).
[20] M. Guttormsen, A. Bagheri, R. Chankova, J. Rekstad, S. Siem, A. Schiller, and A. Voinov, Phys. Rev. C **68**, 064306 (2003).
[21] T. von Egidy and D. Bucurescu, Phys. Rev. C **80**, 054310 (2009).
[22] Ph. Chomaz, V. Duflot, and F. Gulminelli, Phys. Rev. Lett. **85**, 3587 (2000).
[23] M. Guttormsen, M. Hjorth-Jensen, E. Melby, J. Rekstad, A. Schiller, and S. Siem, Phys. Rev. C **64**, 034319 (2001).
[24] M. Guttormsen, R. Chankova, M. Hjorth-Jensen, J. Rekstad, S. Siem, A. Schiller, and D. J. Dean, Phys. Rev. C **68**, 034311 (2003).
[25] J. Lee and J. M. Kosterlitz, Phys. Rev. Lett. **65**, 137 (1990).
[26] J. Lee and J. M. Kosterlitz, Phys. Rev. B **43**, 3265 (1991).

6.4 Paper III: Energy Calibration of the NewSUBARU Storage Ring for Laser Compton-Scattering Gamma Rays and Applications

Energy Calibration of the NewSUBARU Storage Ring for Laser Compton-Scattering Gamma Rays and Applications

Hiroaki Utsunomiya, Tatsushi Shima, Keiji Takahisa, Dan Mihai Filipescu, Ovidiu Tesileanu, Ioana Gheorghe, Hilde-Therese Nyhus, Therese Renstrøm, Yiu-Wing Lui, Yasuhisa Kitagawa, Sho Amano, Shuji Miyamoto

***Abstract*—Using γ-ray beams produced in the inverse Compton scattering between CO_2 laser photons and relativistic electrons, we have calibrated electron beam energies in the nominal energy range 550 - 974 MeV at the synchrotron radiation facility NewSUBARU. The laser Compton-scattering (LCS) γ-ray beams were produced at energies from 561 keV to 1728 keV and detected with a high-purity germanium detector. The electron beam energies were determined by reproducing the full energy peaks of the γ-ray beams by Monte Carlo simulations. The accuracy of the calibration is (5.5 - 9.4) $\times$ 10^{-5}. The reproducibility of the electron beam energy is excellent in an independent injection and deceleration. The present energy calibration of the electron beams offers a standard for the energy calibration of high-energy LCS γ-ray beams produced with a Nd:YVO_4 laser. As applications of the energy calibration, we investigated the energy linearity of a 3.5" $\times$ 4.0" $LaBr_3$(Ce) detector in the response to γ rays at energies up to 10 MeV and the energy profile of the high-energy LCS γ-ray beams.**

I. Introduction

QUASIMONOCHROMATIC γ-ray beams are produced at the synchrotron radiation facility NewSUBARU in the inverse Compton scattering of laser photons from relativistic electrons circulating in a storage ring [1], [2]. A beam of 974 MeV electrons is injected from a linear accelerator into the NewSUBARU storage ring. The energy represents a relative value with $\sim$ 1% uncertainty based on the magnetic field strength and the beam optics of the storage ring [3] and is hereafter referred to as the nominal energy in this paper. The injected beam can be either decelerated down to 0.5 GeV or accelerated up to 1.5 GeV.

H. Utsunomiya is with Department of Physics, Konan University, Okamoto 8-9-1, Higashinada, Kobe 658-8501, Japan and Center for Nuclear Study, University of Tokyo, 2-1 Hirosawa, Wako, Saitama 351-0198, Japan (telephone: +81-78-435-2471, e-mail: hiro@ konan-u.ac.jp).

T. Shima and K. Takahisa are with Research Center for Nuclear Physics, Osaka University, Suita, Osaka 567-0047, Japan.

D. M. Filipescu is with Extreme Light Infrastructure Nuclear Physics and National Institute for Physics and Nuclear Engineering Horia Hulubei, str Atomistilor nr. 407, Bucharest-Magurele, P.O.BOX MG6, Romania.

O. Tesileanu is with Extreme Light Infrastructure Nuclear Physics, str Atomistilor nr. 407, Bucharest-Magurele, P.O.BOX MG6, Romania.

I. Gheorghe is with National Institute for Physics and Nuclear Engineering Horia Hulubei, str Atomistilor nr. 407, Bucharest-Magurele, P.O.BOX MG6, Romania.

H. T. Nyhus and T. Renstrøm are with Department of Physics, University of Oslo, N-0316 Oslo, Norway.

Y.-W. Lui is with Cyclotron Institute, Texas A&M University, College Station, Texas 77843, USA.

Y. Kitagawa, S. Amano and S. Miyamoto are with Laboratory of Advanced Science and Technology for Industry, University of Hyogo, 3-1-2 Kouto, Kamigori, Ako-gun, Hyogo 678-1205, Japan.

In the laser inverse Compton scattering, the energy of scattered photons is given by

$$E_\gamma = \frac{4\eta^2 \varepsilon_L}{1 + (\eta\theta)^2 + 4\eta\varepsilon_L/(mc^2)}, \quad (1)$$

where ε_L is the energy of a laser photon, mc^2 is the rest mass energy of an electron, θ is the scattering angle of a laser photon with respect to the electron incident direction, and η is the Lorentz factor for electron, $\eta = E_e/mc^2$, defined by the total electron energy E_e and the rest mass energy.

The energy amplification factor in nearly head-on collisions ($\theta \approx 0$), E_γ /$\varepsilon_L \approx 4\eta^2$, is very large on the order of 10^6 - 10^7 for several hundred MeV to a few GeV electrons (1.6 $\times$ 10^7 for E_e = 1 GeV) so that an eV laser beam can be converted to an MeV γ-ray beam in the laser inverse Compton scattering. Note that the numerator in Eq. (1) is a dominating factor to determine the LCS γ-ray energy. At NewSUBARU, one can produce low-energy γ-ray beams at a few MeV using a CO_2 laser (wave length λ=10.59μm) and high-energy γ-ray beams at a few tens of MeV using a Nd:YVO_4 laser (λ=1064nm) in collisions with 0.5 - 1.0 GeV electrons.

It is not straightforward to calibrate the energy of the LCS γ-ray beam in the region of a few tens of MeV for a lack of proper γ-ray sources. A high-resolution germanium detector may be used for calibration. However, the standard γ-ray sources can cover only low energies so that a linear extrapolation must be employed to extend the energy range to high energies. It may not be surprising that such extrapolation causes uncertainties of $\sim$ 50 keV around 10 MeV. Furthermore, a large-volume Ge detector is needed to detect a high-energy edge corresponding to the full-energy (FE) peak for 10 MeV γ rays if it may not identify the FE peak as an isolated peak.

One can see by setting θ = 0 in Eq. (1) that the maximum energy of the LCS γ-ray beam can be determined if the electron beam energy is known. It is, however, risky to rely on the nominal energy because the 1% uncertainty results in 2% uncertainty in the maximum γ-ray energy. Obviously, one derives from Eq. (1)

$$\frac{\Delta E_\gamma}{E_\gamma} \approx 2\frac{\Delta E_e}{E_e}. \quad (2)$$

We searched the neutron threshold for ^{197}Au located at 8.07 MeV [4] by detecting neutrons from ^{197}Au(γ,n) reactions with

a 2 mm-thick ^{197}Au target. LCS γ-ray beams were produced with a Nd:YVO_4 laser and electron beams at the nominal electron energies from 677 to 661 MeV in steps of 2 MeV. By changing the electron-beam energy by 2 MeV, we changed the γ-ray energy by $\sim$ 50 keV. Note that electrons at 676.43 MeV produce an LCS γ-ray beam with the maximum energy at the neutron threshold for ^{197}Au. Neutrons were detected with a 4π neutron detector consisting of 20 ^{3}He proportional counters embedded in a polyethylene moderator. Statistically significant events were observed above the nominal energy 667 MeV, indicating that the neutron threshold lies between two LCS γ-ray energies produced by electrons at the nominal energies of 667 and 665 MeV. This observation led to the fact that there is 1.4 - 1.7% discrepancy between real and nominal energies in this energy region; the real energy is higher than the nominal energy.

The threshold search for ^{197}Au showed that absolute calibration of electron beam energies is of critical importance to photoneutron cross section measurements near neutron threshold with LCS γ-ray beams. We performed absolute calibration of electron beam energies of the storage ring NewSUBARU in the nominal energy range of 0.55 - 1.0 GeV. In this paper, we report results on the calibration of the NewSUBARU and applications of calibrated electron beams.

II. Experiment

The technique of laser Compton backscattering has been developed to accurately determine electron beam energies as an alternative to the technique of the resonant spin depolarization which is limited to high energy electrons because of the spin depolarization time [6]. This technique was widely used to calibrate electron beam energies by using low-energy LCS γ-ray beams produced with a CO_2 laser [5], [7], [8], [9] and a free electron laser [10] at different facilities worldwide. Unlike the past calibrations, however, we performed the energy calibration systematically in the following five steps; (1) production of low-energy LCS γ-ray beams in collisions of CO_2 laser photons with electrons at ten nominal energies from 974 MeV to 550 MeV; (2) measurements of LCS γ-ray beams with a high-purity germanium (HPGe) detector; (3) energy calibration of the HPGe detector with the standard γ-ray sources; (4) determination of electron beam energies by Monte Carlo simulations, and (5) study of the accuracy and the reproducibility of the electron beam energies.

Figure 1 depicts the experimental setup for the present measurement in the γ-ray beam line BL01 of the NewSUBARU synchrotron radiation facility. An electron beam was injected from the linear accelerator into the NewSUBARU storage ring at the nominal energy 974 MeV. A grating-fixed CO_2 laser (INFRARED INSTRUMENTS, IR-10-WS-GF-VP) oscillated at a single line of the strongest master transition P(20). The central wave length of the P(20) transition is known (λ =10.5915μm $\pm$ 3Å) [11] with the band width 1.3Å in the full width at half maximum FWHM [12]. The band width, i.e. the gain linewidth 340 MHz in FWHM, was provided by the INFRARED INSTRUMENTS. Including the band width, the accuracy of the wave length of CO_2 laser is 4.1 $\times$ 10^{-5}.

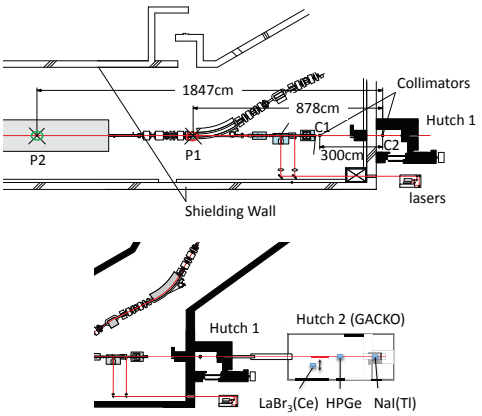

Fig. 1. Experimental setup.

The CO_2 laser photons produced outside the storage ring vault were led through four mirrors and one lens into the vacuum tube of the ring to a collision point P1 in the straight section of the storage ring. The alignment and stability of the laser optical elements were carefully checked by sending a He-Ne laser beam into the straight section of the ring from the upstream on the other side of the beam line and back to the center of the exit of the CO_2 laser through the optical elements. The collision point P1 for the CO_2 laser is located at the distance of 878cm from a collimator set in the experimental Hutch 1. The collision between laser photons and electrons takes place with the maximum collision efficiency at P1, where the electron beam forms a narrow waist in the beam optics [1]. In contrast, the collision point P2 for the Nd:YVO_4 laser is located at 1847cm from the collimator.

The fundamental parameters for the production of low-energy LCS γ-ray beams such as the central wave length (λ) and the band width ($\delta\lambda$) of the CO_2 laser, the size (σ_e), the divergence (θ_e), and the energy spread (δE_e) of the 974 MeV electron beam, and the angle acceptance of the collimator (θ_c) are listed in Table I [1], [13]. The electron beam size at the collision point P1, which is circular, is calculated from the Twiss parameters in the straight section of the ring [1].

The beam line BL01 has two collimators; one (C1) in the storage ring vault and the other (C2) in Hutch 1. Both collimators are made of 10cm thick Pb. In the present experiment, we used the C1 collimator with an aperture of 6mm diameter. The C2 collimator with an aperture of 2mm diameter defined scattering angle for laser Compton backscattering. A NaI(Tl) detector of 6" diameter and 5" thickness was mounted at the end of the beam line in the experimental Hutch 2, GACKO (Gamma collaboration hutch of Konan University), to monitor the γ-ray flux. The C2 collimator was mounted on an x-y-θ stage driven by stepping motors. Fine tunings of the laser

TABLE I

FUNDAMENTAL PARAMETERS FOR THE PRODUCTION OF A LOW-ENERGY LCS γ-RAY BEAM WITH A CO_2 LASER AT THE NOMINAL ELECTRON BEAM ENERGY 974 MEV AT THE NEWSUBARU STORAGE RING: THE CENTRAL LASER WAVE LENGTH λ, THE LASER BAND WIDTH $\delta\lambda$, THE ELECTRON BEAM SIZE σ_e, THE ELECTRON BEAM DIVERGENCE θ_e, THE ELECTRON BEAM ENERGY SPREAD δE_e, AND THE ANGLE ACCEPTANCE OF THE 2MM COLLIMATOR θ_c.

central λ (μm)	band width $\delta\lambda$ FWHM	σ_e (mm)	θ_e (mrad)	δE_e (%)	θ_c (mrad)
10.5915±3Å	1.3 Å	0.3	0.13	0.042	0.11

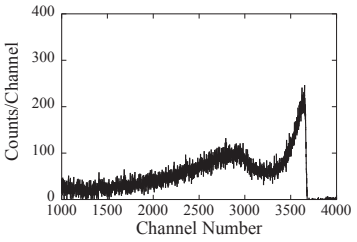

Fig. 2. Response function of the HPGe detector to LCS γ-rays produced in collisions of CO_2 laser photons with electrons at the nominal energy of 850 MeV

optics and the collimator alignment along the horizontal (x), vertical (y) and rotational (θ) axes were carried out to achieve the maximize γ-ray flux. A coaxial HPGe detector (64 mm in diameter $\times$ 60 mm in length) was mounted in GACKO and aligned with synchrotron radiation to measure the low-energy LCS γ rays. The HPGe detector was calibrated with the standard γ-ray sources, ^{60}Co including the sum peak, ^{133}Ba, ^{137}Cs, and ^{152}Eu and a natural radioactivity ^{40}K.

After the injection of 974 MeV electrons into the NewSUBARU storage ring, the electron beam was decelerated to the nominal energy 950 MeV, and subsequently down to 550 MeV in steps of 50 MeV followed by a production of the LCS γ-ray beam and a measurements with the HPGe detector at every energy.

III. RESULTS

A. Response functions of the HPGe detector to LCS γ-ray beams

Figure 2 shows a response function of the HPGe detector to LCS γ-rays produced in collisions of CO_2 laser photons with electrons at the nominal energy of 850 MeV. One can identify the FE peak as well as the Compton scattered component. The FE peak has an energy spread arising from angle acceptance of the 2 mm collimator and the electron beam emittance. Furthermore, the high-energy edge of the FE peak has a slope that reflects the energy resolutions of the electron beam and the HPGe detector. Because of the energy spread and the slope of the FE peak, the electron beam energy cannot be determined analytically using Eq. (1).

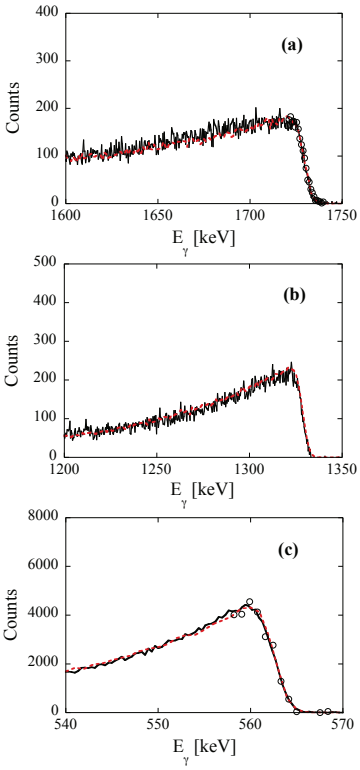

Fig. 3. (a) Monte Carlo simulation (dotted line) with a calibrated energy of the electron beam 982.2 MeV in comparison with the experimental data (solid line) taken at a nominal energy 974 MeV. (b) The same as (a), but for a simulation with a calibrated energy 860.7 MeV in comparison with the data at a nominal energy 850 MeV. (c) The same as (a), but for a simulation with a calibrated energy 559.6 MeV in comparison with the data at a nominal energy 550 MeV.

B. Energy Calibration

The production of LCS γ-rays and the response function of the HPGe detector to the γ-rays were simulated with the Monte Carlo code of Ref. [8]. The EGS4/PRESTA code simulates laser-Compton backscattering and interactions of γ rays with detector materials. The production of γ-rays is based on the kinematics and the cross section for laser Compton backscattering. The cross section in the rest frame of electron is given by the Klein-Nishina formula. The code EGS4 [14] is utilized for the latter simulation.

The effect of the electron beam emittance on the laser Compton backscattering consists of those of the beam size and the beam divergence. The divergence of non-parallel electron beams causes a kinematical effect that increases an angular acceptance of the collimator for Compton backscattering compared to that for parallel beams and has no influence

on the maximum energy of the LCS γ-ray beam which geometrically corresponds to θ=0. The electron beam size defines the size of "a light source" from which LCS γ rays are emitted within a finite solid angle subtended by the collimator. Therefore, the angular acceptance of the collimator increases with increasing the electron beam size compared to that for the point source. As a result, the divergence and size of the electron beam have the same kinematical effect which affects only the energy spread of the LCS γ-ray beam in the Monte Carlo simulation. Thus, the electron beam divergence can be effectively incorporated into the electron beam size though they are different physics quantities, which forms an effective source size [15].

The divergence of the laser beam as well as of the electron beam does not change the maximum energy of the LCS γ-ray beam because it is distributed around zero approximately in a Gaussian function. The maximum allowed misalignment of the laser optics is estimated to be 3mrad for the lens with the Rayleigh length 40cm used for the CO_2 laser with the beam radius 1.2mm. The 3mrad misalignment between the incoming CO_2 laser and 974 MeV electron beam decreases the maximum energy of the LCS γ-ray beam by 3.3×10^{-6}. Therefore, laser misalignment, particularly after tuning the laser optics in the head-on collision geometry by optimizing the intensity of the LCS γ-ray beam, can be safely neglected in the present measurement.

The energy resolution of the HPGe detector can be effectively incorporated into the energy spread of the electron beam, which forms the effective energy spread. The two fitting parameters, the electron beam energy and the effective energy spread have a good control on the position and the slop of the high energy edge of the HPGe response function, respectively, as shown in [6], whereas the effective source size has a good control on the energy spread of the LCS γ-ray beam.

Monte Carlo simulations were carried out to reproduce the FE peak of the response function with three fitting parameters; the electron beam energy, the effective energy spread, and the effective source size (ζ) at the collision point. The parameters of the distance of the collimator from the collision point, the collimator size, the wave length of the CO_2 laser, and the size of the HPGe crystal are fixed.

Examples of the best fits to the spectra are shown in Fig. 3. The FE peaks were well reproduced by the Monte Carlo simulations with the source size ζ = 0.9 - 1.1 mm. The overall energy resolution was taken to be $\Delta E_e/E_e \approx 0.1\%$ in the standard deviation of Gaussian function, which is a quadratic sum of the detector resolution 0.077% (2.43 keV in FWHM for 1332 keV γ rays) and the intrinsic energy spread of the electron beam 0.063%. The estimated energy spread is consistent with the fundamental parameter listed in Table I.

The difference of the calibrated energy E_e^c, thus determined by the Monte Carlo simulation from the nominal energy E_e^n, ΔE = E_e^c -E_e^n is shown in Fig. 4 as a function of E_e^n . The 4th-order polynomial fit to the data gives

$$\Delta E = -4.6949 \times 10^{-10}(E_e^n)^4 + 1.3017 \times 10^{-6}(E_e^n)^3 - 1.3596 \times 10^{-3}(E_e^n)^2 + 0.63854(E_e^n) - 103.94. \quad (3)$$

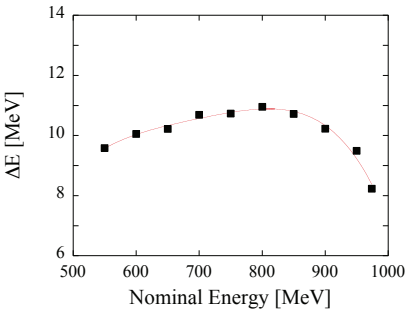

Fig. 4. The difference ΔE of the calibrated energy E_e^c from the nominal energy E_e^n of the electron beams, ΔE = E_e^c -E_e^n, at the NewSUBARU storage ring.

Here E_e^c and E_e^n are given in MeV. The discrepancy of the energy calculated by using Eq. (3) from the calibrated energy is 6 - 215 keV (1×10^{-3}–2×10^{-2} %) at the ten data points. The difference between the nominal and calibrated energies is 10.44 MeV (1.56%) at the nominal energy 667 MeV, being consistent with the result of the neutron-threshold search for ^{197}Au.

C. Accuracy of the electron beam energy

Besides the wave length of the CO_2 laser, the accuracy of the electron beam energy is determined by two factors involved in the response function measurement, i.e., the energy calibration and the counting statistics of the response function [10]. The systematic uncertainty arises from the former factor and the wave length through Eq. (1), while the statistical uncertainty from the latter factor in the least-squares fit to the response functions. The energy calibration of the HPGe detector is shown in Fig. 5. Note that the energy range of the LCS γ-ray beams produced below 1.8 MeV is fully covered by the present calibration. The slope and intercept of the linear fit to the calibration data are given in the figure. The systematic uncertainty for the energy calibration is energy-dependent; it is 7.9×10^{-5} at the nominal energy 550 MeV and 5.4×10^{-5} at 974 MeV, including the accuracy of the wave length (4.1×10^{-5}). We obtained the statistical uncertainty of (1 - 5) $\times 10^{-5}$ in the least-squares fit to the response functions. An example of the dependence of the Monte Carlo simulation on the electron beam energy is shown in Fig. 6. The overall uncertainty in the present calibration over 550 - 974 MeV is (5.5 - 9.4) $\times 10^{-5}$, which is to be compared with the one (3 $\times 10^{-5}$) reported in Ref. [10].

D. Reproducibility of the electron beam energy

To test the reproducibility of the electron beam energy, we aborted the 550 MeV electron beam left in the calibration runs, initialized all the dipole magnets of the storage ring, newly

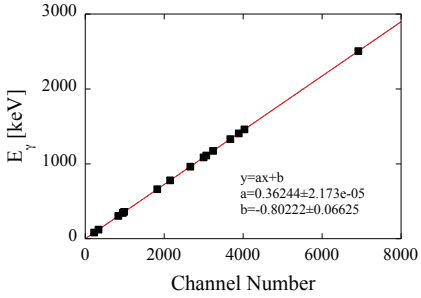

Fig. 5. Energy calibration of the HPGe detector with the standard γ-ray sources and a natural radioactivity ^{40}K for a dynamic range up to the 2.5 MeV sum peak of ^{60}Co.

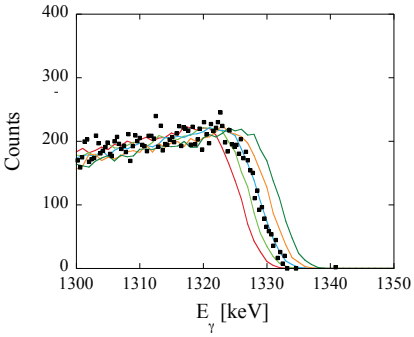

Fig. 6. The dependence of the Monte Carlo simulation on the electron beam energy is shown for the response function of the HPGe detector to the LCS γ-ray beam produced at the nominal energy 850 MeV. The best-fit result with E_e^c = 860.72 MeV is shown in comparison with those obtained with E_e^c = 860.72 $\pm$ 0.50 MeV and E_e^c = 860.72 $\pm$ 1.00 MeV.

injected an electron beam at the nominal energy 974 MeV, and repeated the procedure of deceleration down to 550 MeV. We produced LCS γ-ray beams with the CO_2 laser at two nominal energies, 974 MeV and 550 MeV. The response functions of the HPGe detector measured in the second injection are shown by the open circles in Fig. 3(a) and 3(c). The high-energy edge of the LCS γ-ray beam was excellently reproduced at these two energies.

IV. Applications

A. Linearity of a $LaBr_3$(Ce) detector

An interesting application of the present energy calibration of the electron beam may lie in energy calibration of photon detectors. To demonstrate such an application, we produced high-energy LCS γ-ray beams in an energy range of 10 - 8 MeV at the nominal energies 753.0 (calibrated energy 764.0), 714.0 (724.8) and 677.0 (687.7) MeV with a Nd:YVO_4 laser (SPECTRA-PHYSICS, INAZUMA, λ=1064 nm) and measured the γ-ray beams with a $LaBr_3$(Ce) detector (3.5" in diameter $\times$ 4.0" in length, BrilLanCe380 89S102/3.5, Saint-Gobain) at the count-rate less than 10 Kcps with a bias voltage of +400 V and a shaping time 0.5 μs of a NIM amplifier module. Figure 7 shows response functions of the $LaBr_3$(Ce) detector to these LCS γ-rays.

We performed Monte Carlo simulations of the response function of the $LaBr_3$(Ce) detector. The angle acceptance of the collimator with an aperture of 2mm diameter which is located at 1847cm from the collision point P2 is 0.054 mrad. It is pointed out in Ref. [10] that the γ beam energy spread due to the collimation is smaller than or comparable to that due to the electron beam energy spread, the collimation effect will start to alter the high energy edge of the spectrum, resulting in a shift of the spectrum toward the higher energy. This is not the case in the present measurement because the γ beam energy spread due to the collimation is $\eta^2\theta_e^2$ = (5.31 - 6.55) $\times$ 10^{-3}, whereas that due to the electron beam energy spread is 1.26 $\times$ 10^{-3}. The energy resolution of the $LaBr_3$(Ce) detector was incorporated into the simulation as effective energy resolution of the electron beam as was done for the HPGe detector. Best fits were obtained with the resolution 0.45% which can be translated into the detector resolution 2.1% in FWHM for 8 - 10 MeV γ rays. The energy resolution of the present $LaBr_3$(Ce) detector was 4.0% in FWHM for 662 keV γ rays and 2.6% in FWHM for 1332 keV γ rays. These energy resolutions are less than those (2.8% at 662 keV, 2.1% at 1332 keV, and 1% at 10 MeV) reported in small (3 $\times$ 10 mm^3 [16], 2" $\times$ 2" [17]) detectors.

Results of the Monte Carlo simulation are shown by the dotted lines in Fig. 7. The high-energy portion of the spectra including the FE peak and the bump of Compton scattering was well reproduced. It is noted that the low energy yield of the data includes contributions from backscattering by Pb blocks that were used as a part of the detector mount for the $LaBr_3$(Ce). The discrepancy between the experimental data and the simulation in the low-energy region is due to this backscattering. The FE peaks formed at 10.19 MeV, 9.14 MeV, and 8.19 MeV corresponded to the channel numbers, 947.2, 857.8, and 775.8, respectively. The linearity in the response of the $LaBr_3$(Ce) detector to the 8 - 10 MeV LCS γ rays is shown in Fig. 8, where the low-energy data were taken with the standard γ-ray sources (^{60}Co, ^{133}Ba, ^{137}Cs, and ^{152}Eu) and an Am-Be neutron source as a 4.4 MeV γ-ray emitter, including the single escape peak.

The data show that the linearity is slightly deteriorated at high energies beyond the Am-Be data at 4.4 MeV. A best fit with the 2nd-order polynomial function is shown by the solid line in Fig. 8 together with the best-fit parameters. For comparison, a linear fit to the data taken with the standard γ-ray sources and the Am-Be source is also shown by the dashed line in the figure. It is seen that the output of the $LaBr_3$(Ce) detector for 8 - 10 MeV γ rays is quenched to lower channel numbers from the linear response; the higher the energy is, the larger the quenching. A similar quenching effect

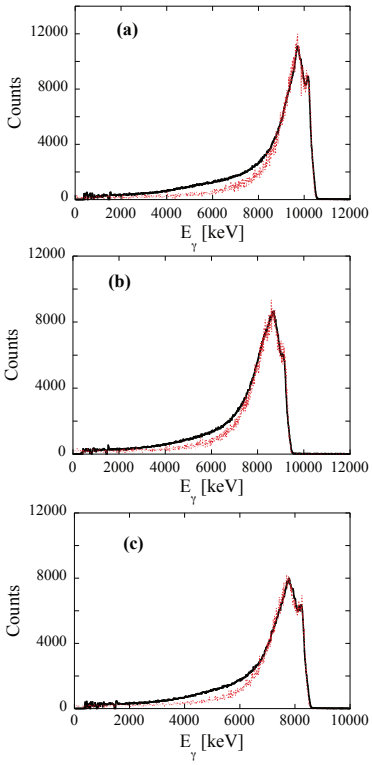

Fig. 7. (a) Monte Carlo simulations (dotted line) with 764.0 MeV (nominal energy 753 MeV) and ζ=1.7 mm for the LCS γ-ray beam produced with a Nd:YVO_4 laser in comparison with the experimental data (solid line). The experimental data are energy-calibrated following the simulation. (b) The same as (a), but for a simulation with 724.8 MeV (nominal energy 714 MeV) and ζ=2.5 mm. (c) The same as (a), but for a simulation with 687.7 MeV (nominal energy 677 MeV) and ζ=2.5 mm.

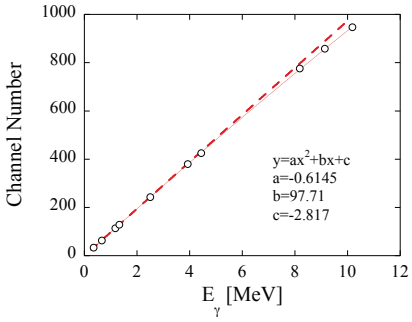

Fig. 8. Linearity in the response of a $LaBr_3$(Ce) detector to γ rays in the energy range 356 - 10190 keV. The data for low-energy photons were taken with the standard γ-ray sources, ^{60}Co, ^{133}Ba, ^{137}Cs, and ^{152}Eu, along with an Am-Be source. The data include the single escape peak of 4.4 MeV γ rays (Am-Be). The data for 8 -10 MeV γ rays were taken with LCS γ-ray beams produced with a Nd:YVO_4 laser. The solid line is the 2nd-order polynomial fit to the data, while the dashed line is the best linear fit to the low-energy data excluding those for the LCS γ rays.

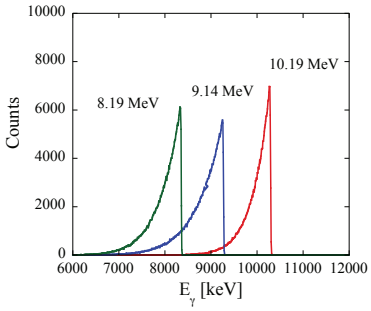

Fig. 9. (Color online) Results of the Monte Carlo simulations for energy distributions of the LCS γ-ray beams produced at the γ-ray experimental hutch GACKO of the synchrotron radiation facility NewSUBARU.

was previously reported above 10 MeV in a 2" $\times$ 2" $LaBr_3$(Ce) detector [17]. It is unknown, however, that the quenching is due to scintillation property intrinsic to the $LaBr_3$(Ce) crystal or saturation of the photomultiplier tube.

B. Energy profile of the LCS γ-ray beams

The present large volume $LaBr_3$(Ce) detector identified the FE peak in the response function as shown in Fig. 7. The Monte Carlo simulation, which best reproduced the response functions of the $LaBr_3$(Ce) detector, also provides the energy distribution of the LCS γ-ray beam incident on the detector. The energy profile of the LCS γ-ray beams is shown in Fig. 8. The present study shows that using a 2 mm collimator, LCS -ray beams were produced at 10.19 MeV in the FE peak with a 267 keV spread (δE) in FWHM, at 9.14 MeV with δE =394 keV, and at 8.19 MeV with δE =339 keV. The energy spread amounts to 2.6 - 4.3% in FWHM. The energy spread of the LCS γ-ray beam depends on tuning the electron and laser beam optics besides the collimator size.

V. Conclusion

We have systematically calibrated energies of the electron beams in the storage ring NewSUBARU in the nominal energy range of 550 - 974 MeV by using low-energy LCS γ-ray beams produced with a CO_2 laser at the γ-ray experimental hutch GACKO. The absolute energy calibration of the electron beams with the high accuracy and excellent reproducibility provides the energy calibration of high-energy LCS γ-ray beams produced with a Nd:YVO_4 laser. The energy-calibrated

LCS γ-ray beams produced in the range of 5.6 - 17.3 MeV in the fundamental mode of the laser operation with λ = 1064 nm offer a variety of experimental opportunities in nuclear science. The energy range can be extended to 11.2 - 34.6 MeV and 16.8 - 51.9 MeV in the second and third harmonics of the laser with λ = 532 nm and λ = 355 nm, respectively. As applications of the calibrated electron beams, we demonstrated a detector-calibration measurement with a 3.5" $\times$ 4.0" $LaBr_3$(Ce) detector in its response to 8 - 10 MeV γ rays and an energy-profile study of the high-energy LCS γ-ray beams. The large-volume $LaBr_3$(Ce) detector with the excellent response function and the good energy resolution can be a good instrument to determine the energy profile of the high-energy LCS γ-ray beams.

ACKNOWLEDGMENT

We thank H. Ohgaki of the Institute of Advanced Energy, Kyoto University for making a large volume $LaBr_3$(Ce) detector available to the present experiment. This work was supported by the Japan Private School Promotion Foundation and partly by the JSPS-FNRS bilateral program. D.M.F., O.T., and I.G. acknowledge financial support from the Extreme Light Infrastructure Nuclear Physics (ELI-NP) Phase I, a project co-financed by the European Union through the European Regional Development Fund. H.T.N. and T.R. acknowledge financial support from the Norwegian Research Council (NFR), project number 210007.

REFERENCES

[1] S. Amano, K. Horikawa, K. Ishihara, S. Miyamoto, T. Hayakawa, T. Shizuma, T. Mochizuki, "Several-MeV γ-ray generation at NewSUBARU by laser Compton backscattering," Nucl. Instrum. Methods in Phys. Res. A 602, pp. 337-341 (2009).

[2] K. Horikawa, S. Miyamoto, S. Amano, and T. Mochizuki, "Measurements for the energy and flux of laser Compton scattering -ray photons generated in an electron storage ring: NewSUBARU," Nucl. Instrum. Methods in Phys. Res. A 618, pp. 209-215 (2010).

[3] A. Ando, S. Amano, S. Hashimoto, H. Kinosita, S. Miyamoto, T. Mochizuki, M. Niibe, Y. Shoji, M. Terasawa, T. Watanabe, and N. Kumagai, "Isochronous storage ring of the NewSUBARU project," J. Synchrotron Rad. 5, pp.342-344 (1998).

[4] G. Audi, A.H. Wapstra and C. Thibault, "The AME2003 atomic mass evaluation (II). Tables, graphs and references," Nucl. Phys. A 729, pp. 337-676 (2003).

[5] L.C. Hsu, C.-C. Ching, C.-I. Yu, "Energy measurement of relativistic electron beams by laser Compton scattering," Phys. Rev. E 54, pp.5657-5663 (1996).

[6] R. Klein, T. Mayer, P. Kuske, R. Thornagel, G. Ulm, "Beam diagnostics at the BESSY I electron storage ring with Compton backscattered laser photons: measurement of the electron energy and related quantities," Nucl. Instrum. Methods in Phys. Res. A 384, pp.293-298 (1997).

[7] R. Klein, P. Kuske, R. Thornagel, G. Brandt, R. Görgen, G. Ulm, "Measurement of the BESSY II electron beam energy by Compton-backscattering of laser photons," Nucl. Instrum. Methods in Phys. Res. A486, pp.545-551 (2002).

[8] H. Ohgaki, H. Toyokawa, K. Kudo, N. Takeda, T. Yamazaki, "Generation and application of Laser-Compton gamma-ray at ETL," Nucl. Instrum. Methods in Phys. Res. A 455, pp.54-59 (2000)

[9] K. Chouffani, F. Harmon, D. Wells, J. Jones, and G. Lancaster, "Determination of electron beam parameters by means of laser-Compton scattering," Phys. Rev. ST Accel. Beams 9, pp.050701-1 - 050701-11 (2006).

[10] C. Sun, J. Li, G. Rusev, A. P. Tonchev, and Y. K. Wu, "Energy and energy spread measurements of an electron beam by Compton scattering method," Phys. Rev. ST Accel. Beams 12, pp.062801-1 - 062801-12 (2009).

[11] C.K.N. Patel, "Selective Excitation Through Vibrational Energy Transfer and Optical Maser Action in N_2-CO_2," Phys. Rev. Lett. 13, 617 (1964).

[12] R.L. Abrams, "Broadening coefficients for the P(20) CO_2 laser transition," Applied Physics Letters 25, 609 (1974).

[13] http://www.lasti.u-hyogo.ac.jp/NS-en/facility/ring/para.html

[14] W.R. Nelson, H. Hirayama and W.O. Roger, "The EGS4 Code Systems" SLAC-Report-265 (1985).

[15] H. Ohgaki, private communications.

[16] E. V. D. van Loef, P. Dorenbos, C. W. E. van Eijk, K. Krämer and H. U. Güdel, "High-energy-resolution scintillator: Ce^{3+} activated $LaBr_3$," Appl. Phys. Lett. 79, pp.1573-1575 (2001).

[17] M. Ciemala, D. Balabanski, M. Csatlós, J.M. Daugas, G. Georgiev, J. Gulyás, M. Kmiecik, A. Krasznahorkay, S. Lalkovski, A. Lefebre-Schuhl, R. Lozeva, A. Maj, A. Vitez. "Measurements of high-energy γ-rays with $LaBr_3$:Ce detectors," Nucl. Instrum. Methods in Phys. Res. A 608, pp.76-79 (2009).

6.5 Paper IV: Photoneutron cross sections for neodymium isotopes: toward a unified understanding of (γ, n) and (n, γ) reactions in the rare earth region I

6.6 Paper V: Photoneutron cross sections for samarium isotopes: toward a unified understanding of (γ, n) and (n, γ) reactions in the rare earth region II

6.7 Paper VI: Photo-neutron cross sections, radiative strength functions and astrophysical reaction rates of dysprosium isotopes

6.8 Paper VII: Level densities and γ-ray strength functions of $^{105-108}$Pd

Chapter 7

Summary and outlook

7.1 Summary

Statistical nuclear properties in the quasi-continuum energy region are studied for a wide range of nuclei, namely Dy, Pd, Sm and Nd isotopes. In particular, the nuclear level density, the radiative strength function and (γ, n) cross sections are studied thoroughly. The experimental techniques used are particle-γ coincidence measurements and photo-neutron experiments.

Small resonances in the vicinity of the giant electric dipole resonance are evident in the radiative strength function (RSF). Some of whom have a theoretical explanation and some which are jet to be fully understood. In the mass region of Pd isotopes we observe an enhanced strength in the ≈ 8 MeV γ-energy region. The strength might stem from the skin oscillation of excess neutrons against the core, but this is still an open question. The characteristics of this resonance is examined for $^{105-108}$Pd. Surprisingly, the strength is best modelled by a gaussian distribution. This Gaussian-shape might be made up of the sum of two or more Lorentzian functions, and one should consider the possibility of several resonances overlapping in this region.

The shape of the RSF at low γ energies indicate that Pd isotopes are in a transitional region regarding the upend structure. The upbend feature is not very pronounced, but we observe a constant strength over a wide γ-energy region. Also the origin of the upbend is not theoretically settled, and it is therefore of uppermost interest to study its appearance.

New Dy data are extracted at energies above the neutron separation threshold for ^{162}Dy and ^{163}Dy, in a region where there are no existing data. The photo-neutron cross sections and RSF's are evaluated. Dysprosium data have also been extracted at lower γ-ray energies for the $^{160-164}$Dy nuclei. In the mass region of Dy isotopes, the $M1$ scissors resonance mode is found around 3 MeV of γ energy.

The resonance can be modelled with a Lorentzian shape, where the strength, width and centroid are fitted to experimental data. The resonance parameters of the Dy isotopes are studied thoroughly.

The Nd and Sm isotopes are also investigated from photo-absorption experiments. The photo-neutron cross sections are extracted for the $^{143-146,148}$Nd and $^{144,147-150,152,154}$Sm nuclei. The TALYS reaction code have been used to reproduce the radiative neutron capture cross sections for the Nd and Sm isotopes, which are known, in addition to the unknown radiative neutron capture cross sections of the ^{147}Nd and ^{153}Sm nuclei.

The nuclear level densities and thermodynamic quantities are studied for the Dy nuclei. Thermodynamical properties are deduced within both micro-canonical and canonical ensemble theories. A phase transition from the pair-correlated state at low energies to a less correlated or uncorrelated state is studied in both ensembles. We observe transitions between the various quasiparticle regimes within the framework of the micro-canonical ensemble. In the canonical ensemble we observe a second-order phase transition, influenced by the first broken pairs of the nucleus, but also the later breaking of Cooper pairs enhances the phase transition significantly.

7.2 Outlook

In future experiments it would be interesting to extend the study of the upend structure to more nuclei. As mapping the properties of this enhancement would be crucial to obtain a theoretical understanding of its origin. The same reasoning should motivate further investigation of the enhanced strength in the ≈ 8 MeV γ-energy region of Pd, and neighbouring nuclei.

Explaining the origin of enhanced strength at low energies is interesting, not only with respect to the fundamental understanding of nuclear physics, the (n,γ) cross section for incident keV neutrons depends sensitively on the RSF, in the energy range below the neutron threshold, typically around 6 MeV of γ-ray energy. The predicted tail of the strength function at low energies therefore plays a fundamental role with respect to astrophysical applications.

Appendices

Appendix A

New intensities and FWHMs deduced for the NaI response functions

The unfolding procedure of the Oslo method is described in Ref. [38]. However, new and improved measurements of the response functions of the NaI detectors have been performed. New intensities and FWHMs deduced for the NaI response functions are given in Table A.1. The response functions are measured for several in-beam γ lines from excited states in ^{13}C, ^{16,17}O, ^{28}Si and ^{56,57}Fe [**?**].

In addition, the resolution of the response function is set to 10% of the experimental one due to technical reasons, compared to 50% in the method described in Ref. [38]. Besides these changes, the new unfolding method follows the procedures described in the paper from 1996, see Ref. [38].

E_γ (keV)	FWHM[keV][a]	ε^b_{tot}	p_f	p_c	p_s	p_d	p_a
800.0	72.8	0.923	0.5778	0.4222	0.0000	0.0000	0.0000
1600.0	103.1	1.003	0.3968	0.5896	0.0097	0.0000	0.0039
2400.0	135.7	1.023	0.3135	0.6537	0.0180	0.0000	0.0148
3200.0	163.9	1.037	0.2443	0.6918	0.0340	0.0071	0.0227
4000.0	188.2	1.045	0.1970	0.7059	0.0444	0.0086	0.0441
4800.0	207.3	1.053	0.1599	0.7256	0.0525	0.0092	0.0529
5600.0	222.7	1.059	0.1435	0.7489	0.0577	0.0084	0.0415
6400.0	238.6	1.066	0.1296	0.7671	0.0590	0.0081	0.0362
7200.0	263.5	1.071	0.1200	0.7760	0.0524	0.0089	0.0427
8000.0	287.4	1.073	0.1102	0.7850	0.0458	0.0096	0.0493
8800.0	310.2	1.076	0.0999	0.7953	0.0389	0.0104	0.0556
9600.0	331.9	1.079	0.0897	0.8054	0.0321	0.0111	0.0619
10400.0	351.9	1.081	0.0830	0.8126	0.0307	0.0113	0.0623

[a] Normalized to 79.9 keV (6%) at 1.33 MeV.
[b] Normalized to 1 at 1.33 MeV.

Table A.1: New intensities and FWHMs deduced for the NaI response functions.

Appendix B

Solving for $\sigma(E_\gamma)$ by using a Taylor expansion method

We will use a Taylor expansion method to solve for $\sigma(E_\gamma)$ in the following expression [46],

$$\int_{S_n}^{E_{\mathrm{Max}}} n_\gamma(E_\gamma)\sigma(E_\gamma)dE_\gamma = \frac{N_n}{N_t N_\gamma \xi \varepsilon_n g}, \tag{B.1}$$

where N_n represents the number of neutrons detected, N_t gives the number of target nuclei per unit area, N_γ is the number of γ rays incident on target, ε_n represents the neutron detection efficiency, and finally $\xi = (1-e^{\mu t})/(\mu t)$ is a correction factor for self-attenuation in the target. The factor g represents the fraction of γ flux above the neutron threshold S_n.

We choose to expand the cross section $\sigma(E_\gamma)$ around the average γ-ray energy E_{av},

$$\sigma(E_\gamma) = \sum_{i=0}^{\infty} \frac{\sigma^{(i)}(E_{\mathrm{av}})}{i!}(E_\gamma - E_{\mathrm{av}})^i. \tag{B.2}$$

Inserting into Eq. (B.1), we obtain

$$\begin{aligned}
\int_{S_n}^{E_{\mathrm{Max}}} n_\gamma(E_\gamma)\sigma(E_\gamma)dE_\gamma &= \sigma^{(0)}(E_{\mathrm{av}}) \int_{S_n}^{E_{\mathrm{Max}}} n_\gamma(E_\gamma)dE_\gamma \\
&+ \sigma^{(1)}(E_{\mathrm{av}}) \int_{S_n}^{E_{\mathrm{Max}}} n_\gamma(E_\gamma)(E_\gamma - E_{\mathrm{av}})dE_\gamma \\
&+ \frac{1}{2}\sigma^{(2)}(E_{\mathrm{av}}) \int_{S_n}^{E_{\mathrm{Max}}} n_\gamma(E_\gamma)(E_\gamma - E_{\mathrm{av}})^2 dE_\gamma \\
&+ \frac{1}{6}\sigma^{(3)}(E_{\mathrm{av}}) \int_{S_n}^{E_{\mathrm{Max}}} n_\gamma(E_\gamma)(E_\gamma - E_{\mathrm{av}})^3 dE_\gamma,
\end{aligned} \tag{B.3}$$

where we have truncated the series for $i > 3$. When we have applied these formulas, we have ensured that the cross sections take the form of a third order polynomial, with the result that all higher order terms vanish. We can also show that the second term of the series equals zero:

$$\begin{aligned}\sigma^{(1)}(E_{\rm av})\int_{S_n}^{E_{\rm Max}} n_\gamma(E_\gamma)(E_\gamma - E_{\rm av})dE_\gamma \qquad (B.4)\\ = \sigma^{(1)}(E_{\rm av})[\int_{S_n}^{E_{\rm Max}} n_\gamma(E_\gamma)E_\gamma dE_\gamma \;\; - \;\; \int_{S_n}^{E_{\rm Max}} n_\gamma(E_\gamma)E_{\rm av}dE_\gamma].\end{aligned}$$

The integral in the first term in Eq. (B.4) is identified as the the average γ energy of the beam,

$$\int_{S_n}^{E_{\rm Max}} n_\gamma(E_\gamma)E_\gamma dE_\gamma = E_{\rm av}, \qquad (B.5)$$

which is exactly the same solution we obtain from the second term,

$$\int_{S_n}^{E_{\rm Max}} n_\gamma(E_\gamma)E_{\rm av}dE_\gamma = E_{\rm av}\int_{S_n}^{E_{\rm Max}} n_\gamma(E_\gamma)dE_\gamma = E_{\rm av}, \qquad (B.6)$$

since the energy distribution of the γ-ray beam is normalized to one. Hence, the terms in the bracket expression in Eq. (C.4) cancel out, and the S_1 term disappears.

We also notice that the first term in the Taylor series of Eq. (B.4) equals the cross section derived at the average energy, which we identify as the monochromatic cross section $\sigma_{\rm mono}(E_{\rm av})$. We can express Eq. (B.4) in the more compact way,

$$\int_{S_n}^{E_{\rm Max}} n_\gamma(E_\gamma)\sigma(E_\gamma)dE_\gamma = \sigma_{\rm mono}(E_{\rm av}) + S_2 + S_3, \qquad (B.7)$$

where

$$\begin{aligned} S_2 &= \frac{1}{2}\sigma^{(2)}(E_{\rm av})\int_{S_n}^{E_{\rm Max}} n_\gamma(E_\gamma)(E_\gamma - E_{\rm av})^2 dE_\gamma \qquad (B.8)\\ S_3 &= \frac{1}{6}\sigma^{(3)}(E_{\rm av})\int_{S_n}^{E_{\rm Max}} n_\gamma(E_\gamma)(E_\gamma - E_{\rm av})^3 dE_\gamma. \end{aligned}$$

Appendix C

Solutions of the primary γ-ray matrix

The normalized primary γ ray matrix can be written as [45]

$$P(E_i, E_\gamma) = \frac{\mathscr{T}(E_\gamma)\rho(E_i - E_\gamma)}{\sum_{E_\gamma=E_\gamma^{\min}}^{E_i} \mathscr{T}(E_\gamma)\rho(E_i - E_\gamma)}. \tag{C.1}$$

This function does not give a one-to-one solution when solving for $\rho(E_i - E_\gamma)$ and $\mathscr{T}(E_\gamma)$, but an infinite number of possibilities. If we have one set of solutions $\rho(E_i - E_\gamma)$ and $\mathscr{T}(E_\gamma)$, we can construct other solutions through the following transformation [45]:

$$\tilde{\rho}(E_i - E_\gamma) = \rho(E_i - E_f)g(E_i - E_\gamma) \tag{C.2}$$

$$\tilde{\mathscr{T}}(E_\gamma) = \mathscr{T}(E_\gamma)f(E_\gamma). \tag{C.3}$$

All solutions have to fulfill Eq. (5.9),

$$P(E_i, E_\gamma) = \frac{\mathscr{T}(E_\gamma)\rho(E_i - E_\gamma)}{\sum_{E'_\gamma=E_\gamma^{\min}}^{E_i} \mathscr{T}(E'_\gamma)\rho(E_i - E'_\gamma)} = \frac{\tilde{\mathscr{T}}(E_\gamma)\tilde{\rho}(E_i - E_\gamma)}{\sum_{E'_\gamma=E_\gamma^{\min}}^{E_i} \tilde{\mathscr{T}}(E'_\gamma)\tilde{\rho}(E_i - E'_\gamma)}. \tag{C.4}$$

Inserting Eqs. (C.3) and (C.3) into Eq. (C.4),

$$\frac{\mathscr{T}(E_\gamma)\rho(E_i - E_\gamma)}{\sum_{E'_\gamma=E_\gamma^{\min}}^{E_i} \mathscr{T}(E'_\gamma)\rho(E_i - E'_\gamma)} = \frac{\mathscr{T}(E_\gamma)f(E_\gamma)\rho(E_i - E_f)g(E_i - E_\gamma)}{\sum_{E'_\gamma=E_\gamma^{\min}}^{E_i} \mathscr{T}(E'_\gamma)f(E'_\gamma)\rho(E_i - E_f)g(E_i - E'_\gamma)} \tag{C.5}$$

and rearranging we obtain

$$f(E_\gamma)g(E_i - E_\gamma) \sum_{E'_\gamma = E_\gamma^{\min}}^{E_i} \mathscr{T}(E'_\gamma)\rho(E_i - E'_\gamma) = \sum_{E'_\gamma = E_\gamma^{\min}}^{E_i} f(E'_\gamma)g(E_i - E'_\gamma)\mathscr{T}(E'_\gamma)\rho(E_i - E_f). \tag{C.6}$$

We observe that the right hand side of the above equation is independent of E_γ, thus the left hand side must also be independent of this variable. As a result we can conclude that the product of f and and g is a function of E_i alone,

$$f(E_\gamma)g(E_i - E_\gamma) = h(E_i). \tag{C.7}$$

We aim to find a functional form of f and g. In order to do so we investigate Eq. (C.7) for some special values of E_γ. First, examining the equation for $E_\gamma = E_i$, yielding

$$Af(E_\gamma) = h(E_\gamma), \tag{C.8}$$

where we have set the constant $g(0) = A$. Since Eq. (C.7) should hold for all values of E_γ, we can insert the above result,

$$f(E_\gamma)g(E_i - E_\gamma) = Af(E_i). \tag{C.9}$$

Furthermore, setting $E_\gamma = 0$ and $f(0) = B$, we can write

$$Bg(E_i) = Af(E_i). \tag{C.10}$$

Inserting this in Eq. (C.9) one obtains

$$g(E_\gamma)g(E_i - E_\gamma) = Ag(E_i). \tag{C.11}$$

Using a Taylor series expansion for the function g in the limit of $E_\gamma \to 0$ yields

$$(A + g'(0)E_\gamma)(g(E_i) - g'(E_i)E_\gamma) = AgE_i, \tag{C.12}$$

where we terminate second and higher order terms in the series. Further, this is equivalent to,

$$Ag'(E_i) = g'(0)g(E_i). \tag{C.13}$$

We define $\alpha \equiv g'(0)/A$, and we solve the differential equation

$$\int_0^{E_i} \frac{dg(E_I)}{g(E_i)} = \alpha \int_0^{E_i} dE_i. \tag{C.14}$$

We then obtaining the following:

$$g(E_i) = Ae^{\alpha E_i}. \tag{C.15}$$

Combining Eqs. (C.15) and (C.10) gives the remaining relation

$$f(E_i) = Be^{\alpha E_i}. \tag{C.16}$$

Finally, inserting Eqs. (C.15) and (C.16) into Eqs. (C.3) and (C.3) we get

$$\tilde{\rho}(E_i - E_\gamma) = \rho(E_i - E_\gamma) A e^{\alpha(E_i - E_\gamma)} \tag{C.17}$$

$$\tilde{\mathscr{T}}(E_\gamma) = \mathscr{T}(E_\gamma) B e^{\alpha E_\gamma}. \tag{C.18}$$

Bibliography

[1] H.A. Bethe, Phys. Rev. **50**, 332 (1936).

[2] A. Gilbert, A. G. W. Cameron, Can. J. Phys. **43** (1965) 1446.

[3] T. von Egidy, H. H. Schmidt, A. N. Behkami, Nucl. Phys. **A 481** (1988) 189.

[4] T. von Egidy, Dorel Bucurescu, Phys. Rev. **C 72** , (2005), 044311, and Phys. Rev. **C 73** , (2006), 049901(E).

[5] T. von Egidy and D. Bucurescu. Phys. Rev. C **80**, 054310 (2009).

[6] S. Goriely, S. Hilaire, and A.J. Koning, Phys. Rev. C **78**, 064307 (2008).

[7] S. Hilaire, M. Girod, S. Goriely, and A.J. Koning, Nucl. Phys. C **86**, 064317 (2012).

[8] H. Nakada, and Y. Alhassid, Phys. Rev. Lett. **79**, 2939 (1997).

[9] Y. Alhassid, S. Lui, and H. Nakada, Phys. Rev. Lett **83**, 4265 (1999).

[10] Y. Alhassid, S. Lui, and H. Nakada, Phys. Rev. Lett **99**, 162504 (2007).

[11] R. Capote *et. al.*, Reference Input Library, RIPL-2 and RIPL-3, available online at URL: http://www-nds.iaea.org/RIPL-3/.

[12] G. A. Batholomew, E. D. Earle, A. J. Fergusson, J. W. Knowles. M. A. Lone, Adv. Nucl. Phys. **7** , 229 (1972).

[13] D. M. Brink, Ph.D. thesis, Oxford University (1955).

[14] P. Axel, Phys. Rev. **126**, 671 (1962).

[15] S. G. Kadmenskiĭ, V. P. Markushev, V. I. Furman, Yad. Fiz. **37** (1983) 277 [Sov. J. Nucl. Phys. **37** (1983) 165].

[16] J. Kopecky and R. E. Chrien, Nucl. Phys. A **468**, 285 (1987).

[17] C. Lederer *et al.*, Phys. Rev. Lett **110**, 022501 (2013).

[18] F. Käppeler, R. Gallino, S. Bisterzo, and W. Aoki, Rev. Mod. Phys. **83**, 157 (2011).

[19] H. Utsunomiya, S. Goriely, H. Akimune, H. Harada, F. Kitatani, S. Goko, H. Toyokawa, K. Yamada, T. Kondo, O. Itoh, M. Kamata, T. Yamagata, Y.-W. Lui, I. Daoutidis, D.P. Arteaga, S. Hilaire, and A.J. Koning, Phys. Rev. C **82**, 064610 (2010).

[20] The homepage of SPring-8 research,
URL: http://www.spring8.or.jp/en/facilities/accelerators/.

[21] S. Amano, K. Horokawa, K. Ishihara, S. Miyamoto, T. Hayakawa, T. Shizuma, T. Mochizuki, Nucl. Inst. and Meth. A **602**, (2009), 337-341.

[22] The homepage of RIKEN research,
URL: http://xfel.riken.jp/eng/gallery/index.html#image/001-1.jpg.

[23] The homepage of NewSUBARU,
URL: http://www.lasti.u-hyogo.ac.jp/NS-en/newsubaru/.

[24] H. Utsunomiya, T. Shima, K. Takahisa, D. M. Filipescu, O. Tesileanu, I. Gheorghe, H.-T. Nyhus, T. Renstr£m, Y.-W. Lui, Y. Kitagawa, S. Amano, S. Miyamoto, Accepted to be published in IEEE Transactions on nuclear science, (2014).

[25] H. Ohgaki, H. Toyokawa, K. Kudo, N .Takeda, T .Yamazaki, Nucl. Instrum. Methods in Phys. Res. A **455**, pp.54-59 (2000).

[26] A. Ando, S. Amano, S. Hashimoto, H. Kinosita, S. Miyamoto, T. Mochizuki, M. Niibe, Y. Shoji, M. Terasawa, T. Watanabe, and N. Kumagai, Ó Isochronous storage ring of the NewSUBARU project,Ó J. Synchrotron Rad. 5, pp.342-344 (1998).

[27] F. Kitatani, H. Harada, S. Goko, H. Utsunomiya, H. Akimune, T. Kaihori, H. Toyokawa, and K. Yamada, Journal of Nuclear Science and Technology, Vol. **47**, No. 4, p. 367-375 (2010).

[28] K. Y. Hara, H. Harada, F. Kitatani, S. Goko, S.-ya Hohara, T. Kaihori, A. Makinaga, H. Utsunomiya, H. Toyokawa, and K. Yamada, Journal of Nuclear Science and Technology, Vol. **44**, No. 7, p. 938-945 (2007).

[29] B. L. Berman, and F. C. Fultz, Rev. Mod. Phys. **47**, 713-761 (1975).

[30] O. Itoh, H. Utsunomiya, H. Akimune, T. Kondo, M. Kamata, T. Yamagata, H. Toyokawa, H. Harada, F. Kitatani, S. Goko, C. Nair, and Y. W. Lui, Journal of Nuclear Science and Technology, Vol. **48**, No. 5, 834-840 (2011).

[31] T. Kondo, H. Utsunomiya, H. Akimune, T. Yamagata, A. Okamoto, H. Harada, F. Kitatani, T. Shima, K. Horikawa, S. Miyamoto, Nucl. Inst. and Meth. A **659**, 462-466 (2011).

[32] NIST Physical Measurement Laboratory, URL: http://physics.nist.gov/PhysRefData/XrayMassCoef/tab3.html.

[33] H. Toyokawa, T. Kii, H. Ohgaki, T. Shima, T. Baba, and Y. Nagai, IEEE Transactions on nuclear science, Vol. **47**, No 6, (2000).

[34] The homepage of OCL,
URL: http://www.mn.uio.no/fysikk/english/research/about/infrastructure/OCL.

[35] M. Guttormsen, A. Atac, G. Løvhøiden, S. Messelt, T. Ramsøy, J. Rekstad, T.F. Thorsteinsen, T.S. Tveter, and Z. Zelazny, Phys. Scr. T **32**, 54 (1990).

[36] M. Guttormsen, A. Bürger, T. E. Hansen, and N. Lietaer, Nucl. Instrum. Methods Phys. Res. A **648**, 168 (2011).

[37] W. R. Leo, *Techniques for nuclear and particle physics experiments*, Springer Verlag (1994) 24-30.

[38] M. Guttormsen, T. S. Tveter, L. Bergholt, F. Ingebretsen, J. Rekstad, Nucl. Inst. Meth. A **374** (1996) 371-376.

[39] Private communication with M. Guttormsen (2014).

[40] N. Starfelt and H. W. Koch, Phys. Rev. **102** (1956) 1598.

[41] P. C. Fisher and L. B. Engle, Phys. Rev. **134** (1964) B 796.

[42] M. Guttormsen, T. Ramsøy, J. Rekstad, Nucl. Inst. Meth. A, **255** (1987), 518-523.

[43] A. C. Larsen, M. Guttormsen, M. Kritcka, E. Betak, A. Bürger, A. Görgen, H. T. Nyhus, J. Rekstad, A. Schiller, S. Siem, H. K. Toft, G. M. Tveten, A. V. Voinov and K. Wikan, Phys. Rev. C **83**, 034315 (2011).

[44] A. Bohr, B. Mottelson, Nuclear Structure, Benjamin, New York, Vol. I, pp. 184-185, (1969).

[45] A. Schiller, L. Bergholt, M. Guttormsen, E. Melby, J. Rekstad and S. Siem, Nucl. Inst. Methods Phys. Res. A **447**, 498 (2000).

[46] H. Utsunomiya, A. Makinaga, S. Goko, T. Kaihori, H. Akimune, T. Yamagata, M. Ohta, H. Toyokawa, S. Müller, Y.-W. Lui, and S. Goriely, Phys. Rev. C **74**, 025806 (2006).

[47] Data extracted using the NNDC On-Line Data Service from the ENSDF database.

[48] A. Voinov, M. Guttormsen, E. Melby, J. Rekstad, A. Schiller, and S. Siem, Phys. Rev. C **63**, 044313 (2001).

[49] L. Henden, L. Bergholt, M. Guttormsen, J. Rekstad and T. S. Tveter, Nucl. Phys. A **589**, 249 (1995).